The Evolution of dark matter substructure

a Ph.D. thesis by

Carlos Antonio Calcáneo Roldán

August 2001

Abstract

This thesis investigates the dynamical evolution of systems orbiting within deeper potentials. Initially we use a simple satellite-halo interaction to study the dynamical processes that act on orbiting systems and we compare these results to analytical theory. Deep images of the Centaurus cluster reveal a spectacular arc of diffuse light that stretches for over 100 kpc and yet is just a few kpc wide. We use numerical simulations to show that this feature can be produced by the tidal debris of a spiral galaxy that has been disrupted by the potential of one of the central cD galaxies of the cluster.

The evolution of sub-halos is then studied in a cosmological context using high resolution N-body simulations of galactic mass halos that form in a cold dark matter (CDM) simulation. CDM halos form via a complex series of mergers, accretion events and violent relaxation. Halos are non-spherical, have steep singular density profiles and contain many thousands of surviving dark matter substructure clumps. This will lead to several unique signatures for experiments that aim to detect dark matter either indirectly, through particle annihilation, or directly in a laboratory. For the first time it is possible to construct maps of the gamma-ray sky that result from the annihilation of dark matter particles within simulated dark matter halo distributions.

The Evolution of Dark Matter Substructure

Carlos Antonio Calcáneo Roldán

A thesis submitted to the University of Durham
in accordance with the regulations for admission to the
Degree of Doctor of Philosophy.

Physics Department

University of Durham
2001

Contents

List of Figures

List of Tables

Declaration

The Evolution of dark matter substructure

The work described in this thesis was undertaken between October 1997 and May 2001 whilst the author was a research student under the supervision of Dr Ben Moore and Prof. Carlos Frenk in the Department of Physics at the University of Durham. This work has not been submitted for any other degree at this (or any other) university.

The work presented in this thesis is my own, unless otherwise explicitly stated. I played a leading role in all the work presented. The cosmological simulations of the "Local Group" and "Draco" (which were used in Chapter 2 and Chapter 4) were carried out in collaboration with Ben Moore, Joachim Stadel, Tom Quinn, George Lake, Sebastiano Ghigna and Fabio Governato. The observations presented in Chapter 3 were carried out by David Malin.

The main results have appeared in the following papers:

- C. Calcáneo–Roldán, B. Moore, J. Bland–Hawthorn, D. Malin and E. M. Sadler, Mon. Not. R. Astron. Soc. **314**, 324 (2000).
- C. Calcáneo–Roldán and B. Moore, Phys. Rev. D **62**, 123005 (2000).
- B. Moore, C. Calcáneo–Roldán, J. Stadel, T. Quinn, G. Lake, S. Ghigna and F. Governato, Phys. Rev. D, in press (`astro-ph/0106271`).

Throughout this thesis I will use the conventional 'we' to refer to the first person

Acknowledgements

The moment has come to thank everyone who has helped me to reach this point in my life. I'm sure the list should be never-ending, so I hope you can settle for this.

Firstly I must thank Carlos Frenk for giving me the opportunity to come to Durham in the first place: You really saved me when I needed it most! And related thanks also go to Shaun Cole for following up my application even though it was late (apparently the Royal mail *still* cannot find the original!).

I acknowledge the generous support of the Consejo Nacional de Ciencia y Tecnología (CONACyT). My entire postgraduate training would not have been possible without the grant it has provided.

I hope Ben Moore knows how important his guidance and encouragement has been throughout my years in Durham; you managed to turn my chaotic thoughts into something that could resemble science. You've been an excellent supervisor and a very good friend. Thanks Ben!

Special mention needs to go to Arnold Wolfendale, I will never be able to transmit how much I admire this man; in just a few conversations he managed to reopen my eyes to the beauty of my subject, I don't think I know anyone as kind!

Adrian Jenkins deserves special mention for helping out always in times of desperation and for feeding me the best roast potatoes on earth! Special thanks also go to Dorothy Jenkins. I am lucky to have had such a nice friend in the department. How *do* you manage to know *everything*?!

I am greatly indebted to Allan Lotts for running the astronomers computer cluster so efficiently and for always giving me a hand. (even when he was up to his ears in work!)

For putting up with me in the office the Oscar goes to: Andrew, Fiona, Geoff, Mikey, Nathan and Russell. I promise I won't stop taking my medication!

Finally, special thanks to Jean and Cathryn for sharing their home and their hearts with us. You made every moment of our life in Durham so special that words will never be enough to thank you. See you in the hacienda!

Todo lo que soy se lo debo a mi mamá: Rosario. Nunca tendré suficientes palabras para agradecer todo lo que me has dado: Thanks mom!

Un abrazote, un besote y todo lo que soy no son suficientes para compensar a María Elena. Mi amiga, mi amor y mi vida: Ti vorrò sempre assai!

Esta tesis está dedicada a ellas.

From each according to their ability. To each according to their needs. *Carl Marx*

Chapter 1 | *Introduction*

There is overwhelming evidence that most of the mass in the Universe is made up of some form of non-luminous "*dark matter*" and that this material is not the usual baryonic matter of everyday life (protons, neutrons, electrons, etc.) but some particle with as yet unknown properties. Determining the nature of dark matter is one of the most important unsolved problems in modern cosmology.

Many scales have been probed for evidence in favour of dark matter: from the cosmological or global scale of the Universe to the local scale of galaxies. Until recently, the second of these methods was the most favoured because it was relatively easy to extract information from the dynamics of nearby systems. Most recently, experiments on a cosmological scale (*e.g.* BOOMERanG [89], or The Supernova Cosmology Project [109]) are making possible detailed measurements of many cosmological parameters. In fact, it is not uncommon to hear many enthusiastic cosmologists say that we are living in "The precision era of cosmology".

By combining observations of astrophysical objects such as galaxies and clusters with assumptions for the dynamics of these objects it is possible to construct theories that model their origin and evolution. Techniques have vastly improved over time; astronomers observe the Universe on many scales, from local star clusters to distant galaxy clusters and beyond. To give an accurate explanation for these observations it is important to make the most realistic models for the interactions that occur between astrophysical objects.

The work presented in this thesis is relevant mostly to galactic and cluster scales; nevertheless, because all that we are about to discuss assumes the existence of dark matter, it is important to have an understanding of why it is reasonable to make this assumption. We shall begin by reviewing the most recent major observational results that are determining the fundamental parameters that define our Universe.

1.1 Matter and energy in the Universe

The quantity and composition of matter and energy in the Universe is of fundamental importance in cosmology. For simplicity, all forms of matter and energy may be written

as a fraction of the critical energy density:

$$\Omega_o \equiv \frac{\rho_{tot}}{\rho_o} = \Omega_{rad} + \Omega_M + \Omega_\Lambda$$

where subscript 'o' denotes the value at the present epoch, $\rho_o = 3H_o^2/8\pi G \approx 1.88\,h^2 gcm^{-3}$ $\approx 278\,h^2 M_\odot kpc^{-3}$ (in these expressions $H_o = 100 h kms^{-1}Mpc^{-1}$ is the Hubble constant and h is a number in the range from 0.5 to 1 - with $h \sim 0.65$ being the currently favoured value). In the present discussion we shall decompose the matter/energy density into three components: the fraction contributed by radiation (or relativistic species) Ω_{rad}, the matter component Ω_M and a smooth contribution Ω_Λ. (There is no *a priori* reason to consider only these components, this specific choice tries to reflect current measured values, only matter and radiation are self evident components.)

One of the most well defined observations in cosmology (with a precision greater than 0.05%) is that the cosmic microwave background radiates as a black body of temperature $T_o = 2.7277$ K. This means that the contribution to the total energy density of the Universe from photons may be calculated precisely to be $\Omega_\gamma h^2 = 2.48 \times 10^{-5}$. If neutrinos are either massless or very light then their energy density is also well known because it is related to that of photons $\Omega_\nu h^2 = 6 \times \frac{7}{8}(4/11)^{4/3}\Omega_\gamma$ (considering that there are 6 neutrino species). Big-Bang nucleosynthesis (BBN) constrains the amount of additional relativistic species unless they were produced after the epoch of BBN [26].

Because the contribution of the radiation to the total energy density in the Universe is so low, we shall continue this discussion taking into account only the other two components that we are considering, namely Ω_M and Ω_Λ.

The temperature of the Cosmic Microwave Background radiation (CMB) is almost isotropic throughout the sky. This is strong evidence that the Universe began in a state of infinite density. However, on the smallest scales probed the CMB presents a temperature anisotropy of $\Delta T/T \approx 10^{-5}$. These fluctuations may be used to determine the value of Ω_o.

In the hot dense state of the early Universe all the particles were coupled. This includes photons and baryons (electrons and ions). As the Universe cools there comes a point when photons scatter from the baryons. The CMB we observe is made up of photons which come to us from the surface of this "last scattering". As the baryons accreted into the dark matter potential wells the pressure of photons acted as a restoring force, and this resulted in acoustic oscillations driven by gravity. These oscillations can be decomposed into their Fourier modes; the multipole amplitudes C_{lm} of the CMB anisotropy are determined by

those modes with $k \sim l\mathrm{H}_o/2$. Last scattering occurs over a short period of time, this makes the CMB a snapshot of the Universe at the time of last scattering in which each mode is "seen" in a well defined phase of its oscillation. Modes caught at maximum compression or rarefaction lead to the largest temperature anisotropy, which results in a series of acoustic peaks. The position of the first peak depends on the value of Ω_o (in fact: $l \approx 200/\sqrt{\Omega_o}$) [132]. Recent observations of the CMB [89] make it possible to constrain the location of the first peak ($l = 200 \pm 8$ [71]) which in turn fixes the value of the total matter/energy density of the Universe: $\Omega_o = 1 \pm 0.1$.

The predicted primeval abundance of ^{4}He ($\approx 25\%$) was the first success of BBN. The consistency of the BBN predictions for the abundances of the light elements (D, ^{3}He, ^{4}He, and ^{7}Li) with their inferred primeval abundances has been an important test of the Big-Bang model at early times. Of all the light elements, deuterium provides the best measure of the baryon density in the Universe. This is because the primeval abundance of deuterium is most sensitive to baryon density ($\propto 1/\rho_{baryon}^{1.7}$) and its evolution since the Big-Bang is simple (stars only destroy it).

Local measurements, where about half the material has been through stars, do not reflect directly the primordial abundances. Recently, deuterium Lyman features in the absorption spectra of three high redshift (z> 2) quasars has allowed an accurate determination of the primeval abundance of deuterium $\rho_D/\rho_H = (3.0 \pm 0.2) \times 10^{-5}$ [27]. This, in turn leads to a value for the baryon density of the Universe of $\Omega_{baryon}\mathrm{h}^2 = 0.02 \pm 0.002$ [27]. Current CMB measurements also provide a limit of $\Omega_{baryon}\mathrm{h}^2 > 0.019$[71] which is consistent with the previous result.

A definite conclusion as to the value of Ω_o is not far away, ultimately the issue will be settled by NASA's MAP and ESA's Planck satellites (which are due to launch later this decade). They will be able to map the entire CMB sky with unprecedented resolution ($\approx 0.1^\circ$).

Another approach to measuring the total mass/energy density is through the deceleration parameter,

$$q_o \equiv -\frac{(\ddot{\mathrm{R}}/\mathrm{R})_o}{\mathrm{H}_o^2} = \frac{\Omega_o}{2}\left[1 + 3p_o/\rho_o\right],$$

which quantifies the present day slowing down of the expansion due to gravity.

This method depends on an accurate knowledge of the luminosity distance (d_L) for an object which, for low redshift z, is related to q_o via

$$d_\mathrm{L}\mathrm{H}_o = z + z^2(1 - q_o)/2 + \mathcal{O}(z^3) \tag{1.1}$$

thus, precision measurements of the flux, $\mathcal{F}$, of objects with known luminosity, L, can be used to determine q_o. (The luminosity distance to an object can be inferred from the inverse square law: $d_{\rm L} \equiv \sqrt{{\rm L}/4\pi\mathcal{F}}$.)

Recently, two groups (the Supernova Cosmology Project and the High-z Supernova Team) used accurate measurements of the flux from objects of well defined luminosity (type Ia supernovæ — SNeIa) to conclude that the expansion of the Universe is accelerating rather than decelerating; *i.e.* $q_o < 0$ [108, 118]. This implies that much of the energy in the Universe is in an unknown component with negative pressure. The most popular explanation for this new component is the existence of a cosmological constant, $\Omega_\Lambda \neq 0$. (Although we are warned — see *e.g.* Ref. [133] — that Eq. (1.1) is not accurate enough at the redshifts of the SNeIa, both groups actually compute d_L as a function of Ω_M and Ω_Λ therefore some modeling has been introduced.)

Thus, by combining modern observations of the CMB [89], with recent observations of supernovæ [109], the currently favoured paradigm is a Universe in which the matter content corresponds to roughly one third of the total density, *i.e.* $\Omega_M \approx 0.3$ and there is an extra smooth component of dark energy that contributes $\Omega_\Lambda \approx 0.6$. The reality and physical nature of this component is currently being debated, but the constraint on the matter content is generally well accepted.

It is also clear that the small value for the baryon fraction in the Universe suggests that most of the matter ($\sim 90\%$) must actually be in the form of some as yet unknown non-baryonic material (we shall see additional evidence for this in the next section).

1.2 Astrophysical evidence for dark matter

In 1932, Oort analysed numbers and velocities of stars near the Sun and concluded that the amount of gravitating matter implied by these velocities was 30% to 50% higher than that which was due to the visible stars. Then, in 1933, Zwicky concluded that the velocity dispersions in rich clusters of galaxies required 10 to 100 times more mass to keep them bound than could be accounted for by the luminous galaxies themselves.

It is not straightforward to conclude from these examples that this is evidence for some form of exotic matter, but they do illustrate how the dynamics of stars, galaxies and clusters can serve as a probe for the matter content of the Universe.

Because they gather material from such a large region of space, rich clusters provide a fair sample of the matter in the Universe (clusters typically form from density

perturbations with a comoving size of around 10 Mpc). The evidence for dark matter in clusters has traditionally been inferred from the application of the virial theorem to galaxy motions within the cluster. Because the virial theorem relates the total kinetic (T) and potential (U) energy for a bound object, it is possible to extract a total mass for clusters assuming that the system is in equilibrium.

There are several independent ways of "weighing" clusters. Maps of the X-ray brightness and temperature profiles are now good enough to allow estimates of the depth of the gravitational well confining the hot X-ray emitting gas. Another method is based on the detection of large numbers of very faint background galaxies whose shapes are distorted by the effects of light bending due to the clusters gravitational field. This technique has the advantage that it offers very direct information about the total mass distribution, whatever its characteristics may be.

Another way to estimate Ω_M from clusters is based on an inventory of matter coupled with BBN. Most of the baryons in clusters reside in the hot X-ray emitting, intracluster gas and not in the galaxies themselves[150, 57]; the problem then reduces to determining the gas-to-total mass ratio, f_{gas}. Recent observations of clusters with high X-ray luminosity [48]* give a value of $f_{gas} = (.059\ ^{+.027}_{-.024})\mathrm{h}^{-3/2}$. If clusters are a fair sample of the matter in the Universe then $\Omega_{baryon}/\Omega_M = f_{gas}$, and the determination of Ω_{baryon} from BBN can be used to infer $\Omega_M = 0.3\mathrm{h}^{-1/2}$.

There is also circumstantial evidence at these scales (clusters and beyond) to believe that Ω_M is significantly greater than Ω_{baryon}. The quantity of structure observed in the present day Universe imposes strong constraints on the nature of the matter within it. There is no viable model for structure formation without a significant nonbaryonic component for the matter. In a baryons-only Universe, density perturbations grow only from the time of decoupling, at z$\sim$ 1000, until the Universe becomes dominated by curvature, at z$\sim \Omega^{-1}_{baryon} \sim 20$. The size of density perturbations inferred from the CMB anisotropy would not have had enough time to grow and form the non-linear structures seen today. With nonbaryonic dark matter, perturbations begin to grow at matter/radiation equality and continue to grow until the present epoch (or nearly so) leading to significantly more growth and making the observed large scale structure consistent with the size of density perturbations inferred from the CMB.

Further evidence for the existence of dark matter is provided by the dynamics of galac-

*In fact, several recent analyses of large cluster samples have confirmed gas fractions in the region $f_{gas} \approx 15 - 20\%$ (see *e.g.* Ref. [115] and references therein).

tic systems *e.g.* the rotation curves of spiral galaxies or the velocity dispersions of dwarf spheroidals. There is not enough luminous matter observed in galaxies to account for their observed kinematics, *e.g.* when the circular velocities of spiral galaxies are measured, it is generally observed that as you measure the rotation velocity away from the centre, it increases until it reaches a constant value. This is in contrast to what is expected for a distribution of matter that corresponds to the luminous (stars + gas) matter in the galaxy.

The smallest scale for which there is evidence of dark matter is that of the Local Group's dwarf spheroidals. Observations of the velocity dispersions in several of these systems [1] have supported for a long time that they are dark matter dominated, with mass to light ratios in the range of 10–100.

1.3 Dark matter candidates

Now that we have reviewed some of the arguments in favour of the existence of a non-baryonic component to the total matter in the Universe, we can turn our attention to the specific nature of this material.

There are many possible dark matter candidates. They range from axions, with a mass $m = 10^{-5}\text{GeV} \approx 9 \times 10^{-72}\text{M}_\odot$, to black holes of mass $m \simeq 10^4\text{M}_\odot$. The basic property of being dark does not clarify its nature. However, there are several categorization schemes which are helpful in organizing the candidates.

We have already examined the first distinction that can be made: Is it baryonic or nonbaryonic? We have been examining evidence that most of the dark matter in the Universe is nonbaryonic. Further evidence against baryonic dark matter (at least to account for the dark matter in our own galaxy) has been provided by micro-lensing studies towards the Large Magellanic Cloud (LMC) [83, 3].

As we have seen in previous sections, there are very compelling arguments in favour of an extra component of matter that is nonbaryonic. Among the nonbaryonic candidates, an important categorization scheme is the "temperature" and interaction nature of the dark matter particles. Hot dark matter (HDM) candidates are particles that were moving at relativistic speeds at the time that galaxies could just start to form. Cold dark matter (CDM) candidates are particles that were moving non-relativistically at that time. Studies of galaxy formation may provide clues as to whether the dark matter is hot or cold. Both HDM and CDM are "collisionless" particles that interact very weakly with themselves

and with baryons. Another possibility is that of "collisional" dark matter in which the particles interact with themselves (but not with the baryons) via the strong force.

The prototype HDM candidate was a light neutrino. If a light ($m_\nu \lesssim$ 100eV) Dirac neutrino exists, its cosmological density would be $\Omega_\nu h^2 \approx m_\nu/93\text{eV}$[74]. N-body simulations of structure formation in a Universe dominated by hot dark matter do not reproduce the observed structure[149] and thus it has been ruled out.

The leading CDM candidates are the axion and weakly–interacting massive particles (WIMPs). Axions are spinless light bosons which appear in QCD models. Laboratory searches, stellar cooling and the dynamics of supernova 1987A all constrain the axion to be very light (less than a few eV) [111]. The window where these particles are viable CDM candidates is getting smaller, but still there is an acceptable range between around 10^{-5} and 10^{-2}eV where they pass all observational constraints (see *e. g.* Ref [14]). WIMPs are stable particles which arise in extensions of the standard model of electroweak interactions. Those discussed most often are heavy fourth–generation Dirac and Majorana neutrinos and the neutralino and sneutrino in supersymmetric models. WIMP masses are typically in the range 100GeV to a few eV, and they have interactions with ordinary matter which are characteristic of the weak interaction.

The most promising WIMP candidates arise within the framework of the Minimal Supersymmetric Standard Model (MSSM). Although these particles interact only weakly with ordinary matter they do have a non-zero cross section for self-interaction and a weak-interaction coupling to ordinary matter. As we shall see in Chapter 4, this opens the possibility to experiments for the detection of dark matter.

Indirect detection may be achieved by observing high energy photons (γ-rays) which are produced when a WIMP particle and its antiparticle meet and annihilate. These γ-rays may be produced with a continuous energy spectrum; when they are a product of the decay of the π^0 mesons produced in jets from WIMP annihilations, or they may be monochromatic; when they arise as the result of two neutralinos directly annihilating into two photons or a photon and a boson. Monochromatic γ-rays would provide an excellent signature for dark matter if they were to be observed at energies of the order of the WIMP mass. Although the detailed form of the encounter for annihilation is difficult to describe concisely, the physics of this interaction (*i.e.* its intrinsic scattering probability) is contained in σ, the cross section for annihilation. If σ is known for an interaction of

particles a with particles b, then we may write

$$n_p = (n_a v) n_b \sigma$$

where n_p is the number of particles produced by the interaction per unit time, n_a the number of "a" particles, n_b the number of "b" particles and v is the relative velocity between them. If we consider only annihilations between the same type of particle ($n_a = n_b = n$) and, if instead of measuring the number of interacting particles we only have an idea of their particle density $\tilde{n}$, then we may rewrite this expression as

$$\tilde{n}_p = (v\sigma)\tilde{n}^2.$$

If we further consider the physical density of the annihilating particles ρ, we arrive at an expression for the total number of products produced after the annihilation of two supersymmetric particles:

$$\tilde{n}_p = (v\sigma)\frac{\rho^2}{m_\chi^2}. \tag{1.2}$$

Here m_χ represents the mass of a supersymmetric particle. The particle characteristics relevant to annihilation are completely contained in the parameter K= $(v\sigma)/m_\chi^2$. The interaction cross section and mass are calculated using techniques developed in QCD for the interaction of baryonic matter in which Feynman diagrams are used to describe all of the possible processes that lead to a specific interaction (see *e.g.* [74] and references therein). In the particular case of the neutralino, the cross section for annihilation has now been calculate both for continuum as well as monochromatic γ-rays (see [13, 138, 12] and references therein). The range of possibilities for the parameter K is large (from $0.007 \times 10^{-30}\mathrm{cm}^3\mathrm{s}^{-1}\mathrm{GeV}^{-2}$ to $\mathrm{K} < 150 \times 10^{-30}\mathrm{cm}^3\mathrm{s}^{-1}\mathrm{GeV}^{-2}$ [12]) therefore, in the absence of further constraints, we shall be using the median value for the velocity averaged cross section of $< \sigma v >= 10^{-30}\mathrm{cm}^3\mathrm{s}^{-1}$.

Direct detection of WIMPs would be the final triumph for dark matter theories. Current searches for dark matter rely on the fact that these particles interact through the weak force with ordinary matter. In many of these experiments, detection is achieved by measuring the slight increase in temperature that is caused within a pure crystal when single WIMPs reach the nuclei of its atoms; the precise increase in temperature depends on the mass of the particle that impacts the nucleus and thus this detection scheme can be used to define precisely the nature of the impacting material. To ensure that there is no spurious heating due the interactions of other particles (such as muons, which are ubiq-

uitous in particle detection experiments) the crystal is isolated in laboratories commonly located many miles under the earth (in unused mine sections).

Despite these efforts at isolating a clear detection their is still the possibility that an increase in temperature of the crystal may be due to something other than WIMP impacts; any detection would then rely on our confidence in the estimates made for the background. How could we eliminate this confusion? Drukier, Frees and Spergel [43] have shown that, due to the Earth's movement around the Sun (and the Sun's movement in the Galaxy) a signal produced by WIMPs would have an annual sinusoidal modulation which peaks in the spring. Thus, observing variations of the crystals temperature increase during the year could provide a clear signal for dark matter.

Recently, Spergel and Steinhardt [124] have proposed the existence of dark matter particles with strong self-interactions. A key feature of these particles (if they are to reproduce important astrophysical features) is that their mean free path is in the range of 1kpc – 1Mpc at the solar radius. This implies that the ratio of their scattering cross sections to their mass must lie in the same range as that for neutrons and protons ($\mathcal{O}(10^{-23}\mathrm{cm}^2\mathrm{GeV}^{-1})$) , implying that natural candidates of this type of dark matter are exotic hadrons — neutral, stable particles that interact through the strong force with themselves but not with ordinary matter. Another possibility is that there is a new type of gluon that arises in supergravity or superstring models. Because these particles have such a large cross section for self-interactions, they are more similar to a gas than to standard cold dark matter (*e.g.* strong interactions now allow the definition of a *dark matter temperature*) which allows it to reproduce astrophysical properties (such as the number of sub-halos in clusters) more effectively that standard cold dark matter.

Progress in fundamental physics may soon tell us whether exotic new particles actually exist, and what their masses and interaction cross–sections are. Calculating how many should survive from the first millisecond and how much they contribute to the dark matter density would then be, in principle, as straightforward as calculating how much helium or deuterium survives from the first few minutes.

No matter what turns out to be the final solution to "the dark matter problem", it is clear that understanding the dynamics of astrophysical systems is very important for a complete description of the Universe. For this reason, in this thesis we shall be concentrating on the dynamical interactions of dark matter dominated systems that we will associate to galaxies and clusters.

1.4 Following the evolution of CDM structure

One of the most intensively studied models for structure formation is based on a Universe dominated by CDM. In particular, a benchmark for comparison with observations has been the so–called "standard CDM model" (sCDM) which involves the following assumptions: the primordial fluctuations are Gaussian and have a power spectrum that is linear [135]: $P(k) \propto k^n$ and $n \approx 1$, the Universe is dynamically dominated by CDM which interacts only gravitationally with other matter, the ratio of total matter/energy density to the critical density of the Universe is unity.

The CDM model has been explored in great detail over the past 20 years through N-body simulations and semi-analytic modelling. An important property of the simulations is that subgalactic-mass halos are the first to collapse and separate out from the expansion of the Universe. These halos then grow either gradually by accreting smaller clumps, or in big jumps by merging with other halos of comparable size. In other words, the formation of structure is hierarchical: small objects form first, larger objects form later. The spectrum of the fluctuation of cold dark matter thus specifies completely the evolution of the dark-matter halos in which, eventually, galaxies will form.

The outcome of these simulations is tested against the data in various ways, such as by comparing the relative amplitude of clustering on different scales with what is actually observed. An uncertainty in comparing such models with the real Universe concerns the relation between the galaxies and the dark matter. This involves complicated gas dynamics, feedback from star formation and other physical processes.

SCDM has now been replaced by ΛCDM (in this model there is an explicit smooth component to the matter/energy density of the Universe $\Omega_\Lambda \approx 0.6$), but the jury is still out on whether this will be the model that prevails. Nevertheless, N-body simulations are currently the best tool to explore the nonlinear evolution and astrophysical properties of a Universe dominated by CDM.

The first numerical studies of collisionless dark matter halo collapses were carried out by Peebles [107] and White [148]. Although the final virialised structure had global mass and size comparable to observed structures, all traces of substructure had vanished. Named the "overmerging" problem, small dark matter structures were initially resolved in the simulations but disrupted as soon as they merged into a more massive structure. This turned out to be a resolution problem [99], and we can now resolve many thousands of dark matter substructure halos orbiting within the virialised extent of cluster, galactic

and sub-galactic halos.

Numerical simulations have now achieved sufficient resolution that allows us to quantify the global and internal structure of dark matter halos. From cluster to sub-halo mass scales, CDM halos are triaxial structures with cuspy singular density profiles that are well fitted by a function of the form [†]:

$$\rho = \frac{\rho_0}{(r/a)^{\gamma}[1+(r/a)^{\alpha}]^{(\beta-\gamma)/\alpha}}. \tag{1.3}$$

A very popular profile (and the one we shall be using most in this work) has $(\alpha, \beta, \gamma) = (1, 3, 1)$ [103].

One of the principle reasons for studying halo–halo interactions is that they may allow us to understand the evolution of galaxies within clusters or satellites within the Milky Way. Galaxies are observed in many different environments, either grouped together to form clusters or weakly clustered in the field. An important part of studying their evolution is to understand what are the principle transformations that they suffer as they orbit within these dense environments.

Galaxies are thought to form at the centre of dark matter halos and, if the halo is large enough, it should dominate the gravitational interaction between galaxies. Thus, by studying idealised halo–halo interactions we hope to understand important factors that influence the evolution of galaxies.

We shall begin with a review of the principle theoretical considerations relevant to N-body interactions. Because it is very difficult to account for all of the dynamical processes which are taking place in a full N-body simulation, we will simulate a simple satellite-halo interaction. Understanding this simulation will help to analyse the more complex interactions that occur during the hierarchical formation of galactic mass or cluster mass CDM halos.

We apply these simple tidal interaction models to explain the possible origin for a particular feature of the diffuse light in the Centaurus cluster. Again, using numerical simulations of the interaction between galactic halos within a cluster.

The most promising CDM particles interact only weakly with ordinary matter. However, they do have a small interaction cross-section for self-annihilation into high energy photons. It is through this process that we hope to detect the presence of dark matter in the Galactic halo by observing a characteristic pattern of gamma-rays across the sky.

[†]A more complete discussion of the particular forms used in this work, and meanings of the constants in this formula can be found in the appendix

We shall use a high resolution simulation of the Local Group to make the first realistic maps of the gamma-rays resulting in the annihilation of dark matter within the halo of the Milky Way.

The ultimate success of the cold dark matter model will be the detection of dark matter particles in the laboratory. By studying the properties of the Local Group simulation and applying the theory of tidal interactions it will be possible to extrapolate beyond the resolution limits of the simulation and make predictions that are interesting for the direct detection of dark matter.

The principle aim of this work is to study the dynamics of CDM halos within halos. By doing this we will be able to see how these interactions can contribute to the origin of observable properties (such as diffuse intracluster light) and how we can use the simulations to make predictions which are relevant to the detection of dark matter.

This thesis is organized as follows: in Chapter 2 we present the main theory for the tidal interactions of halos within halos; then, in Chapter 3, we use N-body simulations to explain the origin of diffuse light in clusters. Chapter 4 contains our detailed use of the simulations to address questions relevant to the detection of dark matter. A short summary of the main conclusions and the work still to be done can be found in Chapter 5.

Chapter 2

Tidal evolution of halos in halos

One of the ultimate aims of an N-body dark matter cosmological simulation is to allow us to make inferences over the bulk properties of galaxies in the Universe such as their positions, masses and sizes. In the hierarchical simulation that we shall be examining in chapter 4 many processes are taking place as it evolves to form the structures which we associate with the Local Group. Some of these processes are truly physical while others are due to the numerical limitations inherent to any computational experiment. It is important to distinguish between these two types of effect if we are to interpret the simulations correctly and apply the results to real astrophysical structures.

In this chapter we shall investigate the simplified dynamical interaction of one halo orbiting within another. First we review the theory of the major processes that occur in such interactions and then we present a high resolution simulation of the evolution of two halos with a 10:1 mass ratio (in which the less massive one is placed on a nearly circular orbit around the other). The lessons learned in this simple satellite-halo interaction will lead us to a better understanding of the more complicated interactions that take place during the hierarchical formation of a cluster, which is more difficult to simulate and complicated to model in complete detail.

2.1 The evolution of N-body systems

There are many processes that occur during the interaction of N-body systems, some of these are artificial; introduced by the limitations of a numerical calculation. Other processes are physical interactions that we should expect to observe in nature. It is important to distinguish between these effects if we are to understand the dynamical evolution of an N-body system.

Among the most important numerical effects are: particle evaporation due to two body relaxation, particle-halo heating and premature tidal disruption due to poor force

and mass resolution. Physical effects include: halo-halo collisions, dynamical friction, tidal stripping and merging.

The particles that make up an N-body system are meant to represent a collisionless fluid (in the particular case of interest here, in which the real particle mass is of the order of the proton mass). That is, each particle evolves in what is assumed to be a smooth background potential. For any real simulation this situation is not exactly true since a typical object is made up of a collection of discrete particles. The potential on each particle is only approximately smooth (it is actually due to the presence of the other particles), and varies each time it experiences a close encounter with any other particle. Over a period of time, called the relaxation time, a particle loses all information of its initial orbit and, if the encounters transfer enough energy to one of the particles, it may become artificially unbound, changing the initial system we are attempting to simulate. Because this effect is slow in nature it has been termed *"particle evaporation"* (See *e.g.* [21]). However it has been shown [142, 99] that two body evaporation is important only for halos with $\lesssim 30$ particles and most modern simulations have much higher resolution than this; nevertheless, this effect could become important if the system loses most of its mass due to other mechanisms such as tidal stripping [78].

As a background particle passes through, or nearby, a halo it distorts the system and increases its internal kinetic energy. Moore *et al.* (in Ref. [99]) conclude that cosmological simulations of individual halos have reached sufficient resolution to avoid this effect.

Although for the present, we are concentrating on the interaction of a single sub-halo within a larger one, when there are many sub-halos an additional heating term arises due to the encounters between them. As in particle-halo heating, the sudden encounter between sub-halos transfers energy impulsively between them. Moore *et al.* [99] estimate that halo-halo heating is an order of magnitude more important than that from heavy particle encounters. The importance of this process has not been investigated in recent high resolution cosmological simulations (we shall see that it is not an important effect).

A pure dark matter N-body simulation attempts to model a system of collisionless particles interacting gravitationally. This is done by replacing the point-like gravitational potential with a *softened potential* in which each particle can be visualised not as an actual particle of dark matter but rather as a bundle of such particles with *softening radius* r_s. In practice, gravitational softening can affect results on a scale of a few softening radii, so we must take this into account when analysing our results.

We shall now turn our attention to some of the physical processes that are present in

the satellite-halo interactions which we will focus on in this thesis.

2.2 Dynamical friction

The term "dynamical friction" was first introduced in 1943 by Chandrasekhar [31] in an attempt to explain the drag experienced by a massive object moving through a smooth background and to distinguish it from the concept of viscosity which was more familiar at that time. He was emphatic in pointing out that the physical ideas underlying each concept were quite different: while viscosity was a result of the shear force of an element of gas over another, dynamical friction pertained to the deceleration that massive objects would suffer due to the trailing density wake of background particles.

Following Binney and Tremaine [21] let us begin by writing down the force a test particle of mass M would experience when moving at speed v at some radius r on a circular orbit within a halo made up of many particles of mass m

$$F = \frac{-4\pi \ln \Lambda \mathrm{G}^2\mathrm{M}^2\rho(\mathrm{r})}{v_c^2}\left[erf(X) - \frac{2}{\sqrt{\pi}}e^{-X}\right] \tag{2.1}$$

here v_c is the speed of circular orbits in the halo, $X = v_c/(\sqrt{2}\sigma)$; with σ the velocity dispersion of the halo, erf() is the error function (see *e.g.* [21]), and $\ln\Lambda$ is known as the Coulomb logarithm which is a measure of the maximum impact parameter b_{max} that should be considered in encounters, $\Lambda \equiv \frac{b_{max}v^2}{G(M+m)}$. b_{max} is roughly the distance at which the density of background particles is much smaller than in the vicinity of the perturber (and we will take it to be the radius of the halo formed by the background). For example, in the case of the interaction between a galactic sized halo and a satellite (which we will be examining) $\ln\Lambda \approx 2$.

We shall consider that the perturber moves within a NFW [103] type halo which has a density profile of the form $\rho(r) = \frac{\rho_o}{(r/a)(1+r/a)^2}$. By Making the approximation that the halo has velocity dispersion $\sigma = v_c/\sqrt{2}$ we may write the force in Eq. (2.1) as

$$\frac{Fr}{M} = \frac{-\ln\Lambda \mathrm{GMr}}{a^2}\left[erf(1) - \frac{2}{\sqrt{\pi}}e^{-1}\right]\frac{1}{(1+r/a)^2}\frac{1}{f(r/a)} \tag{2.2}$$

where a is the *scale radius* and $f(x)$ is a function that results in integrating the NFW profile to obtain the mass*. The force in Eq. (2.2) is tangential to the movement and so affects the dynamics by lowering the angular momentum per unit mass, the rate at which this happens (from the angular momentum at radius r on a given circular orbit

*$f(x) = \ln(1+x) - \frac{x}{1+x}$, see the appendix.

with velocity v; $L = rv$) is:

$$\frac{dL}{dt} = \frac{v_c}{2}\sqrt{\frac{r_{peak}}{rf(r/a)f(r_{peak}/a)}}\left[f(r/a) + \frac{(r/a)^2}{(1+r/a)^2}\right]\frac{dr}{dt}$$

thus,

$$\frac{dL}{dt} = \frac{Fr}{M} \tag{2.3}$$

is an equation for the radius of the perturbing particle with respect to time. This equation may be solved for initial conditions $r(t=0) = r_i$. We shall solve it for the conditions of our simulated halo to follow and compare this analytical prediction with measurements from the simulation.

In the simulations that follow, we will not be evolving point particles within a halo, instead we shall explore the interactions of extended halos orbiting within larger halos that have density profiles similar to those found in cosmological simulations.

2.3 Tidal stripping

Tidal stripping is one of the most important factors that contribute to the dynamical evolution of halos within halos. At a certain radius of any sub-halo the gravitational potential imposed by the parent becomes greater than the self gravitation of the halo. The sub-halo then loses particles which become bound to the deeper potential. As the sub-halo orbits the parent it continually loses mass, and may eventually be completely disrupted depending on how deep its orbit goes into the parent potential and on the number of particles we have to resolve its central core.

Early work on tidal stripping (see *e.g.* Richstone [113] or Merrit [90, 91, 92] and references therein) were based on calculations with halos that were either isothermal spheres or had King profiles. The density profiles of cold dark matter halos have now been studied by many authors including Navarro *et al.* [103, 104], initially for present day halos in a flat cosmology, and now extended to include the effects of cosmology and redshift [45]. These profiles have the form:

$$\rho_{NFW}(r) = \frac{\rho_o}{\frac{r}{a}(1+\frac{r}{a})^2} \tag{2.4}$$

where ρ_o and a are the characteristic density and radius of the halo (more details of the "NFW profile", can be found in the appendix).

We may directly integrate the density profile to obtain the total mass contained within radius r:

$$M(r) = M_{vir} \times \frac{f_{NFW}(x)}{f_{NFW}(c_{NFW})}$$

in this expression,

$$f_{NFW}(x) \equiv \ln(1+x) - \frac{x}{1+x} \quad \text{and} \quad x \equiv \frac{r}{a}$$

and we have introduced the concentration parameter $c_{NFW} = \frac{r_{vir}}{a}$.

By defining the virial mass, M_{vir} to be the mass of a sphere of over-density Δ:

$$M_{vir} = \frac{4\pi}{3}\Delta\dot{\rho}_o r_{vir}^3 \tag{2.5}$$

the structure of the halo may be completely defined by specifying the concentration.

In general Δ depends on the cosmology and may be approximated by (Eke *et al.* [46])

$$\Delta(\Omega,\Lambda) = 178 \begin{cases} \Omega^{0.30}, & \text{if } \Lambda = 0\ ; \\ \Omega^{0.45}, & \text{if } \Omega + \Lambda = 1\ . \end{cases}$$

Eke *et al.* [45] have performed a range of cold dark matter halo simulations and find a convenient relation between the concentration parameter and virial mass of a halo, namely:

$$c_{NFW} \approx 81 \left(\frac{M_{vir}}{h^{-1}M_\odot}\right)^{-0.07} \tag{2.6}$$

Thus, by specifying a cosmology and a halo mass we may completely define its properties.

From these definitions it is straight forward to write the peak circular velocity v_{peak}, orbital frequency ω and potential Φ of an NFW halo as a function of its radius:

$$v_{peak}^2(r) = \frac{GM_{vir}}{a} \times \frac{f_{NFW}(x_{peak})}{x_{peak} f_{NFW}(c_{NFW})}, \tag{2.7}$$

$$\omega_{NFW}^2(r) = \frac{GM_{vir}}{a^3} \times \frac{f_{NFW}(x)}{x^3 f_{NFW}(c_{NFW})}, \tag{2.8}$$

$$\Phi_{NFW}(r) = \frac{GM_{vir}}{a} \times \frac{f_{NFW}(x) + x/(1+x)}{x f_{NFW}(c_{NFW})}. \tag{2.9}$$

Now consider a small halo of mass m and maximum circular velocity v_s moving on a circular orbit of radius R around a large halo of mass M and maximum circular velocity V_P. There will be a radius from the centre of the small halo at which its self gravitation becomes weaker than the tidal force of the large halo, we call this the tidal radius r_t.

To compute it, recall that the force per unit mass of a particle around the small halo at radius r is

$$F_{small}(r) = \frac{Gm(r)}{r^2}$$

and that the tidal force imposed by the large halo is:

$$F_{tidal}(R;r) = \left(2\frac{GM(R)}{R^3} - \frac{G}{R^2}\frac{\partial M(R)}{\partial R}\right) r$$

(Note that both forces are calculated with respect to the small halo centre).

Equating these forces we find an expression for the tidal radius:

$$\left(\frac{R}{r_t}\right)^3 \frac{m(r)}{M(R)} = 2 - \frac{R}{M}\frac{\partial M(R)}{\partial R}$$

which (after substituting the explicit forms for the mass given in 2.7) gives a numerical equation for the tidal radius:

$$\frac{f(x_t)}{f(x_R)} = \left(\frac{x_t}{x_R}\right)^3 \left(\frac{a_s V_P}{a_R v_s}\right)^2 \left[2 - \frac{x_R^2}{(1+x_R)^2 f(x_R)}\right] \tag{2.10}$$

(here $x_t = \frac{r_t}{a_s}$ & $x_R = \frac{R}{a_R}$ and a_s, a_R are the scale radii of the small and large halo, respectively).

At small orbital radii, resonances between the small halo force and the tidal force imposed by the large halo become more important for stripping particles out of the small halo (see *e.g.* , Weinberg [145, 146]). Following Klypin *et al.* [78] we assume that most of the stripping occurs at primary resonance $\omega(r) = \omega(R)$. This leads to a second equation for the tidal radius:

$$\frac{f(x_t)}{f(x_R)} = \left(\frac{x_t}{x_R}\right)^3 \left(\frac{a_s V_P}{a_R v_s}\right)^2 \tag{2.11}$$

Thus, for a particular case we shall take the smaller of the radii found using Eqs. (2.10 & 2.11). We have verified the result of Klypin *et al.* [78] that for $x_R \gtrsim 2$, the equal force condition (2.10) is the most important effect for removing particles. For radii deeper within the potential of the large halo, it is the resonance condition (2.11) that dominates.

In a full cosmological simulation, all of the physical and numerical effects just discussed combine to shape the structures which we associate with astrophysical objects (clusters, groups, galaxies, dwarf galaxies,etc.). In these simulations it is difficult to isolate effects such as stripping, dynamical friction and merging, yet it is necessary to understand them if we are to build a good description of the real physical world.

Observations have reached an unprecedented quality; it is now possible to measure different properties of astrophysical objects such as: the bound mass associated to cluster

galaxies (through weak gravitational lensing), the tidal radii of orbiting galactic satellites (*e.g.* by observing tidal tails from dwarf spheroidal galaxies) and central halo structure using high resolution rotation curves of spiral galaxies. Thus, it becomes relevant to investigate how these properties (bound mass, tidal radius, circular velocity) change with time. When do halos completely disrupt through their interactions within a parent halo? Understanding these processes is particularly important for direct and indirect detection of cold dark matter which we shall explore in detail in the chapter 4.

To answer these questions, and to avoid the complications imposed by a full cosmological simulation, we now perform a high resolution simulation of a single substructure halo orbiting within a larger parent halo.

2.4 A simple satellite-halo interaction

We start by constructing two model dark matter halos which we shall refer to as parent and satellite. The parent halo has the following characteristics: mass $M_{vir} = 1 \times 10^{12} h^{-1} M_{\odot}$, virial radius $R_{vir} = 220 h^{-1}$kpc and peak circular velocity $V_{peak} = 200$ kms^{-1}. The satellite was built to be ten times less massive and its parameters are $r_{vir} = 100 h^{-1}$kpc and $v_{peak} = 95$ kms^{-1}. Both models have a radial density that follows the NFW profile with concentrations $c_{parent} = 11.5$ and $c_{satellite} = 13.5$; consistent with those expected in a ΛCDM cosmology for halos of this mass. The rotation and density curves are plotted in Fig. 2.1.

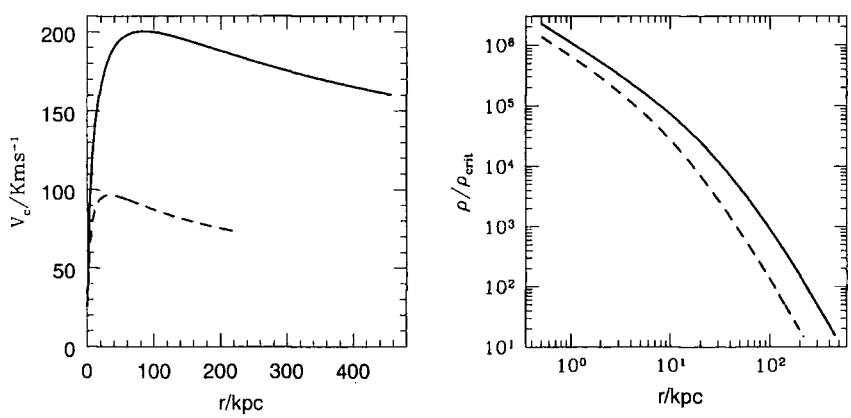

Figure 2.1: The rotation curves: $V_c = \sqrt{GM/r}$ (left panels) and density profiles (right panels) for the two halo models discussed in the text. Solid lines correspond to the parent halo; dashed ones to the satellite.

To build the halos we use the code MakediskGal (Springel, V. private communication) which sets up a collection of particles in equilibrium that follow the NFW profile (this is done by solving the Jeans equation for $\rho(r) = \rho(r)_{NFW}$ and assuming isotropic orbits).

The models are evolved using the parallel treecode "PKDGRAV" (Stadel *et al.*, in preparation). It has an open ended variable time step criteria based upon the local acceleration [110] and uses a spline force softening that is completely Newtonian at twice the softening lengths which, in this case are $r_s = 5$kpc for the parent halo and $r_s = 3$kpc for the satellite.

The satellite is set initially on a circular orbit around the parent at 400kpc. The parent halo particle mass is $\approx 1.0 \times 10^7 M_\odot$ and for the satellite it is $\approx 2.5 \times 10^5 M_\odot$.

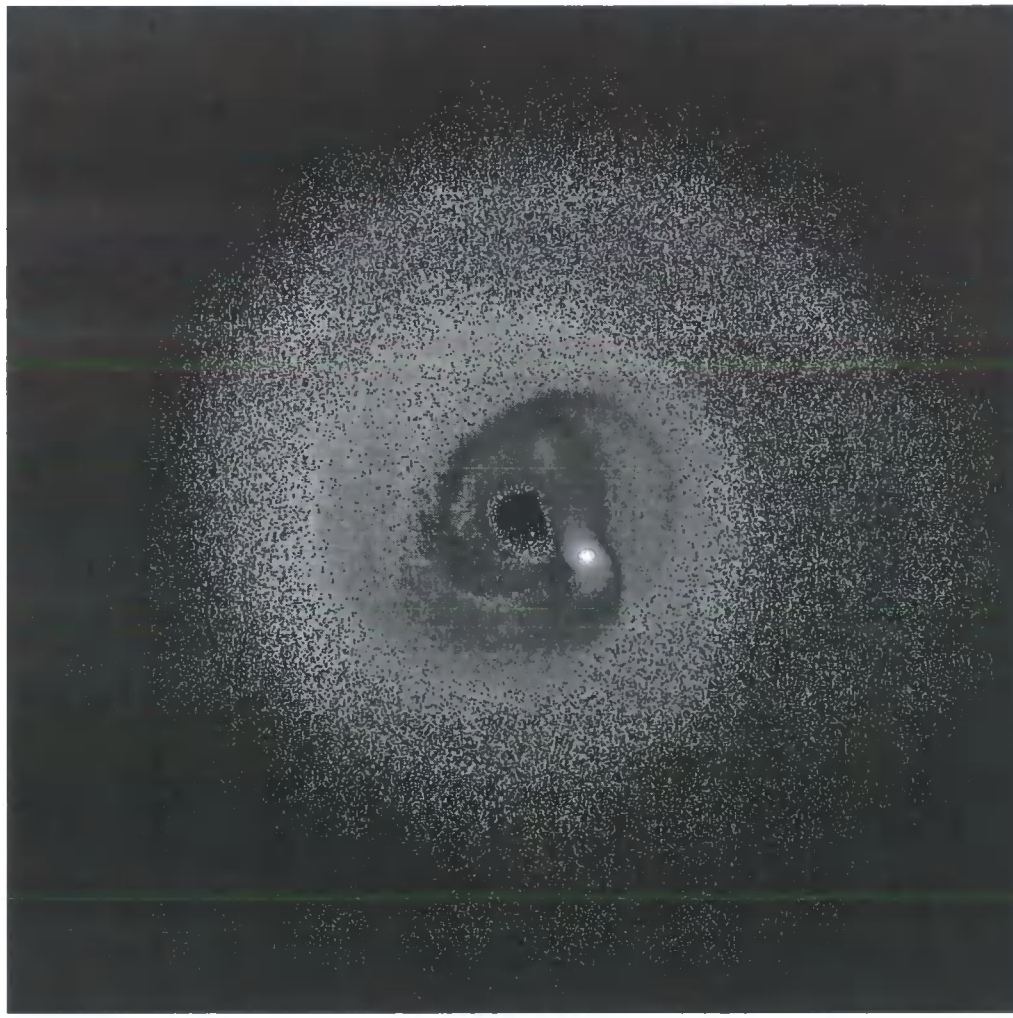

Figure 2.2: A snapshot of the simulation at 20 Gyr as the satellite halo is about to enter the region where it becomes completely disrupted. The image represents the density contrast of the particles from the satellite. For clarity, particles from the larger halo are not plotted.

Figure 2.2 shows a snapshot of the simulation at 20 Gyr. The grey scale represents the local density of particles and for clarity, only the particles in the satellite are plotted. The satellite sinks into the central regions of the parent halo due to dynamical friction.

In Fig. 2.3 we plot the separation between the centres of the parent and satellite halos as a function of time. The points are directly measured from the simulation, both lines are numerical solutions to Eq. 2.3. The dashed line was calculated accounting only for dynamical friction while the solid line also incorporates an estimate of the mass loss due to tidal interactions (as measured from the simulation). Note the presence of "wiggles" in the measure data; they arise because the orbit of the satellite is not exactly circular. The actual time taken for the satellite to sink is almost twice as long as the theoretical estimate without accounting for the mass loss due to tidal stripping. When we account for this mass loss we get a better agreement for the radius of the satellite halos. Thus the Chandrasekhar formalism for dynamical friction is very useful as a first approximation for the amount the satellite halo would sink into the parent (the abrupt deviation beyond 20Gyr could be improved with a more precise model for the stripping).

As the satellite halo orbits the parent, it continually loses mass to the larger halo due to tidal stripping. In Fig. 2.4 we plot the evolution of the total bound mass m_{total}, the peak circular velocity v_{peak}, the radial velocity dispersion σ_{1d} and the maximum radius r_t of the bound particles in the small halo.

From Fig. 2.4 we clearly see that the peak circular velocity v_{peak} of a sub-halo is a fairly stable quantity, thus it can be regarded as a label that identifies and characterises the halo for many Gyr (over 20 Gyrs v_{peak} changes by only $\sim 20\%$ compared to a mass loss of 75%). Also, v_{peak} is the quantity that can be compared most easily with observations (although inferring v_{peak} from the rotation curve or velocity dispersion of the luminous component of a galaxy is not straight forward; *e.g.* , Ref. [103]). Thus, it is of great interest to study the behaviour of this quantity for cosmological simulations (we will do this in chapter 4).

We find that the tidal radius decreases linearly with time and we see an almost perfectly linear mass loss as the satellite gets stripped by the potential of the parent galaxy. We were able to resolve the satellite up to $\approx$ 26Gyr at which time it completely disrupts because we run out of particles to resolve the core. Thus, even at the high resolution used here, we are unable to resolve a massive satellite orbiting within 50 kpc of a galactic mass halo. In the limit of infinite resolution, it should always be possible to resolve a bound core since the density profile is singular.

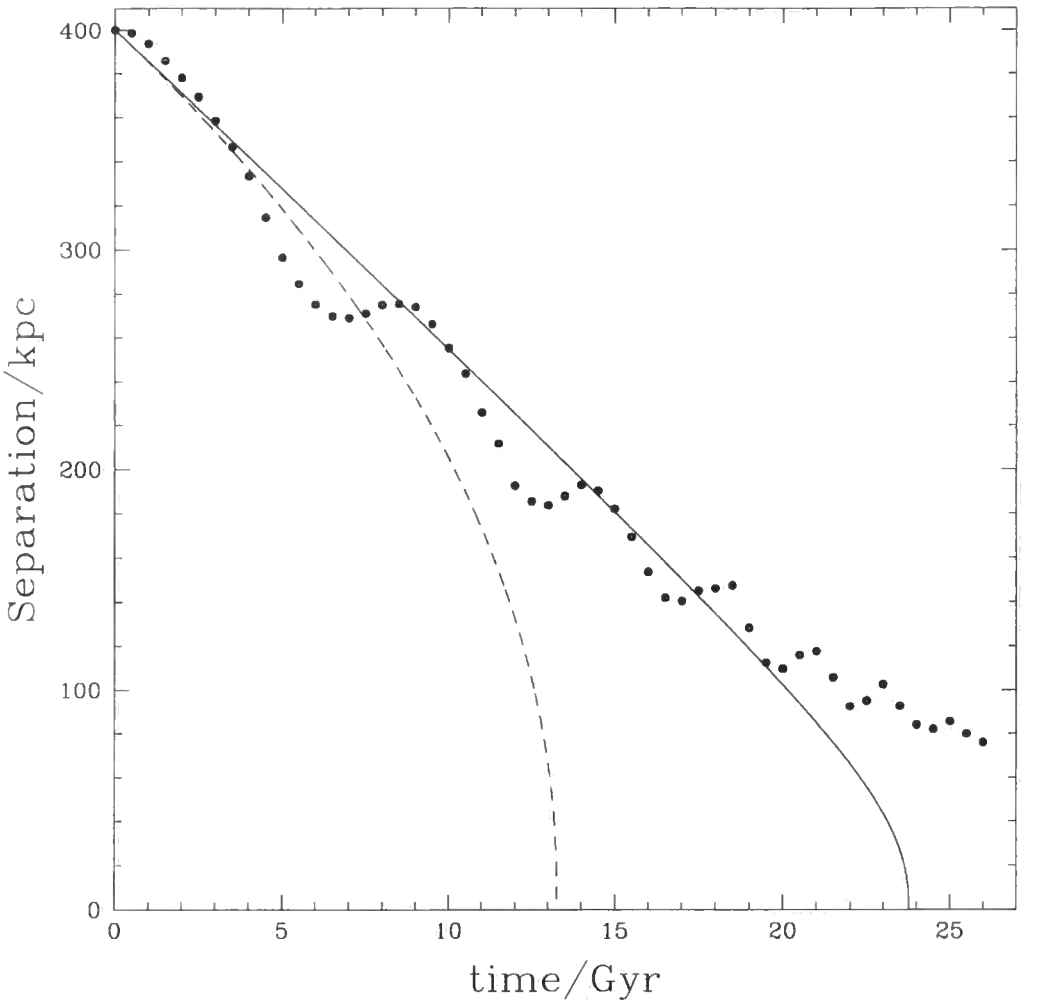

Figure 2.3: This figure shows the orbital decay of the satellite. The dotted points are measured directly from the orbit while the lines are the analytical prediction for the separation; with (dashed line) and without (solid line) accounting for the tidal striping. The presence of the wiggles in the measured decay indicates that the orbit is not exactly circular.

This mass loss and sudden disruption can be understood if we examine the evolution in time of the potential structure of the satellite halo which is plotted in Fig. 2.5. Each curve corresponds to a different time during the simulation, starting with the lower most curve at $t = 0$ and increasing with time, sampling every 2 Gyr in the direction of the arrow, until the end of the simulation (at 26 Gyr). We can see directly how the potential is evolving: initially there is a large potential difference between particles deep in the centre of the satellite with respect to those at its edge, *i.e.* the particles in the core are tightly bound. By the end of the simulation (uppermost curve), the potential at the centre of the

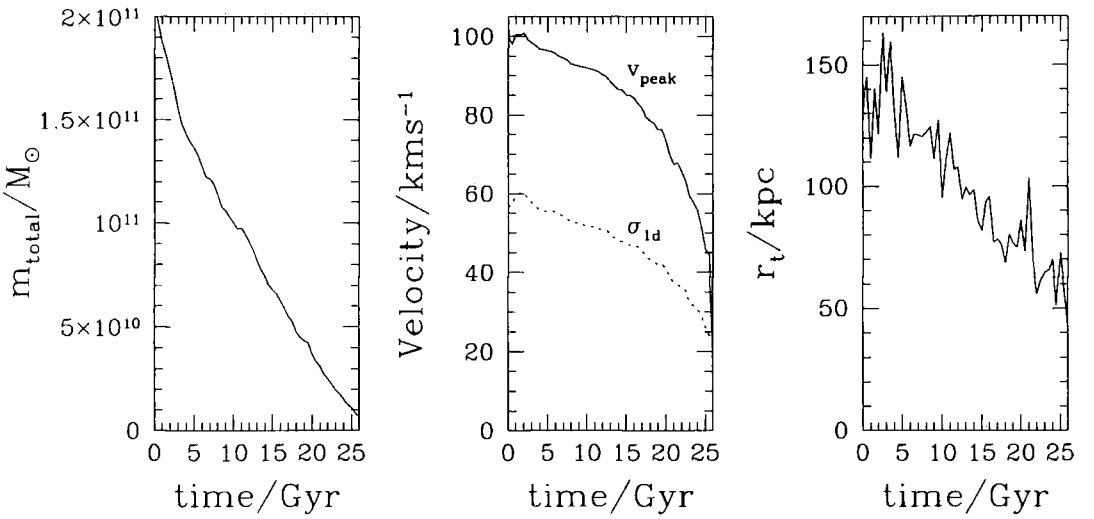

Figure 2.4: The evolution of the satellites bound mass (left panel), peak circular velocity (middle panel, solid curve), radial velocity dispersion (middle panel, dotted curve) and tidal radius (right panel) as discussed in the text.

satellite is almost the same as that at its edge, which means that particles in the satellite need very little energy to escape into the surrounding halo.

Finally, in Fig. 2.6 we plot the difference in potential from the central regions of the satellite halo to that at its edge (measured at the initial virial radius of the halo to be $\Phi_o \approx -4.6 \times 10^{13}$ $M_\odot km^2 s^{-2}$). The difference $\Phi_{bind} = |\Phi(r) - \Phi_o|$ can be viewed as the energy necessary to remove central particles from the halo, *i.e.* a *"binding energy"*. Clearly, as the satellite moves deeper into the potential of the parent halo, less energy is needed to unbind particles from the satellite. In fact, by the final time, the binding energy for the satellite is more than an order of magnitude less than at the start of the simulation. Thus at late times it takes very little energy to completely disrupt a poorly resolved cuspy satellite halo.

For each value of the binding energy we may identify an *escape velocity* v_{escape}. This is defined by assuming the total kinetic energy equivalent to it: $\Phi_{bind} = v^2_{escape} m_{vir}/2$. Figure 2.6 also shows (on the right vertical axis) the escape velocity for the satellite halo. By comparing with Fig. 2.4 we can see that, by the end of the simulation, the random velocity of the particles in the satellite is sufficient to unbind them.

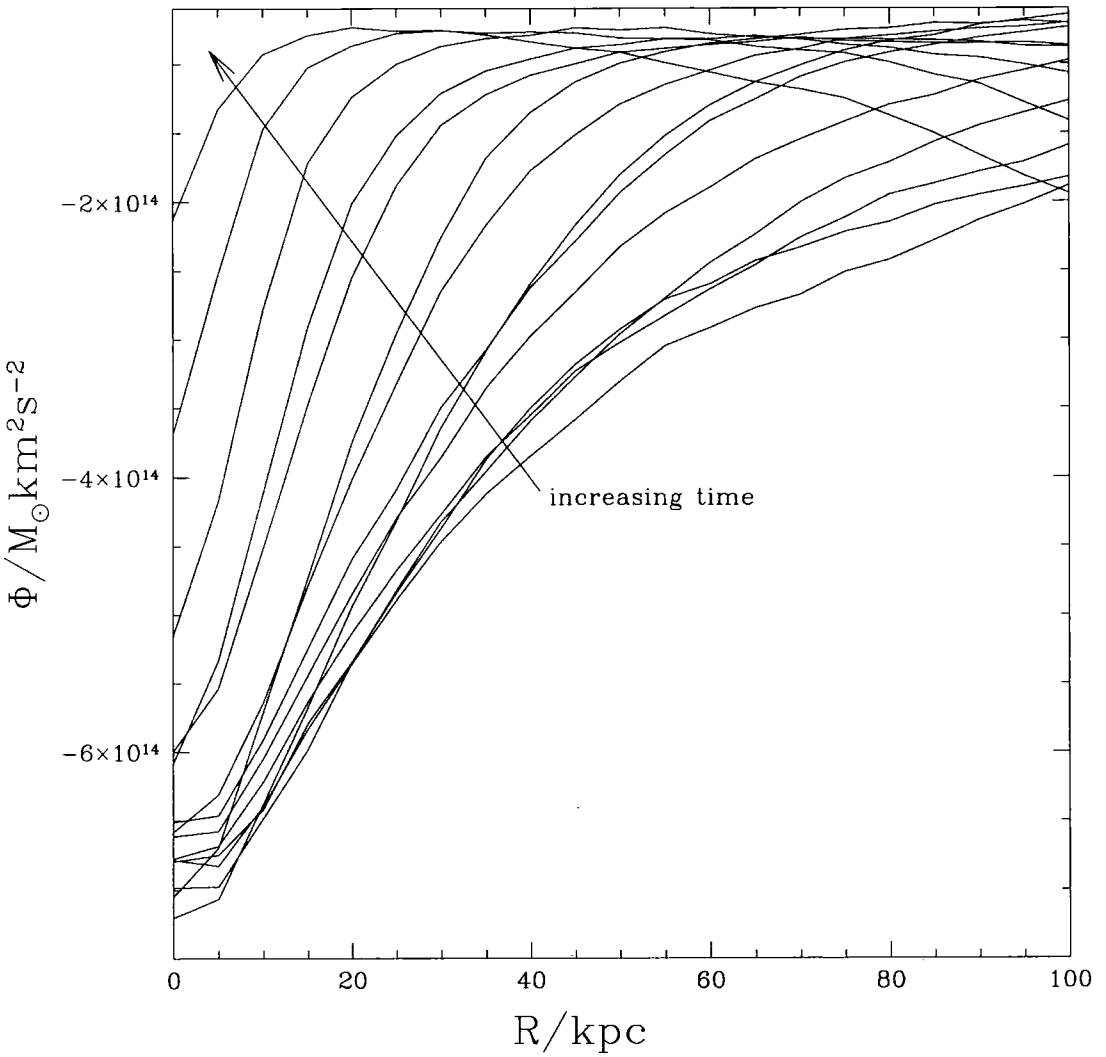

Figure 2.5: The evolution of potential for the satellite halo discussed in the text. The arrow indicates the direction of increasing time

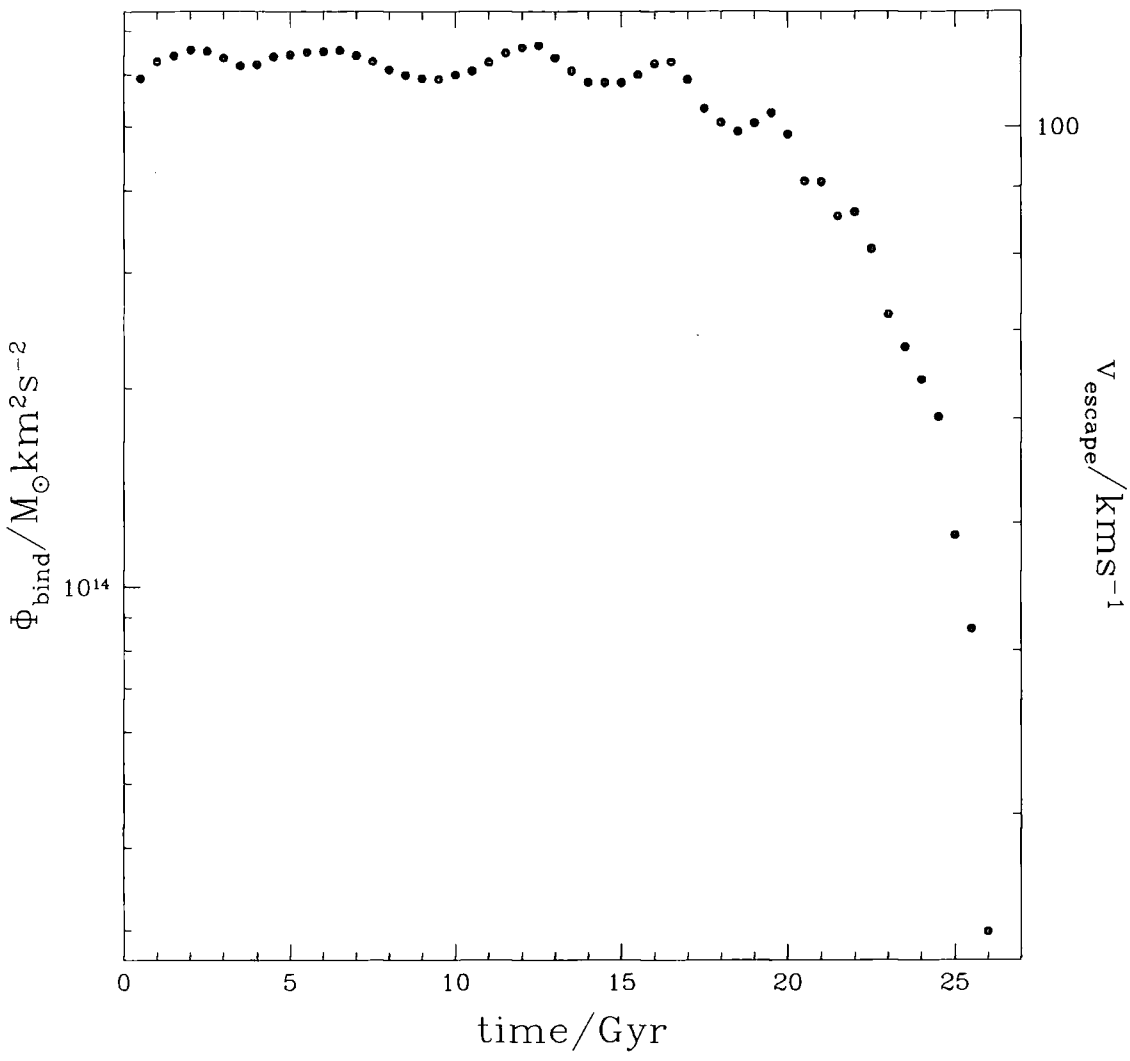

Figure 2.6: The evolution in time of the binding potential Φ_{bind} as defined in the text.

2.5 Summary

By studying a simple interaction of a satellite halo within a parent halo we have been able to learn about the evolution of the main physical characteristics of orbiting N-body halos.

Numerical simulations have reached a level of accuracy such that particle evaporation and particle-halo heating do not play an important role in halo-halo interactions. We were able to resolve an NFW type halo for many orbits during its evolution within another halo of the same type. Dynamical friction and tidal stripping play an important part in the evolution of the sub-halo. As the satellite halo evolves on its orbit dynamical friction causes it to sink towards the centre of the parent, mass loss due to tidal stripping increases

the time it takes to reach the center (compared to how long it would take if the satellite remained intact).

Because their density profiles are singular it should be possible to follow sub-halos for many orbital times, as long as they are built with a sufficient amount of particles. A closer look at Fig. 2.4 reveals that there is a dramatic difference between mass loss and circular velocity evolution for sub-halos. While both the mass and the maximum radius of our satellite halo have an almost linear decline with time we can see that, even after 20 Gyr the peak circular velocity of the satellite has decreased by only $\approx 25\%$. In our simulation, after 26 Gyr, the random velocities of the satellite halo particles were sufficient to break it up. This is a consequence of not having enough particles to resolve the central part of the satellite, more particles would model its potential for a longer time. We also learned that pure dark matter satellites in current cosmological simulations may not survive within the central 20% of the parent halo.

If, as it is hoped, the evolution of halos within halos is a good model for the behaviour of galaxies in clusters, then we have a clear indication that by monitoring σ_{1d} or v_{peak} for these galaxies we are observing a stable characteristic property of that system. We will study the behaviour of v_{peak} for cosmological simulations in chapter 4 to see if we may strengthen these arguments.

Chapter 3

Galaxy destruction and diffuse light in clusters

The most massive virialised dark matter halos are those that surround galaxy clusters. These regions of space are so large that they may even be considered as a fair sample of the matter content of the Universe. With such a dominant dark matter component, it is clear that the dynamics and bulk properties of galaxies within clusters is dominated by the interaction of their dark matter halos.

Now that we have examined the principle processes that occur in a halo-halo encounter we shall turn our attention to a possible observational consequence of an interaction of this type, namely the origin of the intracluster light. By studying the behaviour of a rapid encounter of two halos we shall be able to explain the origin of an astrophysical object that has been a mystery since its discovery more than two decades ago.

3.1 Diffuse light in clusters

Detecting diffuse light in clusters has an enigmatic history spanning several decades [39, 56, 129, 140, 143, 19, 136]. Using either CCDs or photographic imaging, these observations have been plagued by background subtraction, stray light within the telescope and optics, and atmospheric scattering. This has made a quantitative analysis difficult: the total amount of diffuse light, its colour, or its radial distribution have not yet been accurately measured. These techniques have lead to claims that as much as 70% of the light attached to galaxies may lie in a diffuse component. More recently, individual planetary nebulæ have been detected, inbetween cluster galaxies and with redshifts and velocities that place them inside the cluster potential [4, 128, 50]. Deep HST images of the Virgo cluster have also revealed a large population of freely orbiting, red-giant stars [51].

Mergers and slow tidal interactions between galaxies are a well studied phenomenon that can produce dramatic tidal tails of stellar debris (*c.f.* Toomre [130], Barnes & Hernquist [9] and references within). Analysis of dark matter halos within a galaxy

cluster that formed hierarchically has demonstrated that mergers are very rare within rich virialised environments [61]. However, the impulsive and resonant tidal shocks from rapid fly-by encounters between galaxies can also create tidal debris. The cumulative effect of these encounters can cause a dramatic morphological transition between Sc-Sd spirals to dwarf ellipticals/spheroidals [100, 112], whereas low surface brightness galaxies, with lower central densities, can be completely disrupted leading to a possible origin of the diffuse intra-cluster light [98]. This process has been named "galaxy harassment", and extends previous work on slow interactions between galaxies into the impulsive tidal processes that operate in galaxy clusters [92, 141, 69, 101, 44].

In the absence of further perturbations, stars that are tidally removed from galaxies will orbit in narrow streams that trace the orbital path of the galaxy. In a cluster, the star streams will be subsequently heated and mixed on a time-scale of a few crossing times, *i.e.* several billion years. We might therefore expect to find prominent features in the intra-cluster light component from recently disrupted galaxies that have accreted into clusters a few billion years ago. However, with only a couple of documented examples, why are prominent features as bright as these so rare?

The properties of the diffuse light, including its quantity, radial distribution, clumpiness and colour, are of great interest for many reasons. As well as constraining the importance of gravitational interactions as a mechanism for morphological transformation, we have the possibility of using thousands of freely orbiting stars for studying the cluster potential. Understanding the orbital biases of stripped stars and their subsequent evolution within a clumpy potential, will be vital in the interpretation of these velocity data.

Recently, Trentham & Mobasher [131] detected a low surface brightness feature ~ 80 kpc long within the Coma cluster, that may be the result of a high speed encounter between two galaxies. Conselice & Gallagher [33] also find a wealth of fine scale substructure and faint tidal features in a survey of several nearby clusters. Here we "re-discover" a much more spectacular arc of diffuse light that stretches for over 100 kpc near NGC4709 within the Centaurus cluster. The stacked sequence of photographic images by David Malin were first reported very briefly in the Anglo-Australian newsletter by John Lucey over 20 years ago; no further attention has since been given to these data. Using the same techniques Malin has also discovered a second feature that lies near the centre of the Coma cluster that is morphologically similar to the Centaurus arc.

3.2 The images

The Centaurus arc was originally discovered by applying a photographic amplification technique [86] to three plates taken in 1974 by Malcolm Smith at the f/2.66 prime focus of the 4m telescope of the Cerro Tololo Inter-American observatory (CTIO). The photographic emulsion was Eastman Kodak type IIIaJ, hyper-sensitized by baking in nitrogen before use. Photographically amplified positive derivatives from these plates were combined into one image [87] to improve the image quality and minimise processing non-uniformities. The arc was clearly visible on each of the three copies, and its reality was latter confirmed by photographic amplification of IIIaJ plates taken with the 3.9 m Anglo-Australian Telescope and the 1.2 m UK Schmidt telescope.

More recent CCD observations reveal that if this structure lies in the cluster, it is $\sim 120h^{-1}$kpc ($\sim$ 12 arcmin) long and only $1-2h^{-1}$kpc ($\sim 10-15$ arcsec) wide (throughout this chapter $H_0 = 100h$kms^{-1}Mpc^{-1}, h = 1). The arc has very low surface brightness ($\mu_B \gtrsim$ 27.8 mag arcsec^{-2}), is red in colour and points towards the active elliptical galaxy NGC4696. The arc's colour strongly suggests that it is made of stars, so its narrowness is remarkable. The arc is not perfectly straight and has a small curvature along its length.

The top half of Fig. 3.1 shows a negative print of part of the photographically amplified, combined images of the CTIO plates. The arc is the linear feature that extends from the lower left corner (south east) towards the nucleus of NGC4696. The lower image shows the same part of the sky on a single unamplified plate.

The photographs (and CCD frames) show the arc to be diffuse and seemingly devoid of fine structure at the arcsec level. While there are many faint stars and galaxies in the field, there is no apparent enhancement of point-like or diffuse objects along its length. (The point-like source near the centre of the arc is a star). The arc first becomes visible near a small, edge-on S0 galaxy, ESO 322-G102, at a projected distance of about $80h^{-1}$kpc from NCG 4696; the truncation of the arc at this point may be a line-of-sight coincidence, since there is no evidence of any interaction between the arc and ESO 322-G102. Subtraction of the extended light profile of NGC 4696 may reveal the arc on the opposite side of the S0 galaxy.

Spectroscopy of the arc would be extremely difficult in view of its very low surface brightness, however, broadband CCD images of the brightest regions were obtained making it possible to compare the colours of the arc with aged stellar populations. CCD pictures were taken in B, R and I bands with an RCA 350x512 chip at the f/3.3 prime

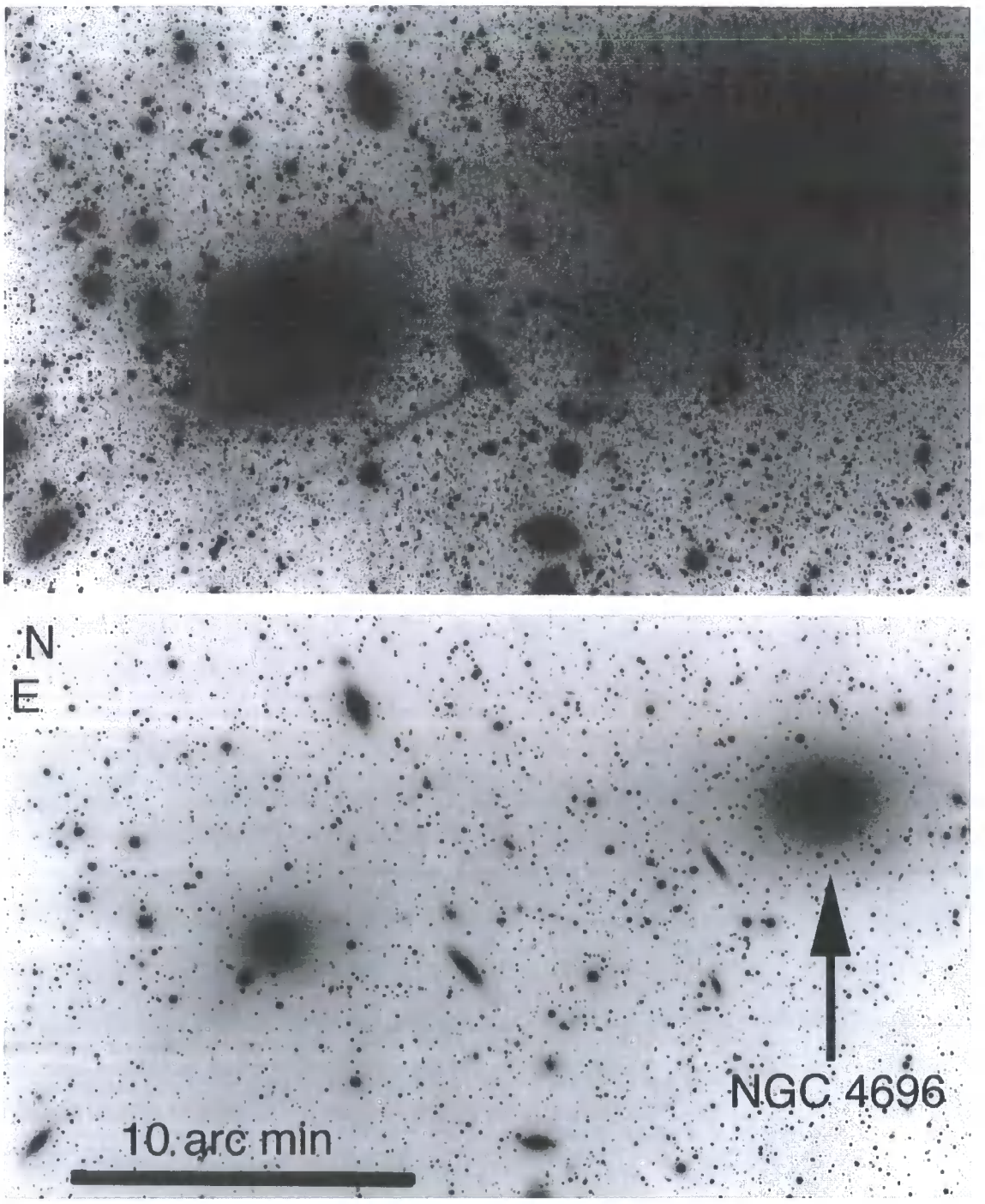

Figure 3.1: A normal contrast image of the core of the Centaurus galaxy cluster with NGC 4696, the brightest galaxy in the cluster, at the upper right (lower panel) and a high-contrast version, with the extremely faint jet-like feature extending towards the lower left corner (upper panel). One arcmin at the distance of Centaurus is approximately $10h^{-1}$kpc.

Surface brightness (mag arcsec^{-2})	Colour (mag)
Arc	
$\mu_B = 27.81 \pm 0.08$	$B - R = +1.72 \pm 0.13$
$\mu_R = 26.09 \pm 0.05$	$R - I = +0.35 \pm 0.22$
$\mu_I = 25.74 \pm 0.17$	
Sky (I frame in twilight)	
$\mu_B = 22.52$	
$\mu_R = 20.76$	
$\mu_I = 18.78$	

Table 3.1: Surface brightness and colours of the arc and sky.

focus of the AAT under photometric conditions on the night of 21/22 June 1990. The CCD scale was 0.49 arcsec/pixel, and the seeing 2 – 3 arcsec. Two sets of overlapping exposures were taken, with total exposure times of 90 minutes in B, 40 minutes in R and 20 minutes in I. Flat fields and bias frames were taken on the same night.

Table 3.1 lists the surface brightness and colours of the arc as measured from the overlap region of the CCD frames. In each case, the mean surface brightness in three regions along the arc was measured, each roughly 5×5 arcsec^2 and free of obvious foreground stars, and six 'sky' regions of similar area straddling the arc and just outside it. The errors quoted in Table 3.1 are 1σ errors on the mean of the three sky-subtracted arc measurements in each filter.

The CCD measurements confirm that the arc is extremely diffuse and very faint, reaching no more than 0.7% of the brightness of the night sky. Further out, the arc is even fainter and we estimate that the faintest parts of the structure revealed by the photographic plates are only 0.1% of the night sky brightness.

The same techniques have also been applied to photographic images of the central regions of the Coma cluster (Abell 1656). These have revealed a feature in the diffuse light, close to NGC 4874, that stretches East-West for at least 5 arcmin, $\sim 150h^{-1}$kpc (Fig. 3.2). It is curved slightly concave to NGC 4874 in a manner very similar to the curve in the Centaurus cluster feature where it appears closest to NGC 4709. The image was made by combining photographically amplified derivatives from three UK Schmidt plates. Two of the plates (J9946 and J10027) were deep IIIa-J (395-550nm) exposures while one was plate OR9945 covering the range 590-700nm. The linear feature is visible

individually on all of the plates, but is much less obvious on the red-light plate. Given the large airmass through which the exposures were necessarily made and the smaller number of plates, this suggests that the surface brightness of the Coma arc is higher than that in the Centaurus cluster. The large airmass has also contributed to the relatively poor seeing in these plates, which is probably why we are unable to confirm the Trentham & Mobasher [131] feature.

The Coma arc is neither as narrow nor as well defined as that in the Centaurus cluster and two resolved galaxies appear to be embedded in the brightest part of it. Given the large number of galaxies in the field, this could be a line-of-sight coincidence, or one of these could be the remnant nucleus of a disrupted galaxy. We note that this feature in Coma was reported independently by Gregg & West [64]. In the absence of CCD photometry of the Coma arc, and its poorer resolution due to its distance, we shall focus our attention on the origin of the Centaurus arc.

3.2.1 Possible origins

The Centaurus arc is unlikely to be foreground reflection nebulosity in our own Galaxy. Malin has used his photographic amplifications technique on many fields containing Galactic nebulosity, and notes that the Centaurus feature (at Galactic latitude 22^o) is morphologically quite different. In particular, it lacks the high-frequency 'crumpling' characteristic of Galactic cirrus and reflection nebulosity. Also, the arc is almost straight (it deviates from a straight line by at most $3-4$ arcsec in the 100 arcsec length covered by the CCD frames) and points at the nucleus of NGC 4696, the brightest galaxy in the Centaurus cluster.

The region of the arc observed with the CCD has colours consistent with those of K0 stars in the (B-R), (R-I) two-colour diagram (Fig. 3.3, from Cousins [35]). If the arc were dominated by optical synchrotron radiation it would be bluer than this, with B-R around 0.7-1.2 as typically seen in BL Lac objects [93] and the M87 jet [127] Whilst the arc might be composed of ionized gas, with most of its light coming from O^{++} and H^{+} ions, very unusual line ratios would be needed to produce the observed colours and it would be difficult to account for the I-band emission. Furthermore, it is hard to imagine a long-lived ionizing source which could operate over such a large distance. If light from the arc originated from emission lines, we would also need to account for the collimation of the ionized gas, or the ionizing beam, or both. We therefore conclude that the arc is probably composed of stars with a mean spectral class of around K0.

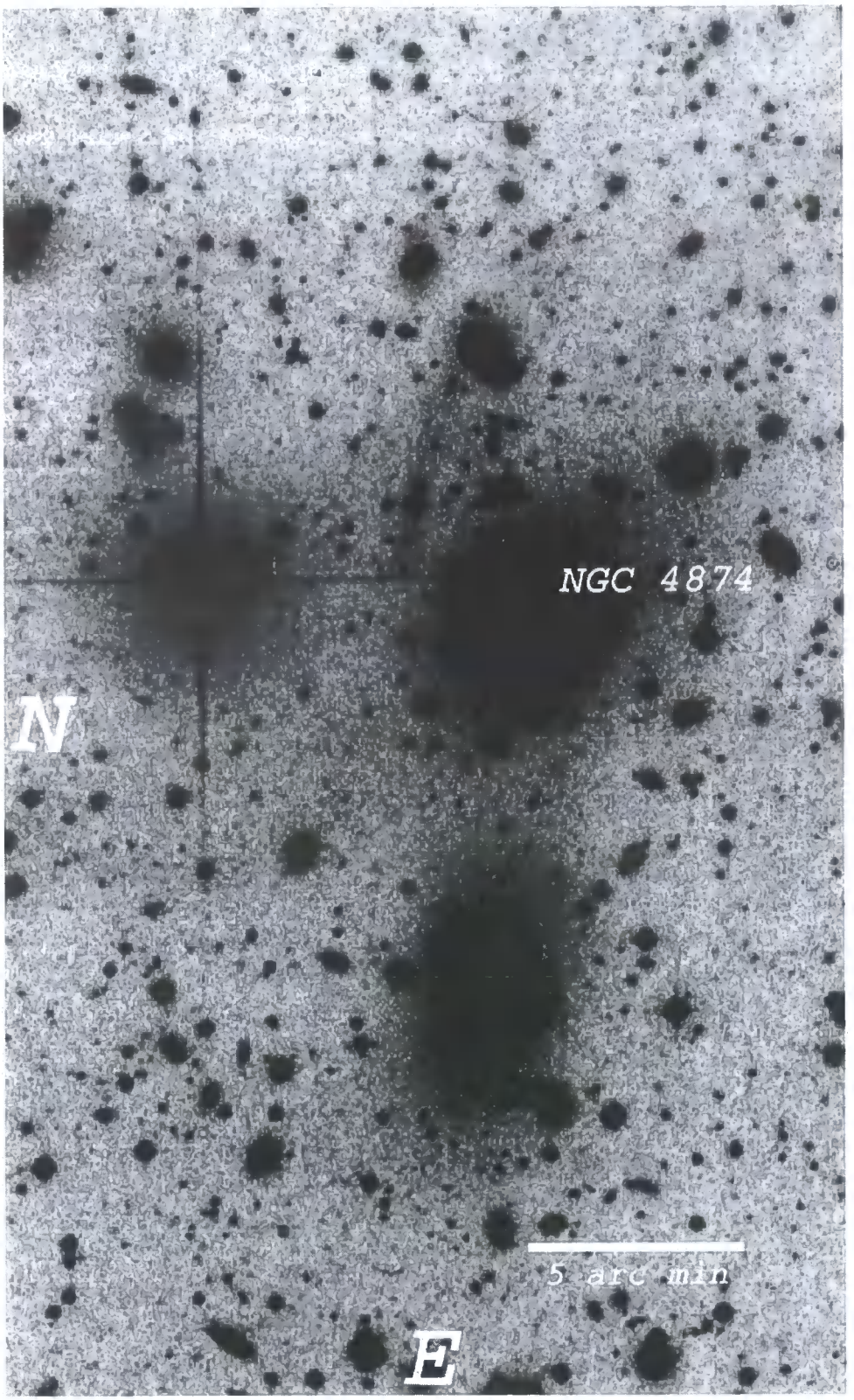

Figure 3.2: A high-contrast image of the core of the Coma galaxy cluster with NGC 4874 at the upper right. One arcmin at the distance of Coma is approximately $30h^{-1}$kpc.

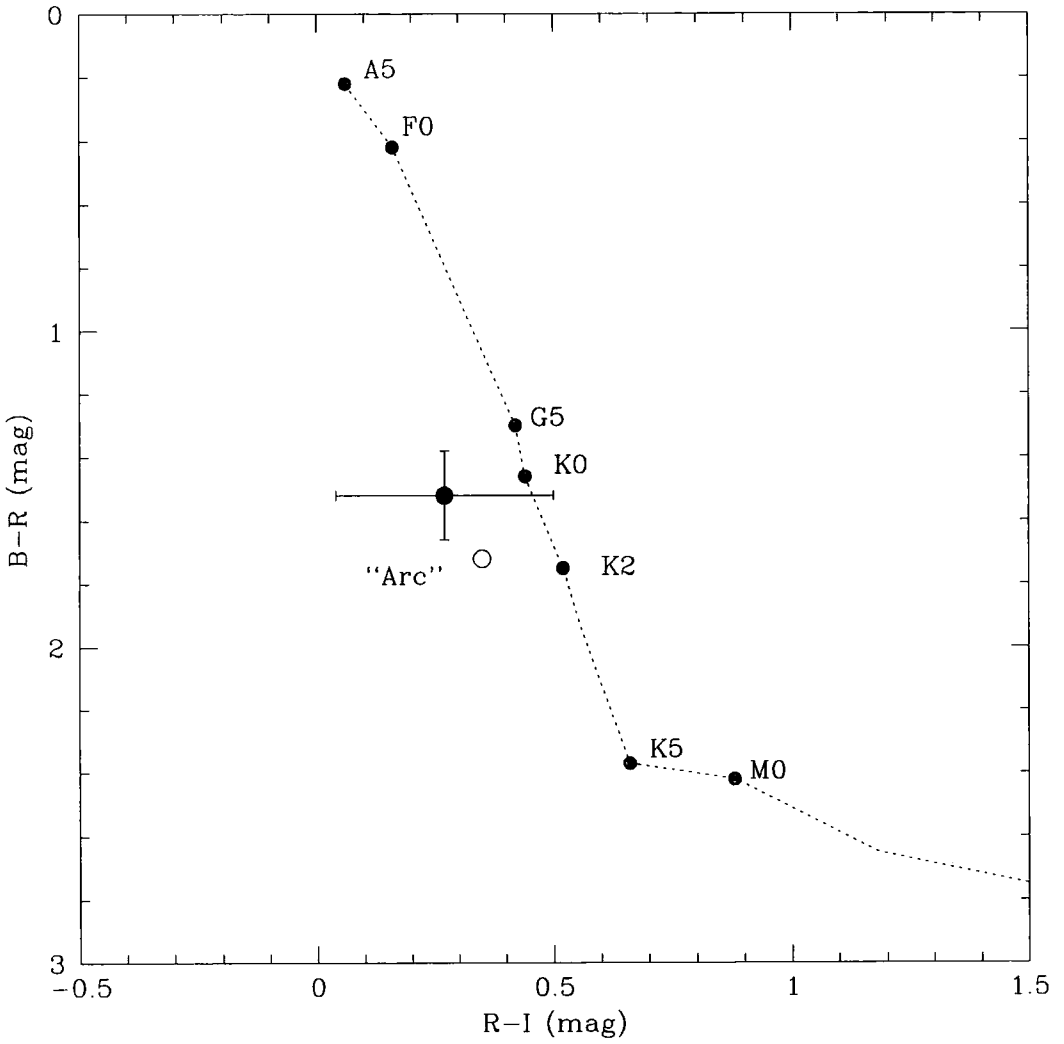

Figure 3.3: The colours of the Centaurus arc compared with those of late-type giant stars. The solid circle is the reddening corrected value, the open circle is the value without this correction.

Could the feature be a gravitational arc from a background galaxy that has been lensed by the combined potential of NGC4696 and NGC4709? In order to produce a gravitationally lensed image this straight, the potential has to be complex, such as would occur in between the combined potential of the two central cDs. Furthermore, a lensed image this close to the massive potential of NGC4709, would produce a much shorter image. Thus, if the mass distribution traces the light distribution to a reasonable extent, then its position and morphology rule out gravitational lensing.

The dimensions of the object rule out a diffuse galaxy that happens to lie along the line of sight – the axial ratios are about sixty to one. If the Centaurus arc is stellar and lies in the cluster, then either the stars formed *in situ*, or they have been removed from one of the cluster galaxies; since no mechanism is known for the former, we shall concentrate on the latter. In either case, the key challenge for any successful model for its origin is to reproduce both the length and narrowness of the feature.

We can estimate the mass of the stars in the arc from its integrated luminosity. Combining measurements of its area and mean surface brightness gives an estimated total B magnitude of 18.4 ± 0.5 for the integrated light. At the distance of the Centaurus cluster (taken here as $26.8 \mathrm{h}^{-1}\mathrm{Mpc}$), this is roughly $4h^{-2} \times 10^7 L_\odot$, corresponding to $8h^{-2} \times 10^7 M_\odot$ if we assume a mass-to-light ratio of $M/L_B = 2$.

The remainder of this chapter will be devoted to investigating the possibility that the Centaurus arc consists of stars that have been tidally stripped from a cluster galaxy. Since the total stellar mass of the arc is just a few percent of the stellar mass of an L_* galaxy we have two possibilities for the progenitor galaxy. It may have originated from a single dwarf galaxy that has been completely disrupted and all the original stars form the 100 kpc streak of light. Alternatively, the observed feature may represent part of the tidal debris that has been torn from a more luminous galaxy. In the latter case, the bulk of the tidal debris may extend beyond the current image and may be detectable at lower surface brightness levels.

3.3 Tides and tails; numerical simulations

3.3.1 Galaxy models

We shall use numerical simulations to investigate the possibility that the Centaurus arc is tidal debris from a gravitational interaction between a galaxy and one of the cD galaxies NGC 4696 or NGC 4709. Given the wide parameter space to explore in both galaxy

morphologies and orbital properties, we shall limit our choice of models to three; dwarf spheroidals, high surface brightness spirals and low surface brightness spirals. Elliptical galaxies are simply too centrally concentrated to lose a great deal of stellar mass. Even if a particularly strong tidal shock unbound some stars, it is unlikely that they would occupy a narrow region of phase space required to produce a feature $\lesssim 2$ kpc across (for which we would have to rely on the ability of the cluster potential to constrain the stripped materials' orbit).

If the Centaurus arc is tidal debris, then its position next to the cluster centre suggests that the potential of one of the massive central cD galaxies was responsible for the disruption. However, we can't rule out the possibility that the encounter took place further from the cluster centre and we are just observing the debris passing pericentre. Rather than treat the full cluster potential and its substructure, we shall model the cD galaxy as a single truncated isothermal dark matter halo with a moderate core radius of 50 kpc (see Fig. 3.4(a)). The dark matter particles that represent the cluster potential have a mass $\sim 10^{10} M_{\odot}$ and softening of 20 kpc. We discuss the effects of a clumpy potential in Section 3.5.

The model galaxies are constructed using the techniques developed by Hernquist[70]. The spheroidal galaxy is constructed as a single stellar system, with a mass distribution shown in Fig. 3.4(b). This is a truncated isothermal distribution of stars with a core radius of 2 kpc, and total mass within 20 kpc of $1.73 \times 10^{11} \mathrm{M}_{\odot}$. This system would have a luminosity $\sim 2\% L_{*}$, therefore we must disrupt the entire galaxy in order to explain the arc. Dwarf spheroidals most probably result from harassed Sc-Sd galaxies, however, they are also the most common type of galaxy in clusters so it is possible that some of these systems are completely disrupted by subsequent strong tidal encounters.

The low surface brightness (LSB) galaxy is modelled on a scaled version of UGC 128 [37], using an exponential stellar disk with scale length $r_d = 10$ kpc and a dark halo with core radius set equal to the disk scale length. Within 3 disk scale lengths, the ratio of dark matter to stars is ~ 4.6.

A characteristic of LSB galaxies is that they have slowly rising rotation curves, indicating that the central regions have almost uniform density. Therefore the central dynamical time-scales remain constant throughout the inner disk and an encounter that is impulsive at the core radius will be impulsive throughout the disk. For this reason, our pre-suspicion was that the LSB galaxy would be the most likely candidate for producing tidal debris most similar to the Centaurus arc.

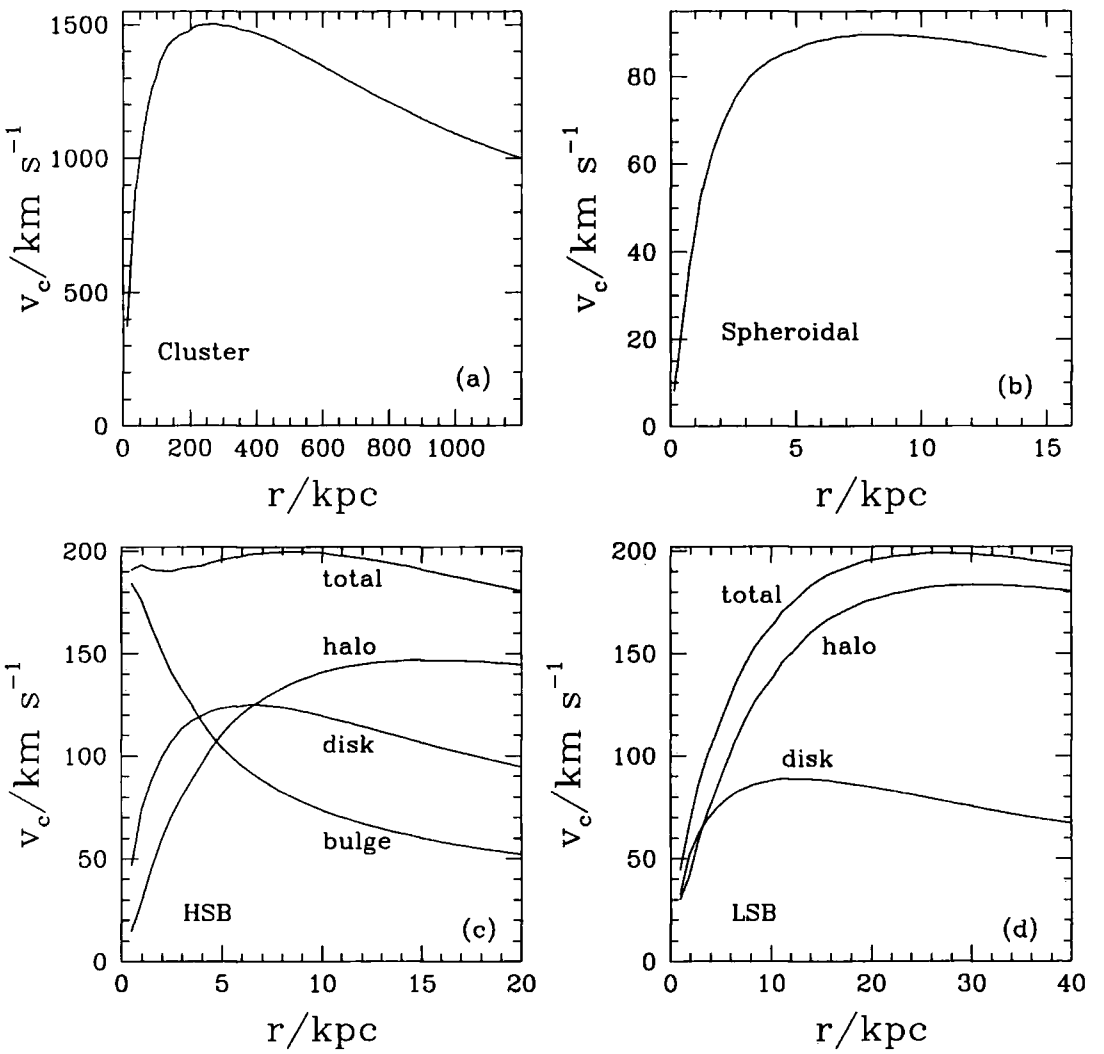

Figure 3.4: The rotation curves $\propto \sqrt{M/r}$ of (a) the cluster, (b) the spheroidal galaxy, (c) the HSB galaxy and (d) the LSB galaxy. The contribution to the rotation curve from the different components of the spiral galaxies are indicated. Note that the HSB and LSB models are constructed to represent observed galactic systems – both have the same peak rotational velocity and lie on the same part of the Tully-Fisher relation, yet have different central mass distributions.

The high surface brightness (HSB) galaxy is similar to the LSB galaxy, except that the disk and halo scale lengths are reduced by a factor of two and we include a bulge with mass $0.25M_{disk}$ such that the rotation curve is flat over the central region (Fig. 3.4(c)). Within 3 disk scale lengths the ratio of dark matter to stars is ~ 1.09.

Both the LSB and HSB disks have scale height $r_z = 0.1r_d$ and are stable with a Toomre parameter $Q = 1.5$. The galaxies have modified isothermal dark matter halos with core radii set equal to r_d. Although both these galaxies have different internal mass distributions, they both have the same total luminosity and their rotation curves both peak at 200kms^{-1}, therefore they both lie at the same point on the Tully-Fisher relation. We use 20,000 star particles in the disk and dark matter halo of the HSB galaxy and twice as many within the LSB galaxy. The softening lengths for these galaxies are set equal to $0.15r_d$ for the star particles and $0.7r_d$ for the halo particles. When we simulate the galaxies in isolation they are stable and remain in equilibrium. To evolve the model galaxies in orbit through the cluster potential we use the parallel treecode "PKDGRAV" (Stadel *et al.* , in preparation).

3.3.2 Orbits

Fixing the orbit in the x-y plane we explore a range of orbital eccentricities, from completely radial to apo:peri=2:1. The more radial the orbit, the stronger the tidal shock and more material will be stripped. However, if the orbit is too radial, the stream may fan out as seen in the simulations of Weil *et al.* [144] and will not produce a long thin tail of stars.

We set the starting position at 1000 kpc for every run and vary the components of velocity using combinations of the following values:

$$v_x = 0, 100, 200, 300, 400, 500$$
$$v_y = 0, 100, 200, 300, 400, 500$$

thus we explore a total of 25 orbits and choose the orbit that produced the longest and thinest tidal debris. We evolve all the runs for 5 Gyr, about two orbital times for this configuration. From these trial runs we found that this was an orbit with $v_x = 400$kms^{-1} $v_y = 300$kms^{-1}, which leads to an $8:1$ orbit, *i.e.*: apocentric and pericentric distances of 1000 kpc and 120 kpc respectively. The velocity at pericentre is ~ 3000kms^{-1}. Note that the impact parameter past the centre of the potential and the velocity at pericentre

determine the strength of the impulsive shock. The starting position and initial velocity could be varied to give a similar impact geometry.

Halos within clusters that form in a hierarchical Universe have a wide range of trajectories; circular orbits are rare and radial orbits are common. Ghigna *et al.* [61] find that 20% of all orbits have apo:peri ratios of at least 10 : 1, therefore the orbit that we have selected as optimum for producing narrow streams of tidal debris, is in fact a typical orbit for a cluster galaxy.

Note that the galaxies are constructed such that their halos extend well beyond the tidal radius, r_t, that would be imposed by the cluster potential at 120 kpc. Using the relation for isothermal spheres $r_t \sim r_{peri} * v_c(\text{galaxy})/v_c(\text{cluster})$, the tidal radii of our models on a circular orbit at 120 kpc would be 8 kpc for the spheroidal and 13 kpc for the spirals. However, the bulk of the stars orbit within these radii, therefore we rely on the impulsive shock as the galaxies move rapidly past pericentre to strip the stars from the central regions.

In Fig. 3.5 we plot snapshots of the spheroidal system at four different epochs. As the galaxy moves in its orbit, many of the halo particles get stripped away, as is apparent from the left hand plots, but upon close examination of the central region we see that most of the material is still bound. After $\sim$ 2.5 Gyr, the stripped stars form long arc like features, but these are not as thin or as bright as that observed within Centaurus.

The orbits of the spiral galaxies have an extra degree of freedom, namely the orientation of the disk as the galaxy moves past pericentre. We shall consider the extreme cases of a disk that is either counter-rotating or co-rotating such that the disk lies in the orbital plane. Figure 3.6 shows the evolution of the HSB galaxy counter-rotating with respect to the orbital direction past pericentre. The first tidal shock occurs after a Gyr, yet even after 1.5 Gyr the disk does not appear to be highly perturbed. After 2.75 Gyrs most of the stars are still orbiting within a thick disk, yet no spiral features remain. At this time the galaxy resembles an S0!

Continued heating of the galaxy after a total of 4 passages past pericentre has not removed a great deal of stars from the galaxy, yet a flattened stellar configuration is only just apparent at late times. By the final time 30% of the stars have been unbound from the disk, however, the stripped stars orbit close to the galaxy and throughout the simulation we never observe long, thin tidal features.

The LSB galaxy on an identical orbit as the HSB galaxy is show in Fig. 3.7. The evolution proceeds in a similar fashion, yet the inner disk is clearly more perturbed and

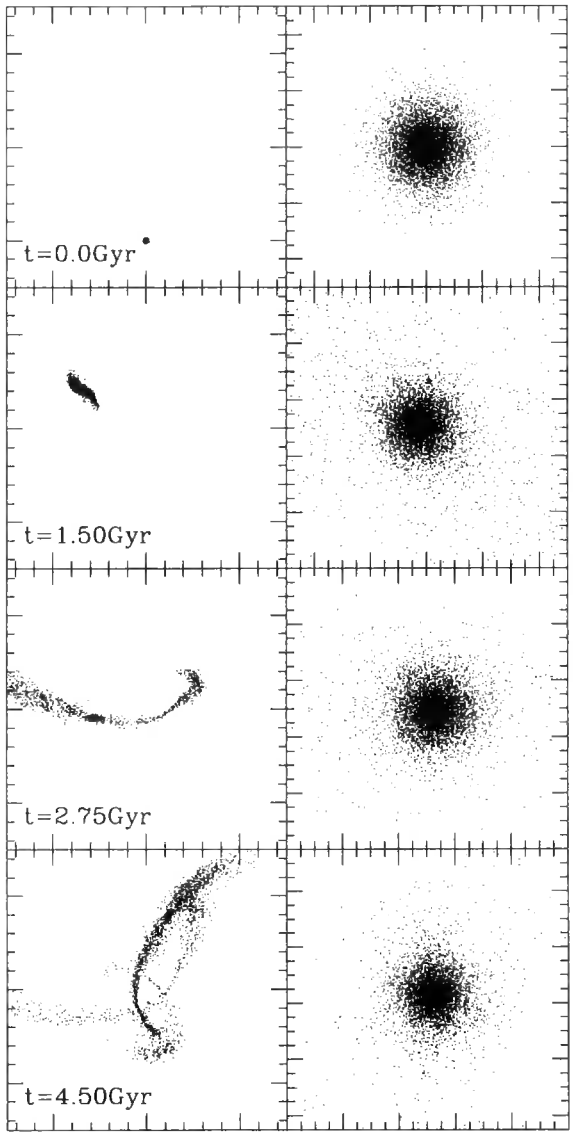

Figure 3.5: The evolution of the spheroidal galaxy on an orbit with apo:peri= 8 : 1. The left hand panels show an area of 3000^2 kpc centred on the cluster potential, while the right hand side is a close-up view (100 kpc on each side) of the centre of the orbiting galaxy. Note that for clarity we plot just 1/5th of the star particles, projected onto the orbital plane and the cluster particles are not plotted to avoid confusion.

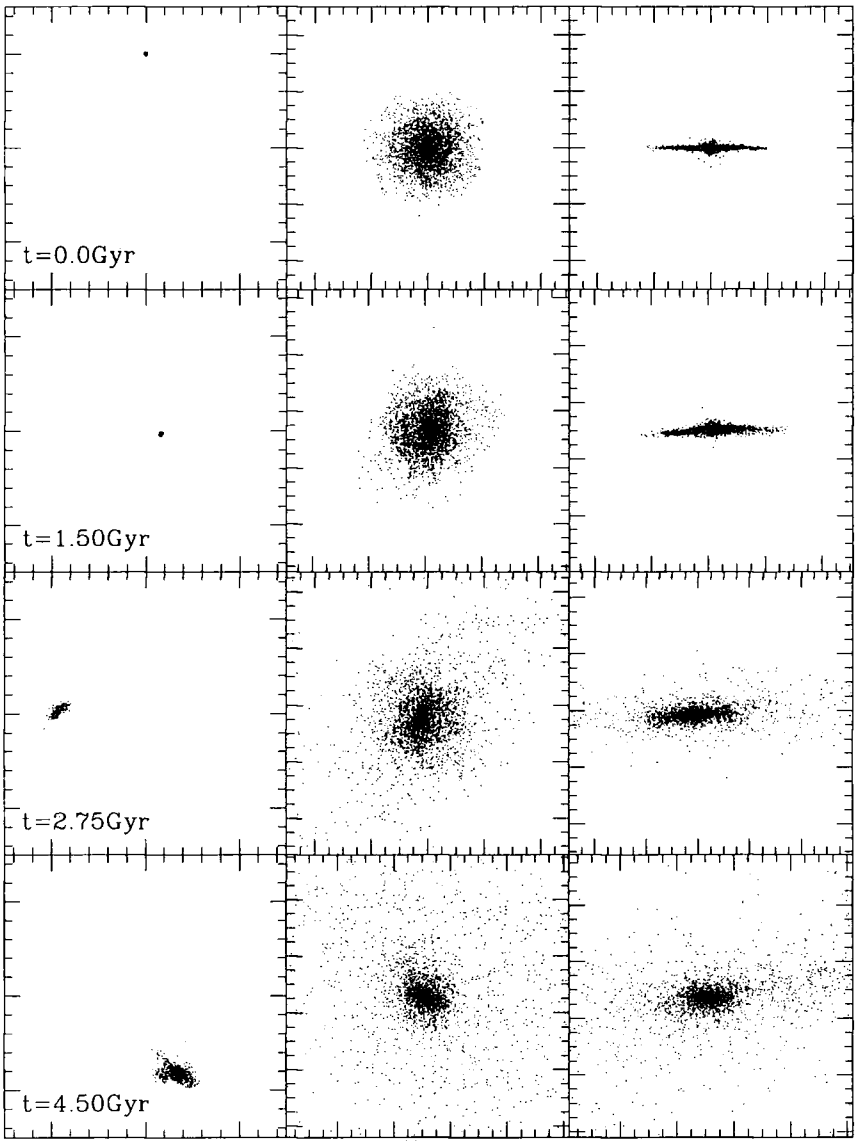

Figure 3.6: The evolution of the HSB galaxy in a counter-rotating orbit. Right panels correspond to a face on and edge on view of the galaxy within a box of 100 kpc on each side, the left panel is the full view of the orbit in a box of 3000^2 kpc centred on the cluster. Cluster particles are not shown.

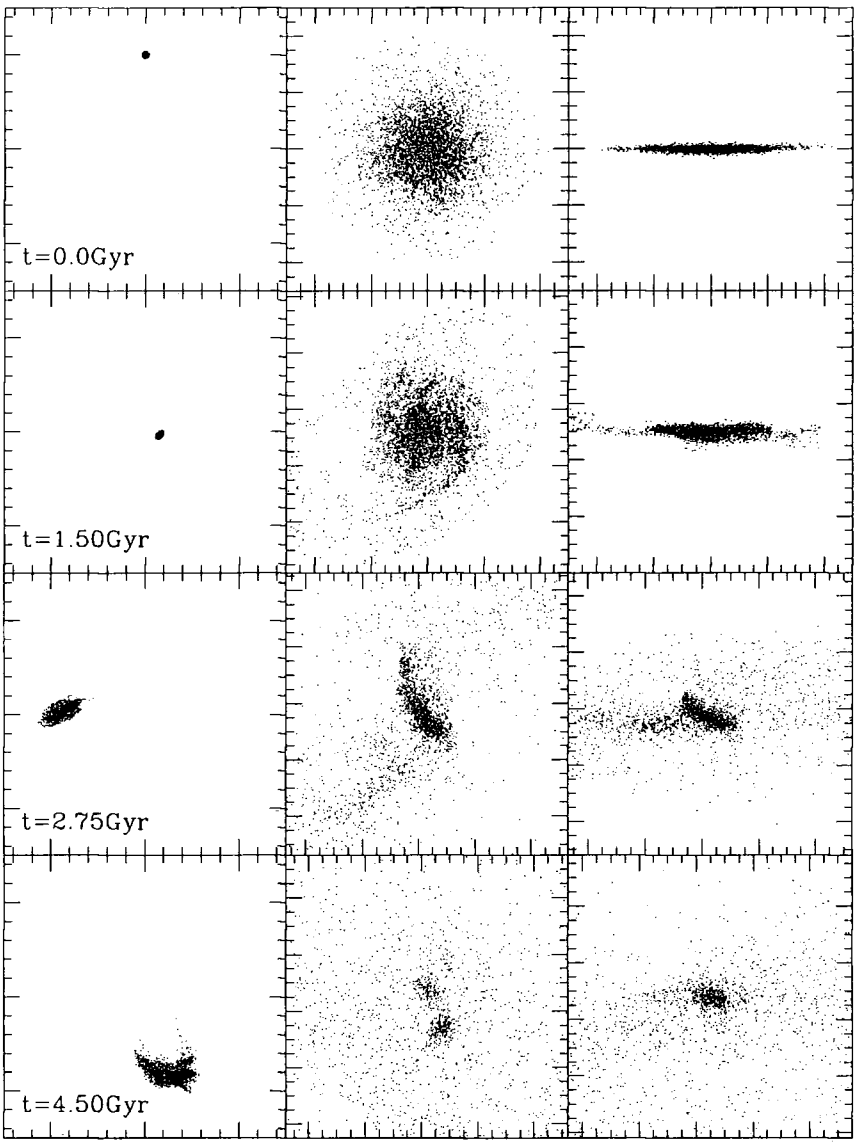

Figure 3.7: The evolution of the LSB galaxy on a counter-rotating orbit. The left panels show the entire orbit centred on the cluster potential in a 3000^2 kpc box. The two right hand panels measure 100 kpc on the side and correspond to a close up view of the galaxy: face on, centre panel and edge on in the right panel.

by the final time, no trace of the original disk structure is apparent. This time, after 2.7 Gyrs 52% of the stars are unbound, yet again we do not find any features that resemble the Centaurus arc, either in dimension or surface brightness.

We now change the direction of the orbit through the cluster potential such that the disk is co-rotating with the galaxy's direction past pericentre. After just 1.5 Gyrs, the morphology of the HSB galaxy shown in Fig. 3.8 has been dramatically altered. Already, most of the disk structure has been destroyed, and the stellar distribution has been significantly heated. However, the most significant change occurs in the morphology of the tidal debris. After 2.75 Gyrs, we start to observe long thin tidal tails of stars that have been symmetrically torn from the disk. Continued heating of the galaxy removes more material from the disk and the tidal tails stretch out further along the orbital path of the galaxy.

The LSB galaxy on a co-rotating orbit, shown in Fig. 3.9, is almost completely destroyed by the tidal forces. After 2.75 Gyrs more than 57% of the disk has been removed and forms long thin tidal tails that stretch for several hundred kpc on either side of the galaxy. By the end of the simulation, just a few percent of the stars remain bound in a configuration that resembles a dwarf spheroidal, with an exponential surface brightness distribution.

The full view of the LSB and HSB co-rotating orbits look very similar; both produce long thin tidal tails. Upon close inspection it is evident that there are particular instances where long "arc like" features are more apparent. The best of these typically occur ~ 2.7 Gyrs after the galaxy enters the cluster, a time when the debris stripped at first passage past pericentre is orbiting past the cluster centre the second time. It is also apparent from Figs. 3.8 and 3.9, that the debris has the narrowest dimension and would be most luminous as it is passing pericentre. At this point, the orbits of the stars bunch up because they are in the deepest part of the potential. It is this section of the tidal debris that we associate with the Centaurus arc that also lies close to the centre of the cluster potential. We illustrate this in Fig. 3.10.

Can we distinguish between these two possibilities? At time $t = 2.75$ Gyrs we extract a 300 kpc length of the stellar debris that is just approaching pericentre. We then project the data and create smoothed density surface density plots and overlay contours of constant surface density.

These density maps are plotted in Fig. 3.11 and demonstrate that debris from both HSB and LSB galaxies can create long ($\gtrsim 200$ kpc) and thin ($\lesssim 8$ kpc) diffuse arc-like

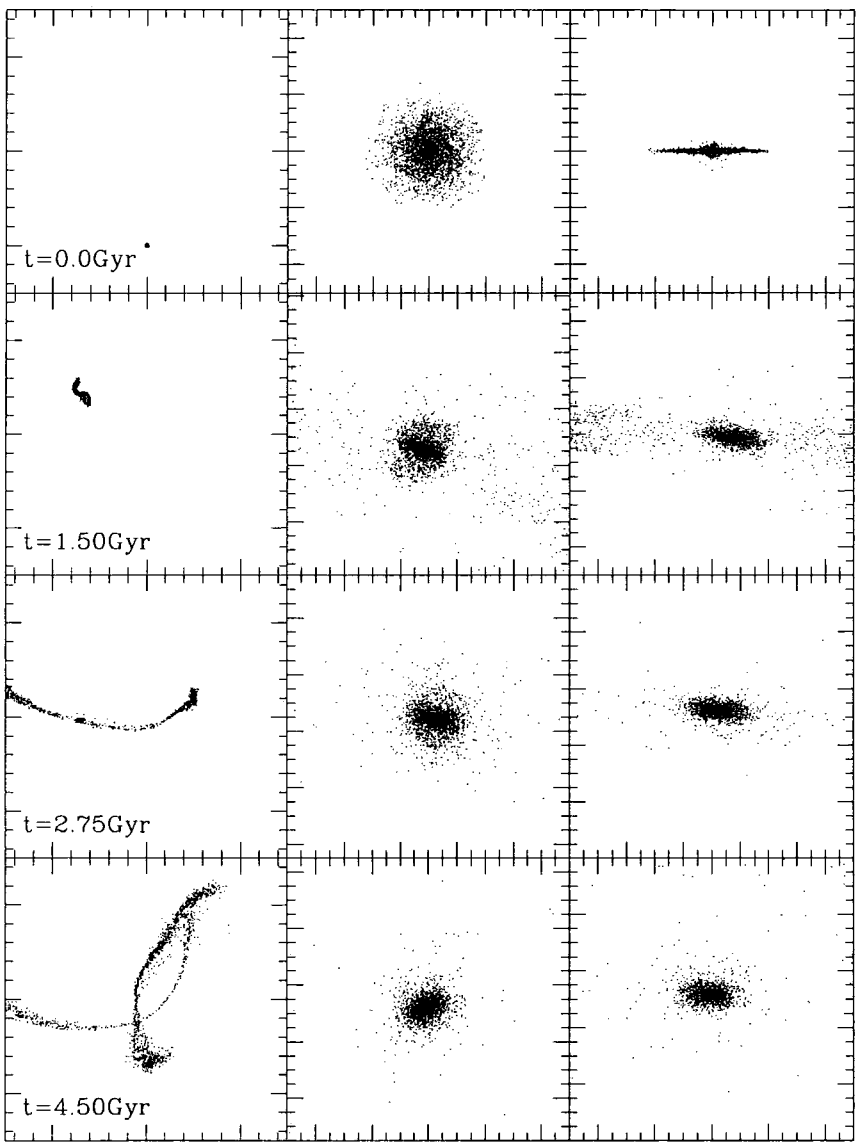

Figure 3.8: As Fig. 3.6, except the HSB galaxy has been placed on a co-rotating orbit.

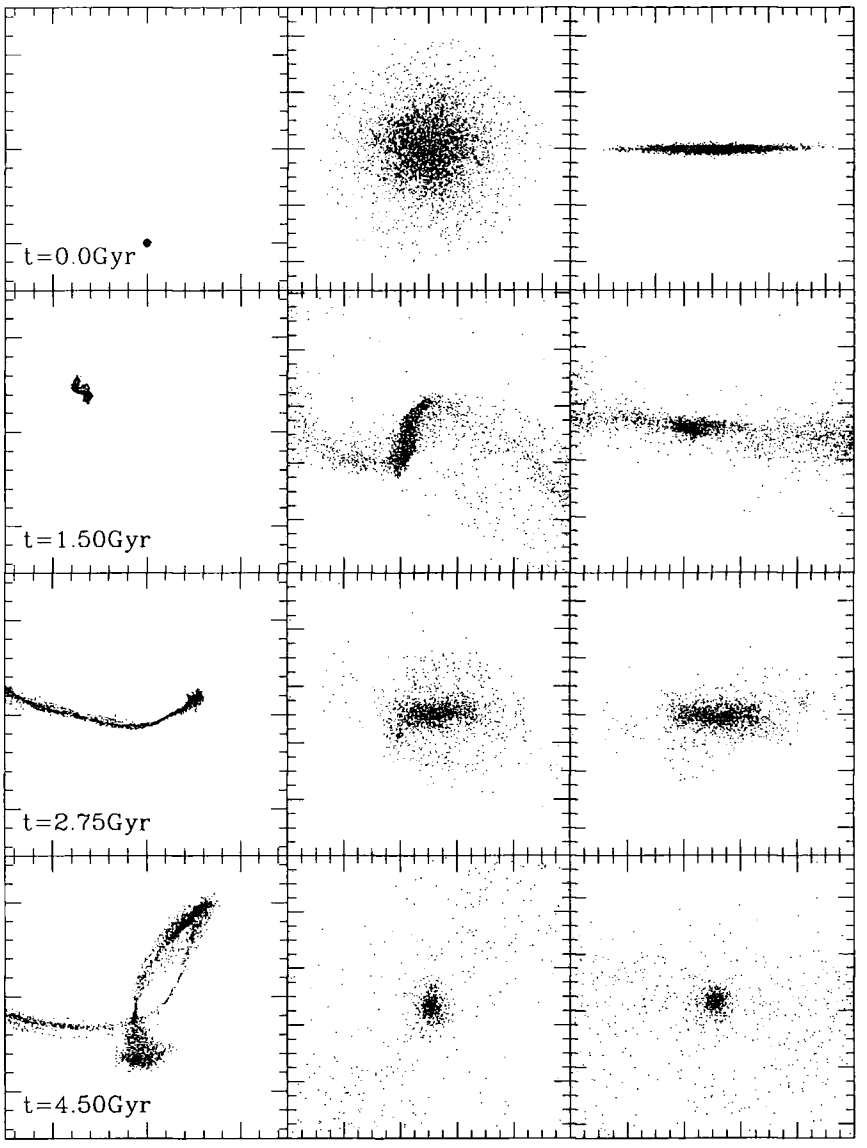

Figure 3.9: As Fig. 3.7, except the LSB galaxy has been placed on a co-rotating orbit.

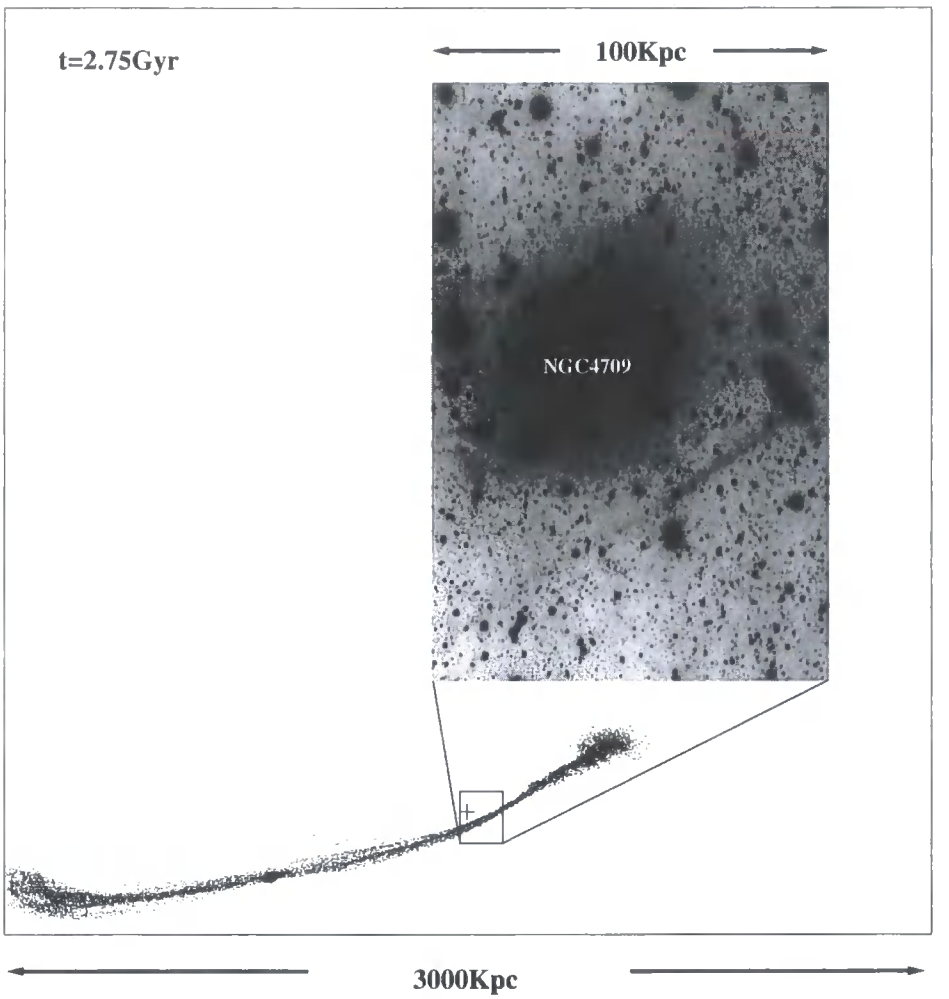

Figure 3.10: An illustration of the part of the tidal debris from the LSB disk galaxy that we associate with the observed arc of light in the Centaurus cluster. The star particles from the LSB galaxy are plotted 2.75 Gyrs after the galaxy enters the cluster, roughly 1.5 Gyrs after the first pericentric passage. These data have been inclined at 30° to the line of sight. At this time, the stellar remnant is approaching pericentre for the second time. The small box centred on the tidal debris shows the part of the stream that we may be observing in the deep image of the Centaurus cluster shown above the tidal debris. The cross in the small box shows the centre of the cluster potential.

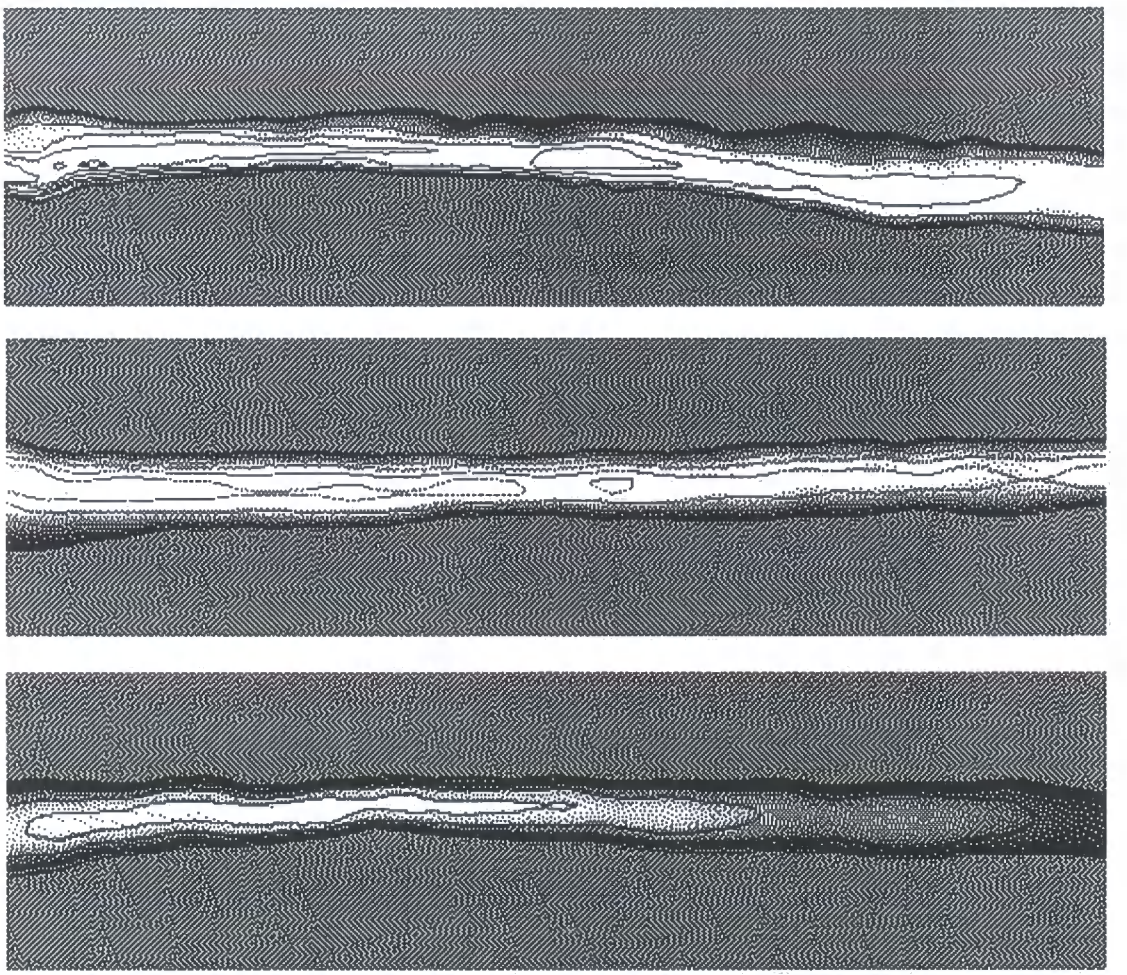

Figure 3.11: Projected density maps of a region 300 kpc by 200 kpc around the thin arc-like structures formed by the LSB and HSB models. The top panel corresponds to the LSB feature viewed at an angle of 15^o from edge on and the middle panel is an edge on view of the same. The bottom panel is an edge on view of the HSB debris. The contours are curves of constant surface brightness in the range $27 - 31$ for the LSB model and $28 - 31$ for the HSB (in blue magnitudes per arcsec^2).

features. These have similar morphological appearance to the Centaurus arc yet differ in their overall surface brightness. The central surface brightness of the inner contour of the LSB galaxy is $\mu_B = 27.85$ arcsec^{-2}, while for the HSB it is $\mu_B = 28.33$ arcsec^{-2}. For this conversion we have assumed a mass to light ratio of $M/L_B = 2$.

3.4 The origin of the Centaurus arc

We now have the necessary results to refine the possible galaxy type and orbital geometry that could have produced the Centaurus arc. Each model was able to produce long arc-like features, but in every case major differences distinguish them.

For the spheroidal model, long streams of debris are obtained, but they are over 3 magnitudes too faint to explain the Centaurus arc. Even after several passages past pericentre, most of the material remains bound to the galaxy. We would require the entire spheroidal to be disrupted into a single smooth stream of length ~ 100 kpc in order to explain this feature. We were unable to achieve this.

Spiral galaxies can have luminosities much larger than the fainter spheroidal systems, therefore a smaller fraction of their stars can be stripped to form observable debris. We find a strong dependence upon the amount of material stripped and its subsequent orbital path through the cluster, with the relative motion of the disk stars as the system moves past pericentre. A larger fraction of stars were stripped from disks that are co-rotating with their orbit, and the stripped stars formed long narrow streams that resembled the Centaurus arc.

We can understand why this happens by considering the relevant dynamical time-scales. The impulsive shock occurs on a time-scale $t_o = 2r_p/v_i$ Gyrs, where the impact velocity of the galaxy is $v_i = 3000$kms^{-1} as it moves past pericentre $r_p = 120$ kpc. We can compare this time-scale with the time it takes for the disk stars to make half a revolution within the core radius of the galaxy, r_{core}, $t_i = \pi r_{core}/v_c$, where $v_c = 200$kms^{-1}. For the particular galaxy and orbit simulated here, $t_i \sim t_o = 0.1$ Gyrs. If the disk is co-rotating, then the encounter occurs at a resonance, whereas a counter-rotating orbit gives time for the central disk stars to respond adiabatically to the encounter.

The LSB is particularly affected by the resonance since the dynamical time within the core radius is constant (due to the constant density of the mass distribution within a disk scale length). Therefore the entire disk is affected by the tidal shock. The HSB galaxy also has a resonance, but only at a single annuli in the disk since the dynamical

time increases linearly with radius. This explains why both the disk galaxies produced long thin tails of debris, but those from the LSB galaxy are much brighter since it lost a great deal more mass with only 17% remaining bound.

Our simulations showed that the orbits of the stripped stars move closer together as they move through pericentre. This creates the appearance of a "standing wave" near the cluster centre, where the surface brightness of the debris is significantly enhanced.

We can understand why the orbits bunch together near pericentre and make a rough quantitative estimate of the enhancement in surface brightness as follows: Consider two stars in circular orbits near the cluster centre at distances r_{a1} and r_{a2}, separated by a small radial distance Δr_a. What happens to the separation of the particles as we move the orbits further out into the cluster, but preserve the small energy difference between the two particles? Now the particles orbit at distances r_{p1} and r_{p2}, this time separated by Δr_p.

The total energy of each orbit (E_i) is conserved and equal to $E_i = K_i + \Phi_i$ Where K_i is the kinetic energy term for each orbit and $\Phi_i = 2\sigma^2 ln\frac{r_i}{R}$* its corresponding potential energy. Because we are dealing with an isothermal potential, all circular orbits have the same kinetic energy, therefore the difference in total energy for each pair of orbits is given by:

$$|\Delta E_A| = |\Phi_A| = |2\sigma^2 ln(r_{a2}/r_{a1})|$$
$$|\Delta E_P| = |\Phi_P| = |2\sigma^2 ln(r_{p2}/r_{p1})|$$

If the energy difference of both orbits is the same then

$$|\Delta E_A| = |\Delta E_P|$$

$$ln(r_{a2}/r_{a1}) = ln(r_{p2}/r_{p1})$$

which leads to

$$\Delta r_a = (r_{a1}/r_{p1})\Delta r_p.$$

Thus for a given energy difference; orbits tend to get closer together as they move towards the central regions of the potential. For an orbit with apo:peri of 10:1, the enhancement of the surface brightness the tidal stream will be roughly a factor of 10 at pericentre.

*Note that we have use a *truncated* isothermal spherical potential where σ is the constant velocity dispersion and R is the truncation radius.

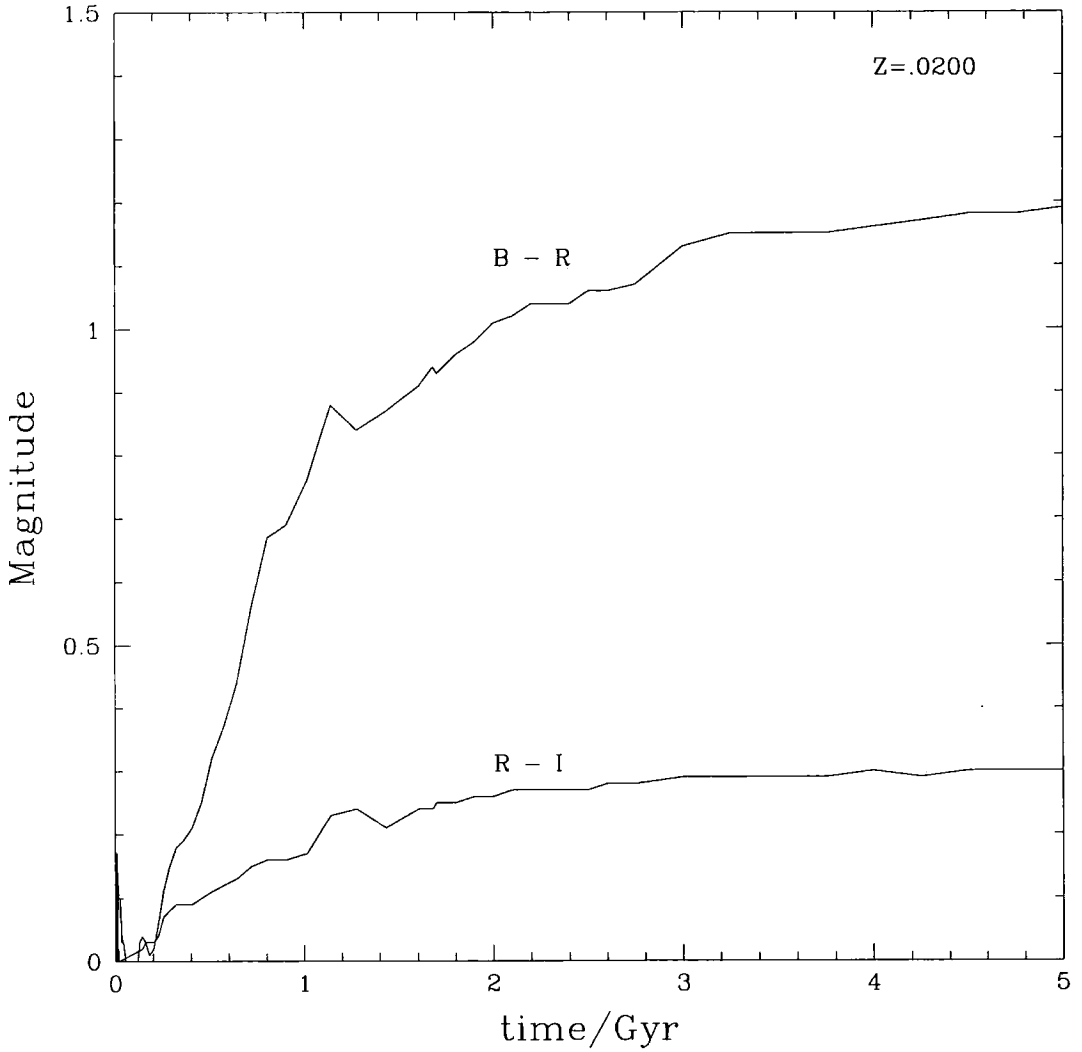

Figure 3.12: Colour fading as a function of time for B-R and R-I colour differences.

	Ellipticals	Sab's	Scd's	LSB
B-R	1.48	1.04	0.86	0.78
R-I	0.57	0.57	0.43	0.49

Table 3.2: Typical colour differences for different galaxy morphologies.

Further support for stellar debris of a galactic origin can be found by considering the colours of the Centaurus arc. In Table 3.2 we give typical colour differences for galaxies of different morphologies across the Hubble diagram [56, 38]. Once the stars are removed from the galaxy, star formation will be abruptly halted and the stars will fade in a predictable manner. Figure 3.12 shows how the colour indices fade with time for a given stellar population with known metallicity and IMF [24].

The tidal tails match the appearance of the Centaurus arc $\sim$ 1Gyr after being stripped from the model galaxies, i.e. the time since the first passage past pericentre. After a Gyr, the amount of fading will be 0.77 and 0.17 for B-R and R-I, respectively. We now reconsider the observed values for the arc (see Table 3.1). We add a further correction for galactic dust reddening using the data of Burstein & Heiles [28] and Schlegel *et al.* [116]; this brings the values of the colours to:

$$B - R = 1.52 \pm 0.14$$
$$R - I = 0.27 \pm 0.23$$

If we take into account the amount of fading over one Gyr, then the initial stellar colours of the stars in the arc would have been $B-R = 0.75$ and $R-I = 0.10$. These colours, within the uncertainties, are consistent with late type spirals and LSB disk galaxies, providing further support for our model.

3.5 Conclusions

Deep photographic and CCD observations of the Centaurus cluster revealed a spectacular arc of diffuse light. This feature is remarkable given its length and narrowness, $\sim$ 12 arcmin $\equiv 120h^{-1}$ kpc long and $\sim$ 10 arcsec $\equiv 2h^{-1}$ kpc wide. The arc is diffuse with no apparent structure and its colours indicate that it is made of stars. The estimated total mass from its integrated luminosity is $\sim 8h^{-2} \times 10^7 M_\odot$ and its surface brightness (in mag arcsec^{-2}) is $\mu_B = 27.8$; $\mu_R = 26.1$; in the R band and $\mu_I = 25.7$, in the I band. Several possible scenarios for its origin, including foreground reflection nebulæ , gravitational

lensing or a radio jet, are rejected in favor of a gravitational tidal interaction that created an arc of stellar debris. A second feature with similar morphology is also revealed within the central region of the Coma cluster.

We used numerical simulations to investigate the response of galaxies of different morphologies to tidal shocks as they pass pericentre in a cluster potential. Spheroidal, HSB and LSB galaxy models were evolved on orbits through a smooth cluster potential. From many different trial orbits, a galaxy moving through the cluster within apocentre:pericentre of 8:1 produced the narrowest, longest and brightest tidal tails. This orbit is typical for galaxies orbiting in clusters that form within hierarchical clustering models [61].

Even though the parameter space is large, we can effectively eliminate spheroidal or high surface brightness spiral galaxies from the possible list of harassed galaxies. The spheroidal galaxy loses only about 15% of its central mass to the cluster and the features formed are wide and extremely diffuse and would not be observable. In the case of the HSB model, only about 30% of its stellar mass is lost during the simulation, and although long thin arc like debris are produced they are also fainter than the Centaurus arc.

The only models that can produce tidal features this long and thin are disk galaxies. Moreover, in order to reproduce the surface brightness of the Centaurus feature, the galaxy must be a massive LSB galaxy with a luminosity close to L_*. In addition to the well defined morphology, we are also forced to use orbits that place the disk in the global orbital plane and the disk must be rotating in a prograde sense, co-rotating with the orbital path past pericentre. This encounter geometry produces the maximum resonant stripping of disk material - almost ninety percent of the disk is removed yet just a few percent constitutes the luminous part of the debris that we associate with the Centaurus arc. Although the tidal debris from a single galaxy can span the entire cluster, as the stars move past pericentre, their orbits move closer together and the streams would appear brighter.

We note that there is a way to confirm the galactic origin of the Centaurus arc. By taking images along its length using different filters, (*e.g.* OIII or Hα) as discussed in Feldmeier *et al.* [50], one would expect to find an over abundance of planetary nebulæ at similar redshifts to NGC4709; thus confirming the stellar nature and formation mechanism.

The tidal tails of stellar debris follow the progenitor galaxies orbit through the cluster and stretch for several Mpc. The coherent length of structure in the diffuse light will

be much shorter than this since the real cluster potential is far from smooth. The other cluster galaxies will disrupt the tidal tails, "chopping" them into pieces. On average, each galaxy in a cluster experiences a close encounter with one of its massive cluster companions at a rate of one per Gyr, thus short sections of narrow features may survive for a crossing time. However, even deeper images of the feature may reveal the arc extending further from the cluster centre. Somewhere along the tidal tails lies the remnant spheroidal galaxy surrounded by a cloud of diffuse light that closely resembles the feature reported by Trentham & Mobasher [131].

The success of this model at reproducing a particular feature in the diffuse light within Centaurus has motivated us to continue to explore "galaxy harassment" as a mechanism for the origin of the intracluster light in general. We are currently in the process of devising a method for simulating the interaction of many halos within a cluster. One possibility is to repeat the simulations we have described in this chapter. This time, instead of evolving a single halo within the cluster, we would set of many models of compound galaxies to try and simulate the more complex interactions that galaxies undergo within their lifetime. This would allow us to better quantify the fate of the luminous matter that is stripped within a cluster.

Chapter 4 | *Dark matter detection*

The cold dark matter (CDM) theory has proved remarkably successful at predicting and explaining many well known observational results. At the moment the hierarchical CDM model is the most popular theory for explaining the formation of structure in the Universe. Nonetheless, the ultimate validation of CDM will be its detection, either directly in a laboratory, or indirectly through particle annihilation in the galactic halo. At the moment many experiments are taking place (or being constructed) that explore the possibility of CDM detection. We now turn our attention to this exciting subject.

We shall use a high resolution cosmological simulation of galactic mass halos that form in a Universe dominated by CDM. This is the first time that simulations of this kind are used to make predictions relevant to both of the detection scenarios. The results of chapter 2 are particularly important since we will be extrapolating the cosmological simulations to much smaller scales.

4.1 A cosmological simulation of the Local Group

One of the key aims of a cosmological simulation is to interpret and predict the dynamical properties of astrophysical objects such as clusters, groups and galaxies. Here we shall use one such simulation in which a pair of dark matter halos with similar dynamical properties to the Local Group, are followed throughout their evolution from a redshift of $z > 100$ to the present epoch (and beyond). The particle mass in the high resolution regions is $10^6 M_\odot$ and softening radius is set to 0.5 kpc. A thorough discussion and details of this simulation are presented in Ref. [96].

In Fig. 4.1* we can see different snapshots of the simulation. The grey scale shows the local density of dark matter at the indicated redshifts. At a redshift of z=0 we are able to identify two dark matter halos separated by 1 Mpc infalling at 100 kms^{-1} with peak circular velocities ≈ 200 kms^{-1}; this structure is what we identify as the "Local Group".

Now that we have a better understanding of the dynamical effects that act on ha-

*This figure kindly provided by Dr. B. Moore

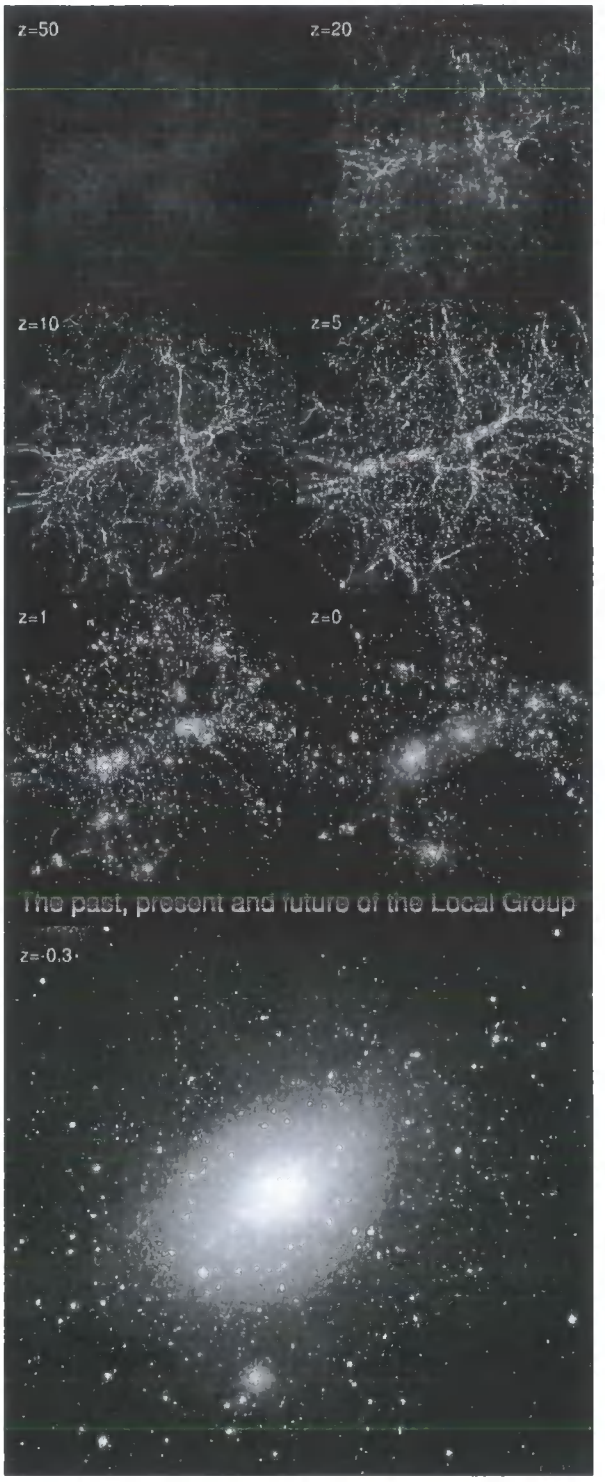

Figure 4.1: The hierarchical formation of a Local Group within a Universe dominated by CDM. The grey scale shows the local density of dark matter at the indicated redshifts. The upper six panels show a comoving volume of length 4 Mpc whilst the lower panel is the "future" halo resulting from a merger between the two halos surrounding M31 and the Galaxy.

los within halos we shall analyse substructure halos within the Local Group simulation investigating the evolution of their key properties.

The smallest scale on which there is evidence for dark matter is within dwarf spheroidal galaxies that orbit within the halo of the Milky Way. The Local Group simulation contains over 2000 of these systems with peak circular velocities, $v_{peak} > 10$ kms^{-1}. Most of these sub-halos orbit within the virial radius of the two large halos. Their internal structure is smooth because the resolution of this simulation does not allow us to resolve any substructure within them. A further high resolution re-simulation of one of these sub-halos was performed by Moore *et al.* [96], which revealed that substructure continues to form on even smaller scales giving rise to "halos within halos within halos" (because it resembles one of the dwarf spheroidal halos in our own Milky Way, with $\sigma_{1d} \sim 8$kms^{-1}, we shall call this sub-halo simulation "Draco").

4.1.1 The distribution of circular velocities in the Local Group

The first step in analysing the circular velocities of sub-halos is identifying each halo in the high density regions where they cluster. This is easy to do visually: the bound cores of the halos are evident when we look at density snapshots along its evolution (as can be seen in Fig. 4.1), but to characterise a sub-halo correctly we must only select the particles that are bound to it and screen out all background particles that may be streaming through. We shall use a group finding algorithm that uses local density maxima to find the halo centres and then iteratively checks for self-boundedness to define halo membership. The algorithm is named SKID and is fully described by Stadel *et al.* at the University Of Washington N-Body Shop[†].

The simulation outputs are a collection of particle masses, positions, velocities, potentials and smoothed density at discrete moments during its evolution at different redshifts, z. For the Local Group simulation the outputs range from z=50 to z=-0.3 (originally the simulation was run up to "the present day": z=0, but then it was allowed to evolve until the two biggest halos of the group coalesce into one single "super halo"). At each output we run the algorithm to find all of the bound halos and sub-halos and we use these to explore elements of the past, present and *future* of the Local Group.

For our implementation of SKID we explored different values of three parameters that control its behaviour: the linking length ℓ; which is the radius over which a particle and its nearest neighbour are associated, the minimum number of member particles n_{min} in the

[†]see `http://www-hpcc.astro.washington.edu/tools/tools.html`

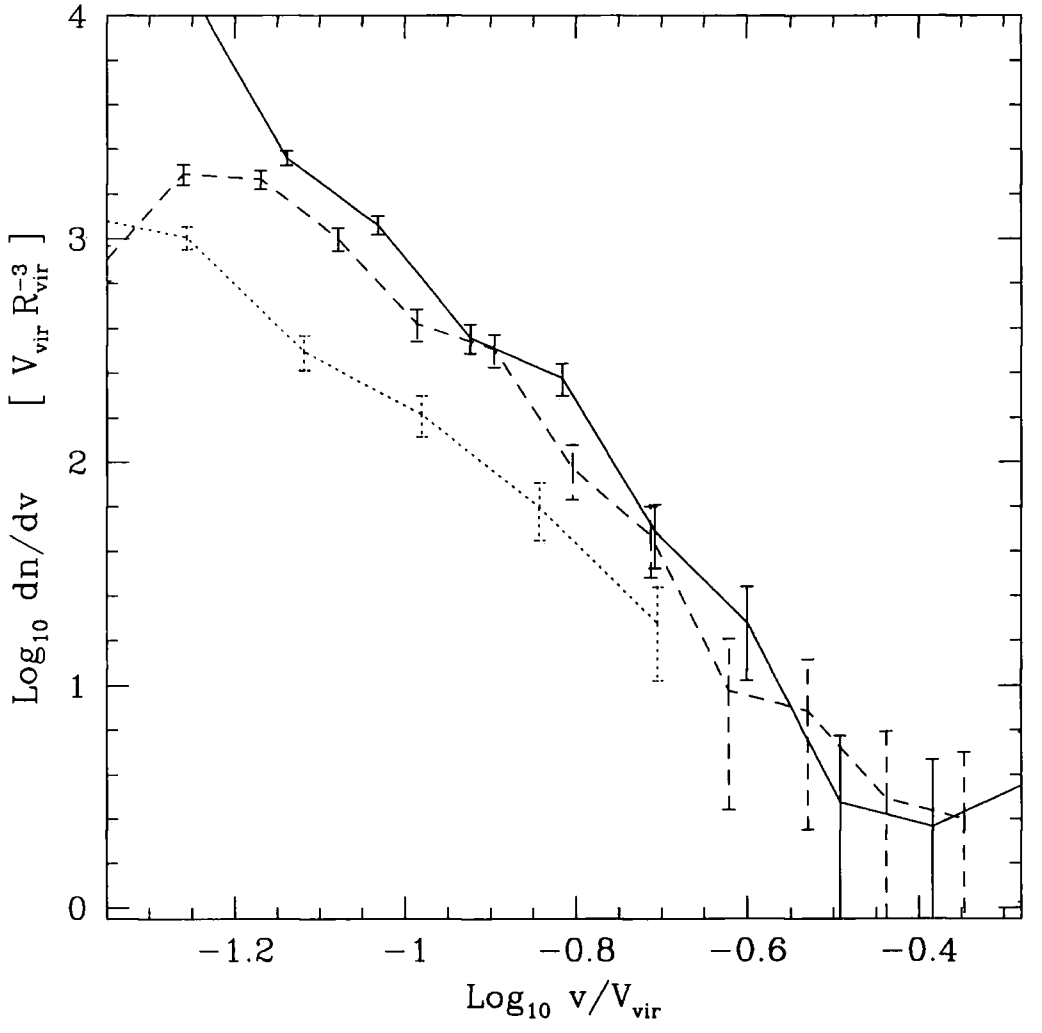

Figure 4.2: The differential velocity distribution functions for dark matter sub-halos within a CDM cluster (solid line), galaxy (dashed line) and mini-halo (dotted line). Each halo has been simulated with $\gtrsim 10^6$ particles and using softening lengths $\lesssim 0.002 R_{vir}$. The peak velocities of the sub-halos are normalised by the circular velocity at the virial radius of their parent halos.

group and the minimum over-density for dark matter particles which are considered for grouping den_{min}; although these parameters are not completely independent (*i.e.* fixing a minimum number of members automatically fixes the minimum mass of groups found, this in turn fixes the minimum density). We searched through many values for these parameters until we found a set after which further refinements did not modify the number and location of groups found: $\ell = 5\mathrm{kpc}$, $\mathrm{n}_{min} = 16$ and $\mathrm{den}_{min} = 100$ (this sets the lower mass limit for which we can resolve halos above a mass of $1.6 \times 10^7 \mathrm{M}_\odot$).

We define the velocity distribution function (VDF) as the number of halos per unit peak circular velocity interval (recall that $v_{peak} = \mathrm{MAX}[\sqrt{\mathrm{GM/r}}]$). The VDF of sub-halos within dwarf spheroidal, galactic and cluster mass CDM halos are compared in Fig. 4.2 (Here the "cluster" data is taken from Ghigna *et al.* [62] for a halo of mass $5 \times 10^{14}\mathrm{M}_\odot$). The masses of these objects vary by 7 orders of magnitude yet they all contain similar amounts of dark matter substructure. The slope of the circular velocity function within the draco, galaxy and and cluster halos are $\mathrm{n(v)} \propto v^{-\alpha}$ with $\alpha = 3.0, 3.7$ and 3.9 respectively. The slope of the VDF is shallower for the mini-halo than galactic or cluster halos which may reflect the fact that the simulations are approaching the "n=-3" part of the power spectrum, *i. e.* all halos are collapsing at the same time which may lead to a higher rate of merging.

4.1.2 Tracing the substructure of the Local Group

An interesting question that arises when dealing with the substructure of a simulation is: *How do the halos evolve once they enter the virial radius of the parent cluster?*

The first step in tracing the substructure of a simulation is identifying halos at each output of the simulation, after this, we need a rule for following a particular substructure clump as it evolves. Apart from outputting which of the particles belong in each group, SKID also calculates many physical quantities for each group such as the peak velocity of the halo, its total bound mass, the coordinates of its centre of mass, and the maximum radius.

Using the parameters discussed above for SKID we find that the earliest time in which we can find structure in the simulation is at the z=20 output. At this time ≈ 40 virialised halos are evident above the smooth background of particles. These halos are well defined and have peak velocities that mostly lie in the range $20\mathrm{kms}^{-1} < v_{peak} < 30\mathrm{kms}^{-1}$ (We show a histogram of their velocities in Fig. 4.3. The fact that few halos are found for $v_{peak} < 25\mathrm{kms}^{-1}$ is only a resolution effect, since with higher mass resolution we would

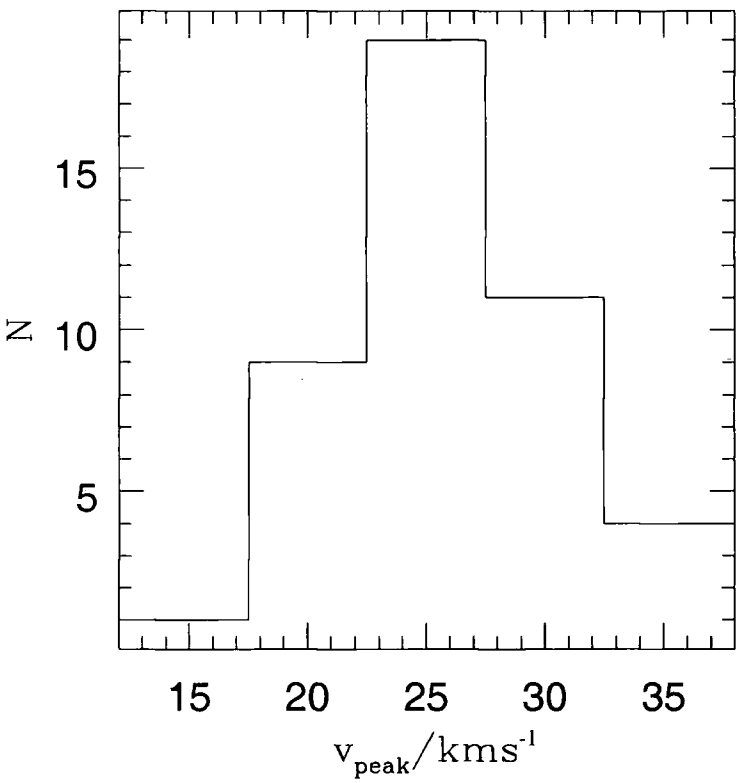

Figure 4.3: The peak circular velocities of halos found at z=20.

find many more halos of lower mass).

We can now trace these halos forward in time to see where they will end up by the end of the simulation. At each output available (z = 20.0, 15.0, 10.0, 7.0, 5.0, 3.0, 2.0, 1.5, 1.0, 0.75, 0.5, 0.3, 0.2, 0.0, 0.05, 0.02, -0.1, -0.2, -0.3) we run SKID again to identify the halos. The particles in each of the initial groups are tagged with a number. For each individual group we then search through the groups at the next redshift (in this case z=15) and look for the groups were the particles end up. We identify the halo that contains the majority of precursor particles and tag this group as the evolved version of the original at z=20. We do this for all halos at all redshifts until we end up with a list for each halo of the groups it has belonged to throughout the simulation. This allows us to construct a merger tree and to follow the changes in the peak circular velocity for each of the original halos at z=20.

The plot in Fig. 4.4 shows the evolution of the peak circular velocity v_{peak} for each of the "original" halos. We can see that all these halos end up within the large "super-halo"

by the end of the simulation. The merger history for all the groups can be seen in this plot; as the halos evolve, most begin to merge at z=10, some survive for a very long time, falling within the super-halo only at the very end of the simulation. This clearly illustrates that substructure is present in the simulation for a large percentage of its lifetime.

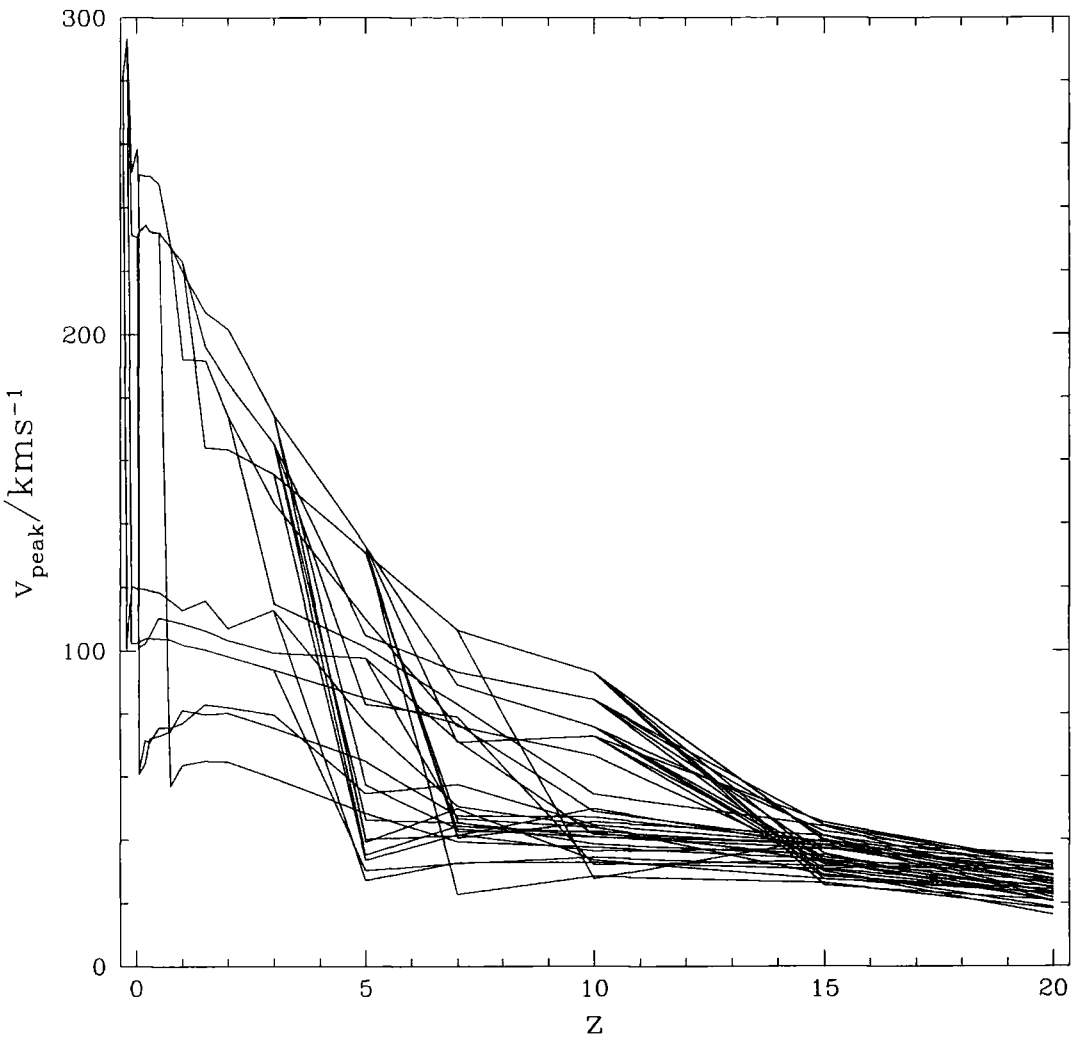

Figure 4.4: The evolution of v_{peak} for halos found at z=20. Each curve represents a different halo.

There is a problem in continuing to trace the halos in this fashion. After a halo falls into a bigger one we are left without any information as to its specific nature: *Is it now a sub-halo, orbiting intact within the virial radius of the parent or has it completely merged with the parent?* The answer to this question is not simple. For these few halos we could trace the structure individually and examine what their ultimate fate is. This procedure

would be difficult to manage for the whole of the simulation due to the great number of halos present.

An easier approach is to use the same software and identify all halos within the virial radius of the super-halo at the final redshift and trace these *backwards*. This will allow us to follow all of the substructure which is present at the end and to study the evolution of their properties.

We proceed in a similar way as before, but now we set an initial list of halos to those found at the end of the simulation. Again we follow the particles for each halo, taking each time as its "progenitor" that halo which contains the most particles of its "sibling". This allows us to trace the evolution of v_{peak} as a function of redshift for each sub-halo. In Fig. 4.5 we attempt to plot this function for all of the halos that are within the virial radius of the "super-halo" at z=-0.3. Because there are thousands of halos this makes the plot look very crowded, particularly at low redshift.

Comparing Fig. 4.4 with Fig. 4.5 we can see that the new procedure clearly traces some of the structures back to the very beginning of the simulation. Other halos disappear from the merger tree because we reach the redshift at which they form. Thus we are seeing direct evidence that most of the substructure halos present at z=-0.3 have been orbiting within our simulated cluster from beyond a redshift of z=7.0. Substructure halos survive for long times within their parent halos.

It is apparent from the plots in Fig. 4.5 that most of the substructure halos with $v_{peak} < 40\text{kms}^{-1}$ present little or no evolution of their peak velocity. To quantify the amount of evolution in this quantity we calculate the time that corresponds to each redshift by integrating the relation between cosmic time and redshift. This gives for a standard CDM Universe:

$$t = \frac{2}{3H_0} \times (1+z)^{-3/2} \tag{4.1}$$

(here H_0 is the present day *Hubble parameter* and is taken to be 100h $\text{kms}^{-1}\text{Mpc}^{-1}$[‡]). We then fit each v_{peak} *vs* time curve to a straight line. The slope of these fits gives us the rate of change in peak velocity as the halos evolve within the simulation. Next, to quantify the evolution we bin the data and draw a histogram of the number of halos per interval of velocity change.

From Fig. 4.6 we can clearly see that almost 75% of the halos change their peak

[‡]Here h is taken to have the same value as was used for the simulations h $\approx$ 0.5

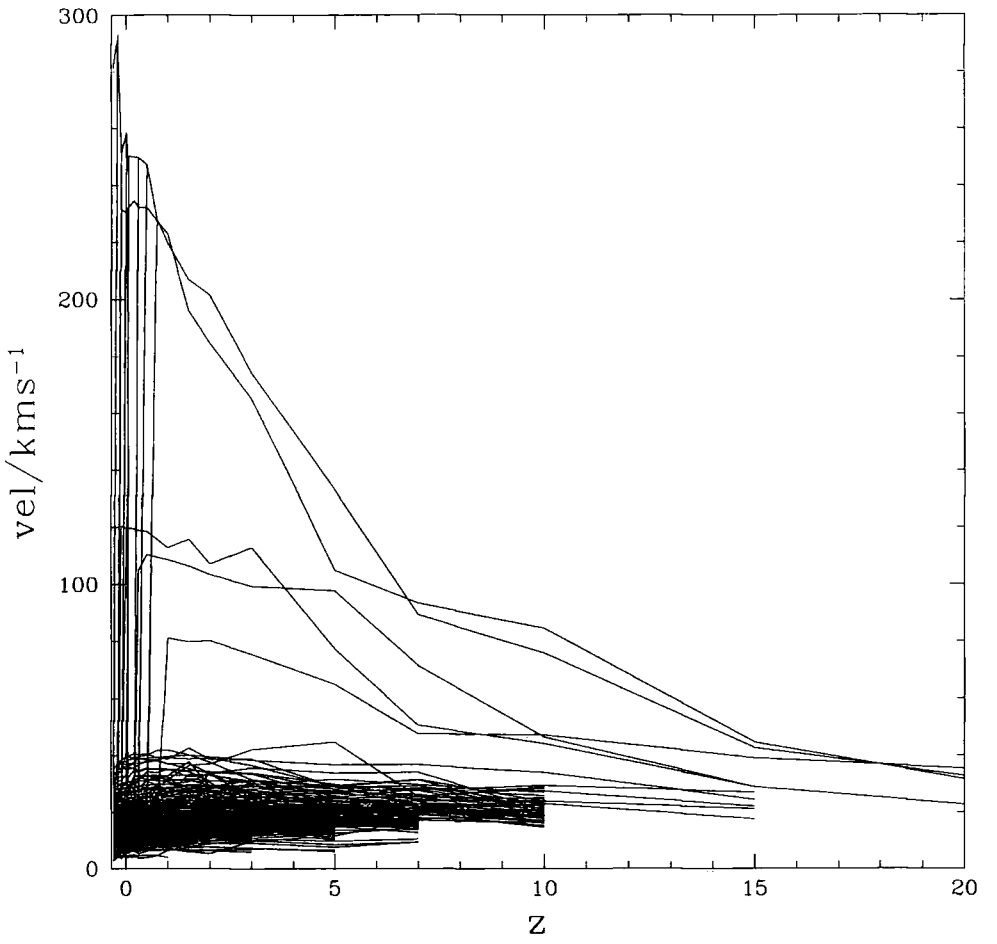

Figure 4.5: The evolution of v_{peak} for halos found at z=-0.3. Each curve represents a different halo. We plot all halos from z=-0.3 to z=20.0.

velocities by less than $0.5h^{-1}kms^{-1}Gyr^{-1}$. Even though they spend more than 5Gyr orbiting within a more massive virialised system. This adds further strenght for our use of v_{peak} as a label to characterise substructure halos.

4.2 Indirect detection

Both theory and observational data currently favour a Universe with a matter density that is dominated by non-baryonic particles. Many candidates have been proposed: some are known to exist, others are more speculative (*e.g.* , Ellis [47] and references therein). Structure formation in a Universe dominated by cold dark matter (CDM) has been extensively tested against observations and the model has proven highly successful at reproducing the large scale properties and distributions of galaxies [36, 10]. On the non-linear scales

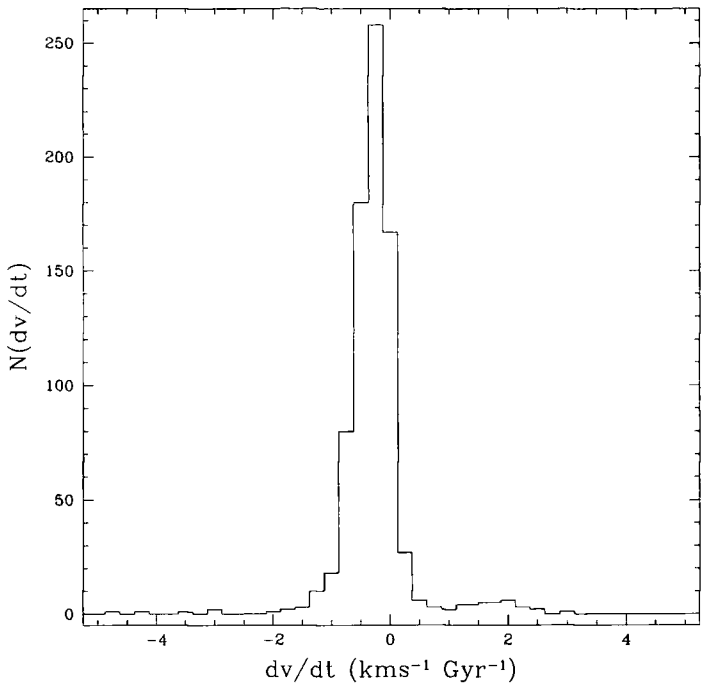

Figure 4.6: A histogram of the change in v_{peak} as a function of time.

of galactic halos it remains to be confirmed whether or not the model can successfully reproduce the observational data [94, 52, 25, 97, 79, 120]

Direct detection in the laboratory is the ultimate technique for verifying the existence of dark matter particles (see Collar [32]). However, even the most popular candidate for dark matter, the neutralino, has a cross section that spans many orders of magnitude and the current laboratory searches are only just becoming sensitive to the cosmologically interesting parameter range. Presently, astronomical observations provide the best insights into the nature of the dark matter; furthermore direct detection relies on the existence of a smooth component of dark matter.

Within the next few years indirect detection of neutralinos will provide interesting constraints on their possible cross-section and masses. Neutralino-neutralino annihilation produces observable photons (as well as a host of other particles) that may be observed as a diffuse gamma-ray background from the halo surrounding the Milky Way as discussed in Refs. [66, 126, 123, 134, 122, 22, 82], and more recently, in Refs. [15, 17, 6, 63, 5].

High energy γ-ray experiments can be broadly classified into two groups: satellite born spark chamber detectors, such as the Energetic Gamma–Ray Experiment Telescope (EGRET) [76] or the Gamma–Ray Large Area Space Telescope (GLAST) [58] and atmospheric Cherenkov telescopes (ACTs) such as the Very Energetic Radiation Imaging

	EGRET	GLAST	VERITAS
Effective Area (cm^2)	1500	8000	7×10^8
Energy Resolution	10%–15%	10%	15%
Angular Resolution	5.8^o (at 100MeV)	3.0^o (at 100MeV)	1.0^0
Energy Range	20MeV– 30GeV	20MeV– 300GeV	50GeV–50TeV
Field of View (sr)	0.5	> 2	0.004

Table 4.1: Approximate characteristics of γ-ray detection instruments.

Telescope Array System (VERITAS) [85]. Ground based and satellite experiments offer two complementary ways of detecting gamma rays. While satellite experiments offer a lower energy threshold, superior energy resolution, and the possibility of relatively long exposure times, their relatively small effective area (approximately 1 m^2) limits their sensitivity at high energies. On the other hand ACTs offer the potential for very large effective areas (approximately 0.3 km^2), but a higher energy threshold ($E_\gamma < 250GeV$).

The primary process for detection in satellite experiments is the conversion of γ-ray photons into electron-positron pairs. The radiation of interest is first separated from other forms of cosmic radiation and then the pair creation process takes place within a spark chamber. The tracks of the pair particles are then followed electronically and used to determine the direction of incidence of the primary high-energy photon. ACTs employ large (approximately 10 m) optical reflectors to image flashes of Cherenkov light from electromagnetic showers formed as high-energy γ-rays interact with the earths atmosphere. By making use of the distinctive differences in shower images, γ-ray signals may be distinguished from hadronic showers which form an important part of the radiation detected in these instruments. We present the approximate characteristics for the three experiments mentiones above in Table 4.1.

Renewed interest in these predictions has recently arisen because of an unexplained component of diffuse high energy photons in the EGRET data (*e.g.* [42]), and also the possibility of an excess from the center of the Galaxy itself [88], unexpected clumpy emission and the unresolved "discrete sources" [67]. Progress in this area will result from several new and sensitive gamma-ray surveys such as GLAST and VERITAS. The sensitivity and resolution range of these new instruments will be important factors in distinguishing gamma ray signals coming from particle annihilation from those that arise due to other high energy astrophysical phenomena (such as γ-ray pulsars, active galactic

nuclei, γ-ray bursts and the diffuse emission that comes from the Milky Way).

The efficiency of the annihilation process is strongly dependent on the local density and the cross-section of the neutralino. Many authors have calculated the expected flux from the Galactic halo using simple models for the expected mass distribution of neutralinos within the Galaxy (see, *e.g.* , Refs. [17, 63]) or from its satellites [82, 5].

Advances in computational Cosmology have lead to several recent breakthroughs that have direct relevance to the detection of dark matter. In particular, the numerical resolution that can be achieved using parallel computational techniques is now sufficient to study the internal structure of dark matter halos that form within a cosmological context. The results of these simulations have important implications for indirect (and direct) detection of dark matter candidates. Most significantly for particle-particle annihilation, we are now confident that the central density profile of CDM halos follows a singular power law down to small scales [30, 103, 98, 61]. Thus we may expect a point like source of mono-chromatic gamma-rays emanating from the center of the Milky Way, where the annihilation rate will be very high.

A second fundamental prediction of the CDM model is that previous generations of the merging hierarchy survive within halos [61]. We have demonstrated that halos which accrete into larger systems may be tidally stripped of most of their mass, however their dense central cores survive and continue to orbit within the parent halos. This may present some problems for the CDM model since the predicted number of satellites within the Milky Way's halo is 50–100 times as many as observed [97]. If the CDM model is correct, then only a fraction of these satellites must have formed stars and most of the substructure remains as dark objects within the Galactic halo.

The possibility of an enhanced gamma-ray background from dark matter substructure was explored by Bergström *et al.* [16], who made simple assumptions as to the mean density and abundance of such clumps. We can now use the high resolution N-body simulations to directly measure these quantities. The simulations also allow us to study the influence of the halo shapes on the diffuse gamma-ray background and the intensity of the central halo emission that arises from the singular dark matter density profiles.

4.2.1 The sky distribution of the gamma-ray background

In what follows we will consider a flux of photons (or other particles) that are a by-product of the annihilation of dark matter particles within the smooth component of dark matter that surrounds the Galaxy. It is not our intention to discuss the details

of neutralino interactions, a complete overview on these processes (and super-symmetric matter in general) can be found in Refs. [74, 14]

4.2.1.1 Model neutralino halos

We calculate the gamma-ray flux along a given line of sight through a spherically symmetric galactic halo using:

$$\phi(\psi) = \frac{K}{4\pi} \int_{Line\ of\ sight} \rho^2(l) dl(\psi) \tag{4.2}$$

where ψ is the angle between the direction of galactic center and observation; ρ, the density of dark matter at distance l from the observer. We have summed up the dependence of the flux on neutralino mass and interaction cross section in the constant K. This is enough scope for the present discussion - it is straightforward to take our results and input a neutralino cross-section, $< \sigma v >$, and mass, M_χ to determine the absolute gamma-ray flux (where K is defined to be $< \sigma v > /M_\chi^2$). Our results can also be used to infer the sky distribution of other products of the annihilation, such as neutrinos or positrons.

The line of sight distance, l, is related to the radial distance from the halo center, r, via

$$r^2 = l^2 + R_o^2 - 2lR_o \cos(\psi)$$

where R_o is our galacto-centric distance, taken here to have the IAU standard value of $R_o = 8.5$kpc [77], and ψ is related to galactic coordinates (ℓ, b) through

$$\cos(\psi) = \cos(\ell)\cos(b).$$

For the halo density profile, $\rho(r)$, we take the latest results from the highest resolution numerical simulations of galactic halos carried out to-date [97] These authors simulated 6 different galactic mass halos with force resolution of 0.5 kpc and mass resolution of $10^6 M_\odot$. (Throughout the chapter we will use the Hubble constant value of $H_o = 100\mathrm{hkms}^{-1}\mathrm{Mpc}^{-1}$ and h = 0.5; as was done for the simulations.) The best fitting density profile to these data is (subscript *moore*):

$$\rho_{moore}(r) = \frac{\rho'_{moore}}{(r/a)^{1.5}(1+(r/a)^{1.5})}. \tag{4.3}$$

Where r is the distance from the halo center, $a = r_{200}/c_{moore}$ the scale radius for halos of mass $\approx 1 \times 10^{12} M_\odot$. The virial radius of our fiducial Galactic halo, $r_{200} \approx 300$ kpc, is defined as the radius of a sphere at which the mean over-density is 200 times the

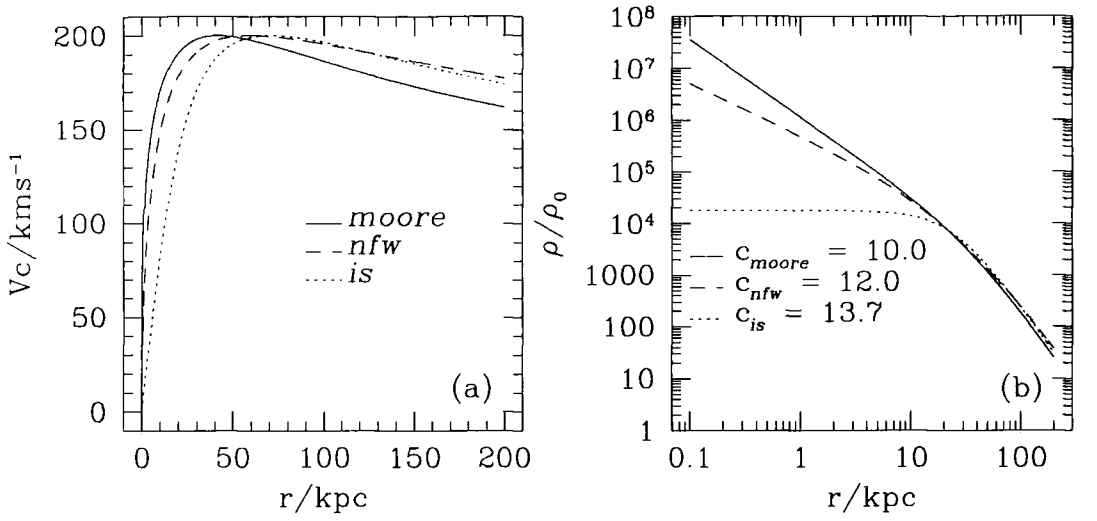

Figure 4.7: The circular velocity curves $v_c(r) = \sqrt{GM(r)/r}$ (a) and density profiles (b) are plotted as a function of the radius for each of the halo models considered in the text.

cosmological mean density. (A central density profile of slope -1.5 on galactic scales was also found by Jing & Suto [73] and confirmed as an asymptotic slope by Ghigna *et al.* [62].)

We also compare this profile with that determined by Navarro *et al.* [103] using a sequence of lower resolution studies (subscript *nfw*) (the main difference being that the central dark matter density profile has a slope of -1):

$$\rho_{nfw}(r) = \frac{\rho'_{nfw}}{(r/a)(1+r/a)^2} \tag{4.4}$$

and the modified isothermal profile with a constant density core (subscript *is*):

$$\rho_{is}(r) = \frac{\rho'_{is}}{[1+(r/a)^2]^{3/2}}. \tag{4.5}$$

The scale radius, a, is determined directly from the numerical simulations, except for the modified isothermal model which we normalise to match the observational rotation curve data (as in Ref. [80]); $a_{is} = 24.3$ kpc, $a_{nfw} = 27.7$ kpc and $a_{moore} = 33.2$ kpc (this radius is directly related to the concentration parameter, $c = r_{200}/a$). We normalise each density profile such that the peak circular velocity, $v_{peak} = 200$ km/s (the maximum of the $v_c = \sqrt{GM/r}$ curve), which gives: $\rho'_{is} = 4.96 \times 10^6 M_\odot$ kpc^{-3}, $\rho'_{nfw} = 5.11 \times 10^6 M_\odot$ kpc^{-3} and $\rho'_{moore} = 1.64 \times 10^6 M_\odot$ kpc^{-3}. We plot the effective circular velocity profiles and density profiles of these model halos in Fig. 4.7(a) and Fig. 4.7(b) respectively.

In Fig. 4.8 we plot the flux, ϕ, along the line of sight through a spherical Milky Way halo using the above density profiles as the observer looks towards the Galactic center at

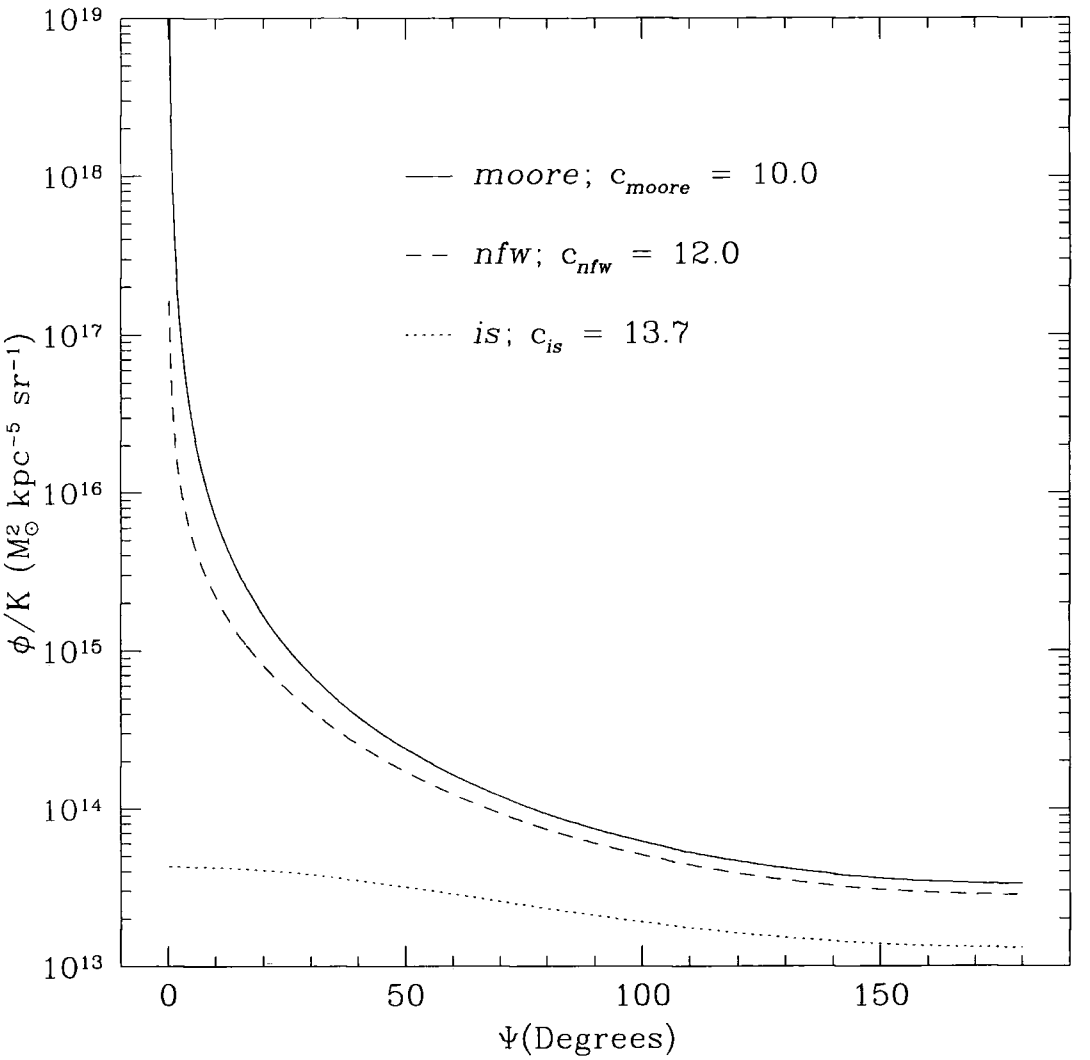

Figure 4.8: The gamma ray flux from neutralino annihilation, $\phi(\psi)$, plotted as a function of the angular distance from the galactic center ψ. The curves show the results using the three different density profiles plotted in Fig. 4.7 The flux at a given position is averaged over 4π steradians.

$\psi = 0°$, to the Galactic anti-centre at $\psi = 180°$. As expected, the central annihilation flux depends strongly on the form of the inner density profile. At an angle of five degrees from the Galactic center, the ratio of fluxes from the three different profiles, *moore:nfw:is* are 1000:100:1.

The peak central value depends upon the distance from the Galactic center that we are willing to consider integrating from – the flux slowly diverges for the density profile in Eq. (4.3). However, within a given radius, most of the neutralinos would have self annihilated leaving a tiny constant density core. We can estimate the size of this core using $(n\sigma v)^{-1} = t_h$, where $t_h \sim 10$ Gyrs is the Hubble time. Taking a typical cross section, $\sigma v = 10^{-30}\mathrm{cm}^3\ \mathrm{s}^{-1}$, and adopting the Moore *et al.* density profile we find that the annihilation radius within the Milky Way is approximately 4×10^{-7} parsecs $\approx 10^{-12} r_{200}$.

The total flux that arises within 5 degrees of the Galactic center using the Moore *et al.* density profile is a factor of 10 larger than that found using the NFW profile (both integrated down to the annihilation radius calculated above).

4.2.1.2 Comparison with high resolution CDM simulations

We can use the numerical simulations to compare directly with the above predictions that were obtained assuming spherical symmetry. (For details of the numerical simulations see Moore *et al.* [97]). To construct the expected gamma-ray sky maps we choose a simulated dark matter halo at a redshift z=0 that has a peak circular velocity of $\sim 200\mathrm{kms}^{-1}$ and a total mass, within the virial radius, $r_{200} = 300\mathrm{kpc}$, of $1 \times 10^{12}\mathrm{M}_\odot$. This simulated halo is from the "Local Group" simulation discussed earlier and is close to our fiducial Milky Way cold dark matter halo that we adopted in the previous section.

N-body simulations attempt to simulate a collisionless fluid of dark matter using discrete massive particles. We calculate the local density at the position of each particle by averaging over its nearest 64 neighbours. The observer is placed 8.5 kpc from the halo center (defined using the most bound particle in the simulation) and we sum up the flux of annihilation products along each line of sight using the discrete equivalent to Eq. (4.2):

$$\Phi(\ell, b) = \frac{K}{\Omega} \sum_{LOS} \rho_i^2(\ell, b) \Delta r_i(\ell, b) \tag{4.6}$$

where ℓ, b are galactic longitude and latitude respectively. The flux is binned in angular windows of size $\Omega = 1° \times 1°$ and in the radial direction in fixed increments $\Delta r_i = 1\mathrm{kpc}$.

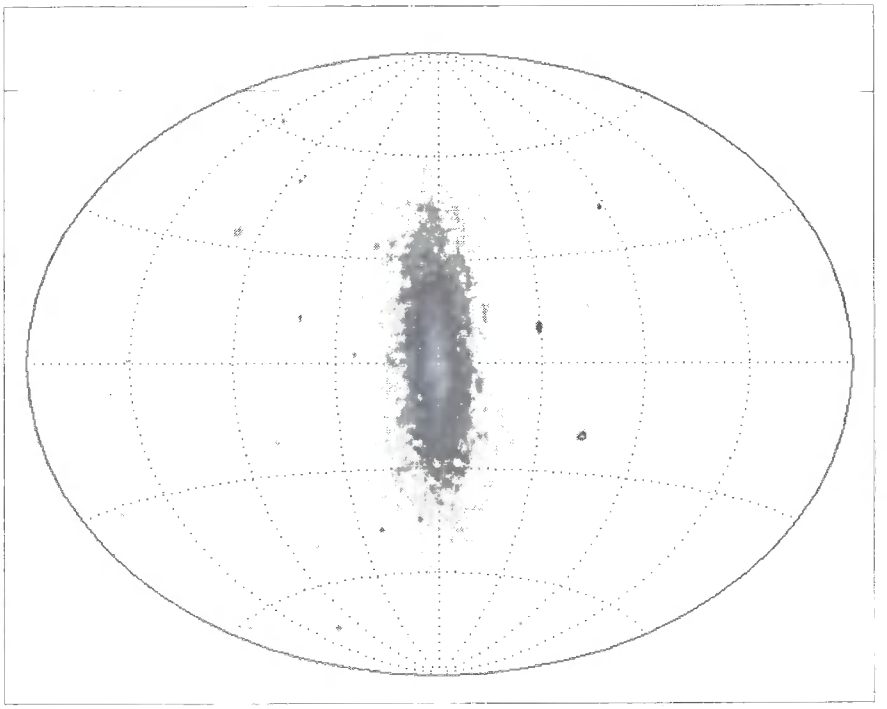

(a)

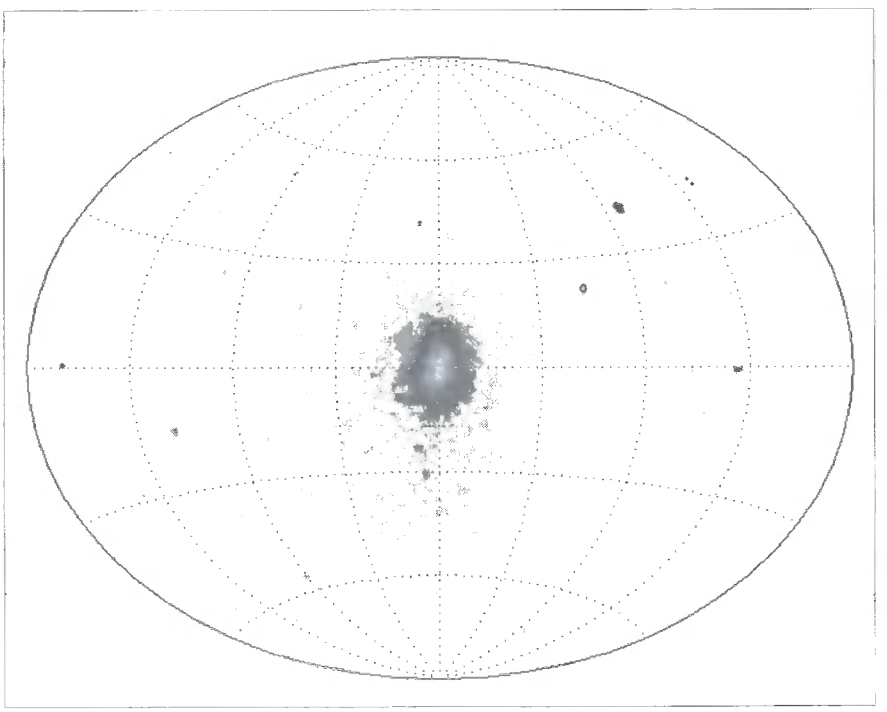

(b)

Figure 4.9: All-sky maps of the gamma ray background constructed using a single high-resolution N-body simulation of a cold dark matter halo. The observer has been placed in the short (a) and long (b) axis of the simulated halo.

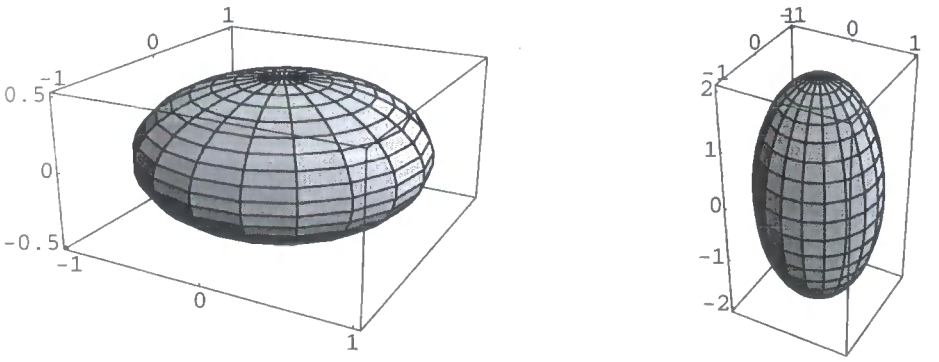

Figure 4.10: The left panel shows a unit oblate ellipsoid and the right hand panel shows a unit prolate ellipsoid. The axis ratios for both are 2:1.

The simulated dark matter halos are typically flattened oblate or prolate systems [7] We do not know a-priori in which axis the stellar disk would be located, therefore we show two all-sky maps using the same dark matter halo but viewed using two different locations for the "observer": Figure 4.9(a) and Fig. 4.9(b) has the observer located on the short and long axes respectively. Both of these plots show the enhanced brightening towards the halo center, as well as some clumpy substructure in the halo itself. Note that both the central halo and the centers of the substructure halos are artificially "dimmed" in these plots due to the numerical resolution ~ 0.5 kpc, which sets a maximum density that can be resolved. The non-spherical shape of the halo is also clearly evident by inspecting the plots with different observer positions.

Recent estimates for the shape of the Milky Way's halo (see, *e.g.* , Ref. [106] and references therein), suggest that it may be flattened with a short/long axis ratio of 0.5. An independent constraint from the orbit of the Sagittarius debris stars yields a nearly spherical dark matter halo [72]. The simulated halo that we have chosen to analyse represents a typical prolate CDM halo with a short to long axis ratio of 0.4, and intermediate to long axis ratio of 0.5.

It is straightforward to estimate the effects of flattened dark matter halos by modifying Eq. (4.2) to accommodate triaxial shaped bodies. The simplest way to achieve this is to change from spherical coordinate r to

$$\xi^2 = \frac{x^2+y^2}{b^2} + \frac{z^2}{c^2}$$

where $b > c$ for the oblate case, and $b < c$ for prolate and we leave z as the axis of symmetry. A 2d visualization of these 3d shapes is illustrated in Fig. 4.10.

In Fig. 4.11 we plot spherical, oblate (2:1) and prolate (2:1) versions of the integral

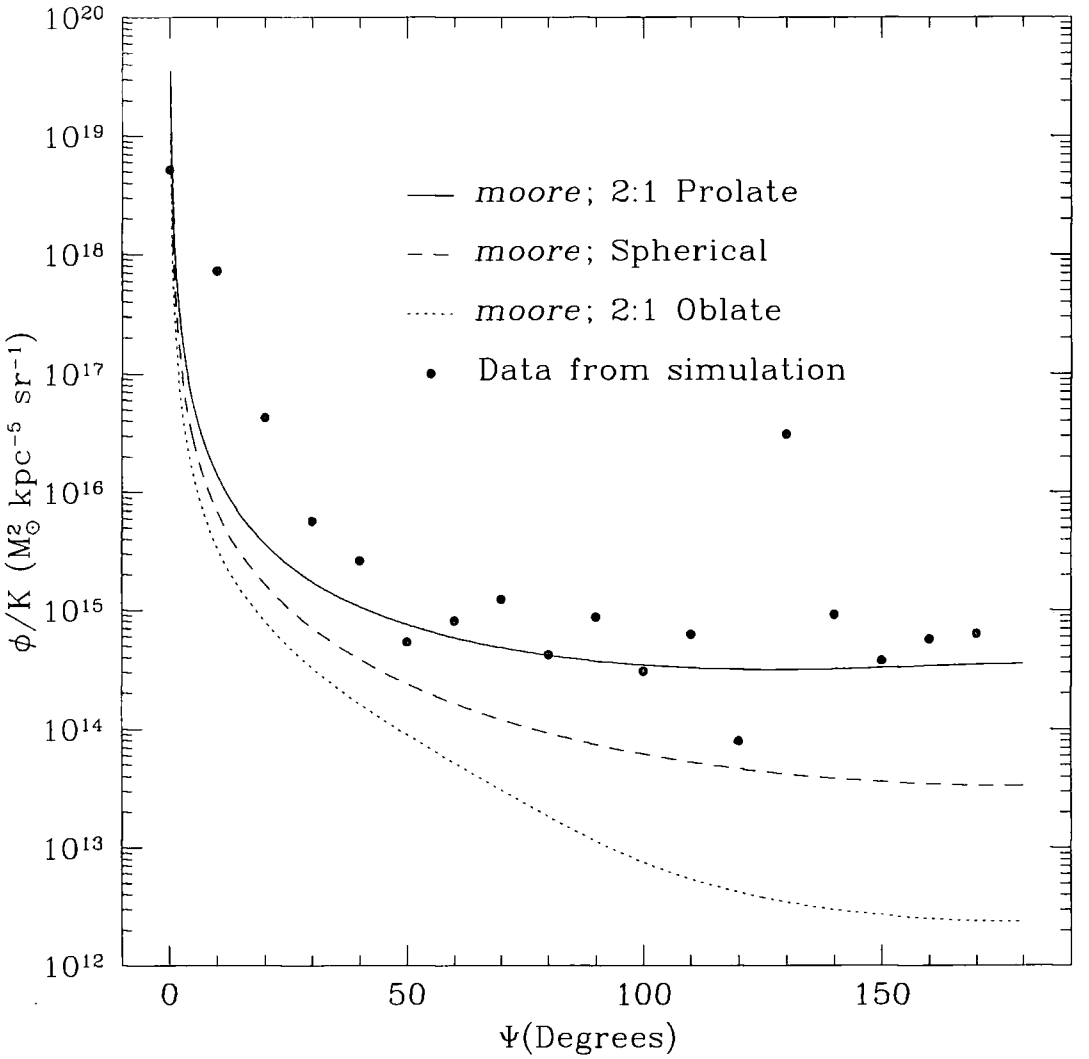

Figure 4.11: The gamma ray flux, ϕ, plotted as a function of angle ψ, for smooth halos of the same total mass using the density profile given in Eq. (4.3) for spherical, oblate and prolate halo geometries. The points are values of the flux measured directly from the N-body halo used in Fig. 4.9.

in Eq. (4.2) using the Moore *et al.* density profile. The observer is located on a plane parallel to the axis of symmetry, again at a distance $R_o = 8.5$kpc from the center of the halo. The halo shape leads to little difference towards the Galactic center, but at the anti-center prolate halos can be 100 times brighter than oblate halos.

We can also compare the predicted angular flux with that measured directly from the N-body simulation. The annihilation flux is averaged in ten degree bins from the simulated dark matter halo, along a great circle from the galactic center to its anti-center. This direct measurement of the flux is also plotted (as points) in Fig. 4.11. These data are particularly noisy due to the large numbers of substructure clumps in the simulation - the spike at $\psi = 125°$ is due to a massive dark clump that happens to lie exactly along this chosen line of sight.

4.2.2 Substructure

4.2.2.1 Enhancement of global flux due to substructure

Cold dark matter substructure clumps have singular density profiles that will be a significant source of annihilation products. The velocities and spatial distribution of dark matter substructure is unbiased with respect to the smooth dark matter background [62]. Therefore, to first order, it increases the global sky brightness in any given direction. However, the details depend on how much substructure survives within the solar radius and also on how far down the mass function substructure halos form and survive.

First we will estimate the annihilation flux from clumps of dark matter that are known to exist in the Galactic halo *i.e.* the dark matter halos that surround the Magellanic Clouds and dwarf spheroidal galaxies. In fact, high-Energy gamma-ray emission from the Large Magellanic Cloud (LMC) was detected with EGRET by Sreekumar *et al.* [125] in 1992 (although the origin of this emission was reported to be the interaction of cosmic rays with interstellar matter).

We estimate the average flux, Φ_{AV}, from the dark matter halos that surround some of the principal structures in the Local Group: The "Andromeda Galaxy"; M31 ($v_{peak} = 200\text{kms}^{-1}$ at a distance of 700 kpc), The Large and Small Magellanic Clouds ($v_{peak} = 70\text{kms}^{-1}$ and $v_{peak} = 40\text{kms}^{-1}$, respectively; both at a distance of 50 kpc), Draco ($v_{peak} = 10\text{kms}^{-1}$ at a distance of 50 kpc) and a small dark matter clump ($v_{peak} = 2\text{kms}^{-1}$ at a distance of 10 kpc). A sketch of the geometry is given in Fig. 4.12.

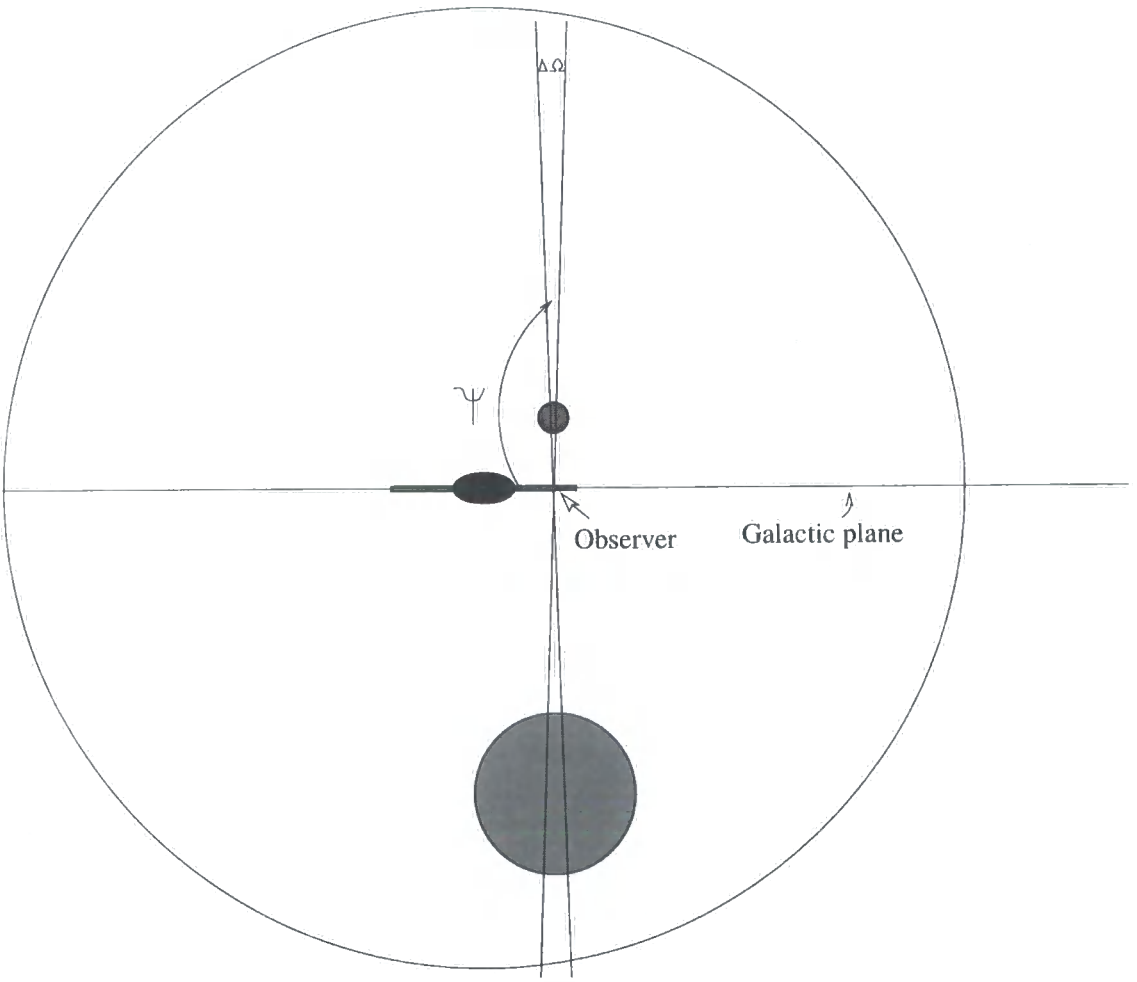

Figure 4.12: A sketch showing the geometry of an observer in the galaxy viewing substructure in the galactic halo.

The total flux from a substructure halo at distance R_c from the observer is

$$\Phi_{TOT}(R_c) = \frac{K}{R_c^2} \int \rho^2(r) r^2 dr. \tag{4.7}$$

by considering the central $\Delta\Omega = 1^\circ \times 1^\circ$ patch over each clump, we define the maximum integration limit in 4.7 above and the average flux is then

$$\Phi_{AV} = \frac{\Phi_{TOT}}{\Delta\Omega} \tag{4.8}$$

(we set $\Delta\Omega$ in steradians, so we may compare directly with the smooth flux of Section 4.2.1).

For the dark matter distribution within the substructure clumps we use the Moore *et al.* profile, which provides a good fit to the smallest, well-resolved substructure halos. The concentration of all dark matter halos is, in general, a function of mass [78]. For the CDM model and this profile:

$$c_{moore} \approx 102 \left(\frac{M_{vir}}{1h^{-1}M_\odot}\right)^{-0.084}. \tag{4.9}$$

This defines the scale radius of each substructure clump: $a_{\rm M31} = 33.3$kpc, $a_{\rm LMC} = 6.7$kpc, $a_{\rm SMC} = 3.1$kpc, $a_{\rm Draco} = 0.5$kpc, $a_{\rm Tiny} = 0.05$kpc.

The integral in Eq. (4.7) diverges as $r \to 0$ for the density profile that we are using, however, even the smallest substructure halos will have a maximum density set by the radius within which most of the neutralinos would have self annihilated. We therefore present results for the average flux from these clumps as a function of the minimum integration radius $\rm R_{min}/a$ in Fig. 4.13, where a is the scale radius as defined above.

For comparison, we plot the range of background emission at the Galactic anti-center as the shaded line in Fig. 4.13. The Tiny clump is only marginally visible above the background flux (depending on whether or not the Galactic halo is prolate or oblate) whereas the rest of the substructure is easily visible. Also for comparison, we have plotted the flux from the inner region of the galaxy which is clearly the brightest of the these sources.

Although the Galactic halo is expected to contain only about a dozen clumps more massive that the Magellanic Clouds, there are many thousands of smaller mass objects. The mass function of substructure is a power law close to $dn(m)/dm \propto m^{-1.9}$ or in terms of circular velocity $dn(v_c)/dv_c \propto v_c^{-3.8}$ [62]. Above a circular velocity $v_{peak} = 10$ km s^{-1} and 1 km s^{-1} we expect the galactic halo to host roughly 1000 and 5×10^5 substructure halos respectively. Future simulations should be able to measure how far

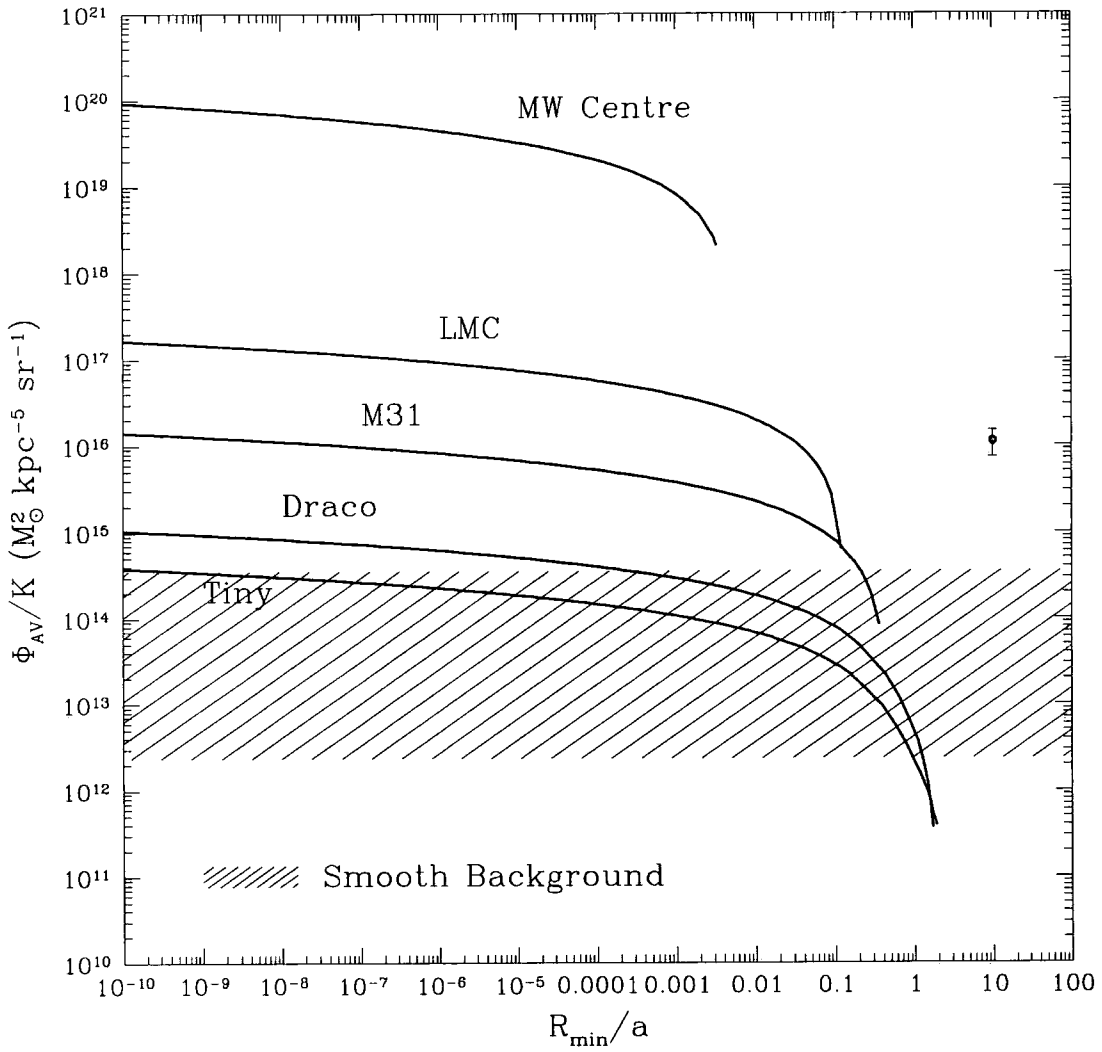

Figure 4.13: The gamma ray flux, Φ_{AV}, plotted as a function of minimum integration radius R_{min} for halo substructure of different circular velocities and distances as detailed in the text. The shaded region shows the range of background values at the Galactic anti-center that can be expected depending on the halo shape. The point is the average flux due to all clumps with $v_{peak} > 1$ km s^{-1}.

down the mass function substructure halos can survive as well as to determine their central density profiles. (We note that the highest resolution simulation to date resolved the substructure within the "Draco" dark matter mini-halo of mass $10^7 M_\odot$ discussed in section 4.1. The force resolution was 10 parsecs and the mass resolution was $10M_\odot$ allowing substructure with peak circular velocities as low as a few hundred meters per second to be resolved. The survival of substructure continues even down to this scale, where the slope of the power spectrum is close to -3.)

We calculate the total flux from substructure using Monte-Carlo techniques. First we generate a list of peak circular velocities and positions of 5×10^5 substructure halos in the range of 1–70km s^{-1}. (Distances are randomly selected using the Moore *et al.* density profile and peak circular velocities are randomly assigned from a power law distribution scaling as $v^{-3.8}$). For each lump, we estimate its total flux as in the previous cases, integrating Eq. (4.7) with a density profile scaled according to Eq. (4.9) for the concentration.

In the absence of further constraints on the possible value for R_{min}, we use the same criteria as before and choose it to be a fixed fraction of the virial radius, $R_{min} \approx 10^{-12} r_{200}$. This corresponds to a mean density of $\approx 10^{22} M_\odot$ kpc^{-3} for the galactic halo. The effects of altering the minimum integration radius is apparent from inspection of Fig. 4.13. The total flux is then averaged over the entire sky and we repeat this process in order to estimate the variance. The cumulative distribution of flux above a given substructure peak circular velocity ($\Sigma\Phi_{TOT}$) is plotted for ten of these random halo realisations in Fig. 4.14.

It is evident from this plot that the effects of including the entire mass spectrum of substructure is quite dramatic and boosts the expected flux from the smooth halo by several orders of magnitude.

To quantify the brightening of the background due to substructure, we have calculated the average flux due to all clumps with $v_{peak} > 1$ km s^{-1}. The point plotted in Fig. 4.13 represents this contribution to the flux, where the error-bar is the 1σ variation among the different Monte-Carlo models. From this plot we see that the flux due to substructure can be as much as 4 magnitudes brighter than the background. We note that one needs to observe several square degrees on the sky to ensure a significant number of clumps lie in the field of view. (Also note that the variance at high peak circular velocities is due to the proximity of the largest few dark matter substructures, however, the mean total flux converges to similar values for each Monte-Carlo model.)

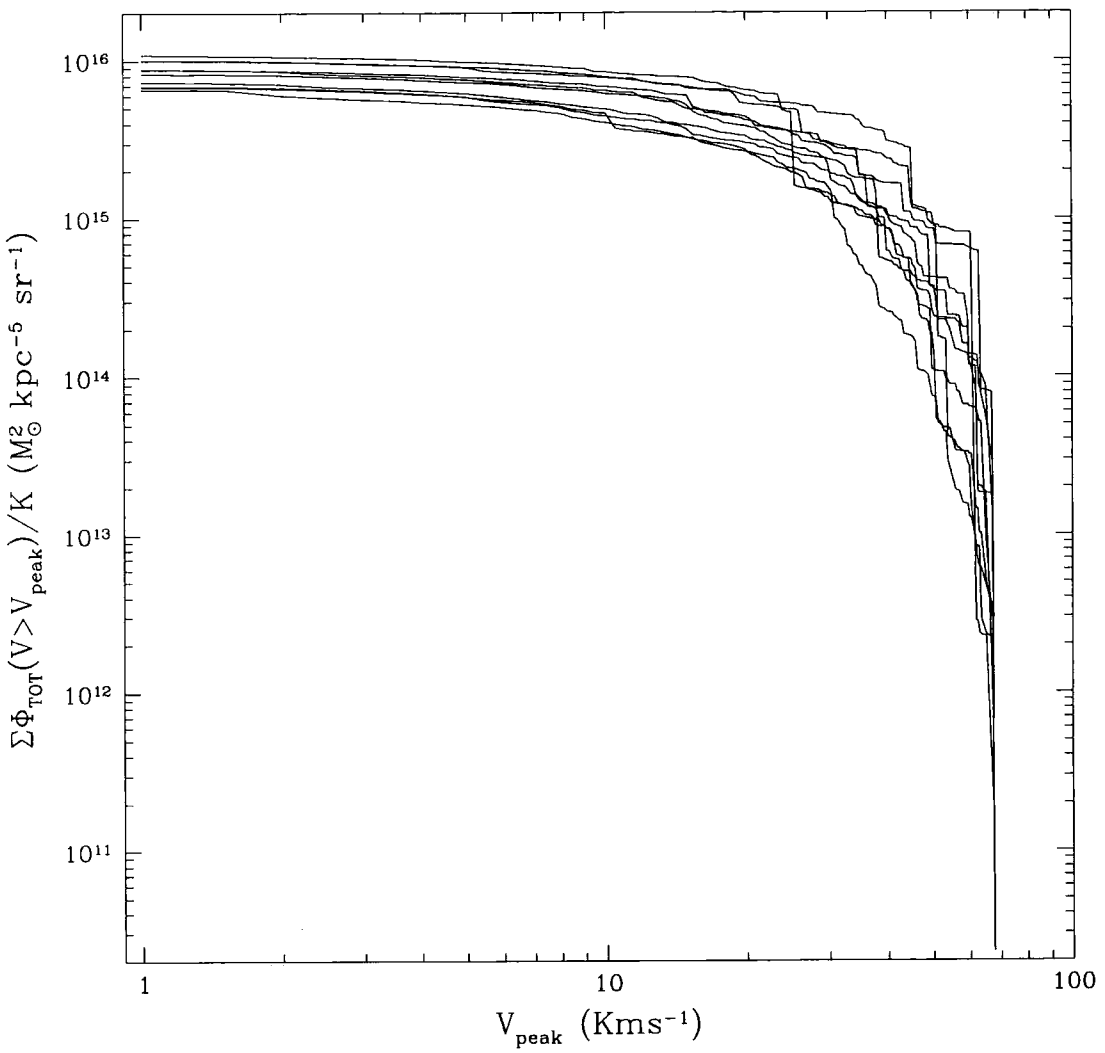

Figure 4.14: The cumulative gamma-ray flux from halo substructures, $\Sigma\phi_{TOT}(v > v_{peak})$, above a given substructure circular velocity v_{peak}. The ten different curves correspond to different Monte-Carlo realizations of a Galactic halo of substructure halos. The flux is averaged over 4π steradian and can be compared with the flux from the smooth halo from Fig. 4.8 and Fig. 4.11.

4.2.2.2 The flux due to substructure in prolate and oblate halos

Not only is the mean flux at a given position on the sky dominated by substructure halos, the spatial distribution of flux across the sky will be determined by the substructure. The convergence study by Ghigna *et al.* [62] shows that substructure halos trace the global mass distribution of the halo. Therefore, we can use the N-body simulations to generate Monte-Carlo distributions of substructure halos and construct all-sky maps of the expected gamma-ray flux. We take a random particle from the simulation and assign a circular velocity from a distribution $dn(v_c)/dv_c \propto v_c^{-3.8}$. For each sub-halo we calculate its total annihilation flux and then repeat the process until we have 500,000 halos above a circular velocity of 1kms^{-1}.

Figure 4.15(a) and Fig. 4.15(b) show the resulting sky distribution of flux from sub-halos binned in one degree bins where the observer has been placed in the short and long axis of the simulation respectively. Large substructure halos, such as the Magellanic Clouds in our own halo, will contain its own gravitationally bound sub-halos which leads to clustering of gamma-ray emission in the all sky maps.

Future observations are likely to construct deep strip maps therefore in Fig. 4.16 we have binned the flux along lines of constant galactic l and b with the observer placed in the short and long axis of the global density distribution. From these plots we can see that the emission from substructure peaks at the galactic center, as one would expect, this effect is not that different for spherical halos than for prolate or oblate halos.

Figure 4.17 and Fig. 4.18 show Monte-Carlo simulations of halos of substructure that are spherical, prolate and oblate flattened 2:1 and 3:1. In each case, the spherically averaged density profile is taken from Eq. (4.3) and again the observer is placed in either the short or long axis of symmetry. Note that in this case, the positions of the substructure on the sky are completely random and we have averaged over 100 realisations to reduce the noise.

These simulations show that the distribution of flux on the sky can vary significantly depending on the shape of the density distribution and on where the observer is situated within the halo. We can immediately see that the N-body halo is closest to the prolate 2:1 model.

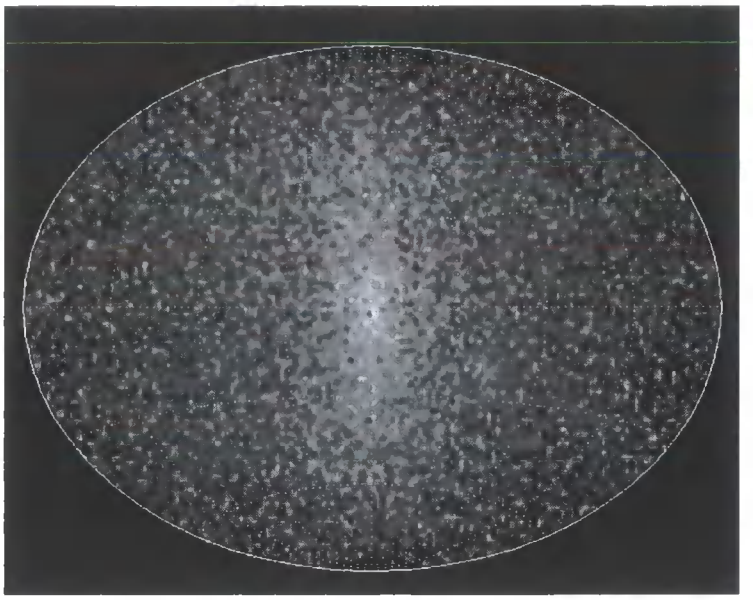

(a)

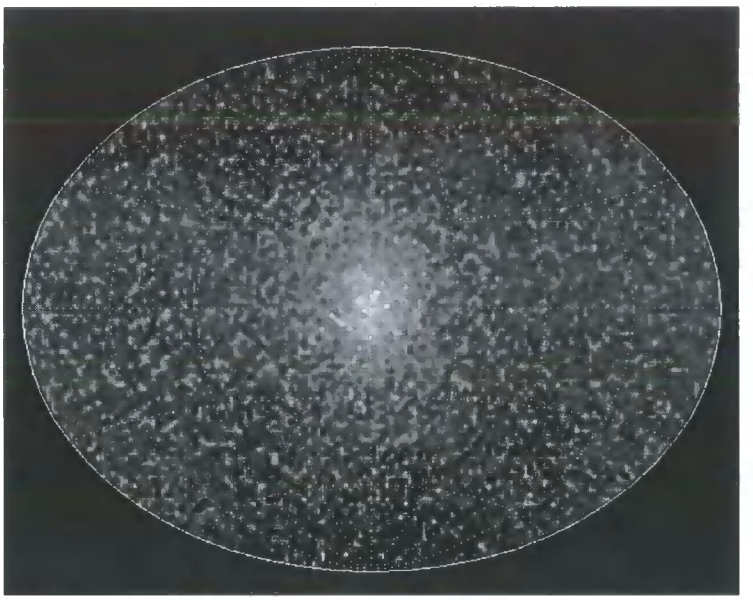

(b)

Figure 4.15: All-sky map of the gamma ray background that arises solely from dark matter substructures. The positions and circular velocities of sub-halos above a circular velocity of 1kms^{-1} are drawn from the N-body simulations but the flux from each halo is calculated analytically. The observer is located on the short (a) and long (b) axis of symmetry. The grey scale corresponds to the log of the flux of annihilation products.

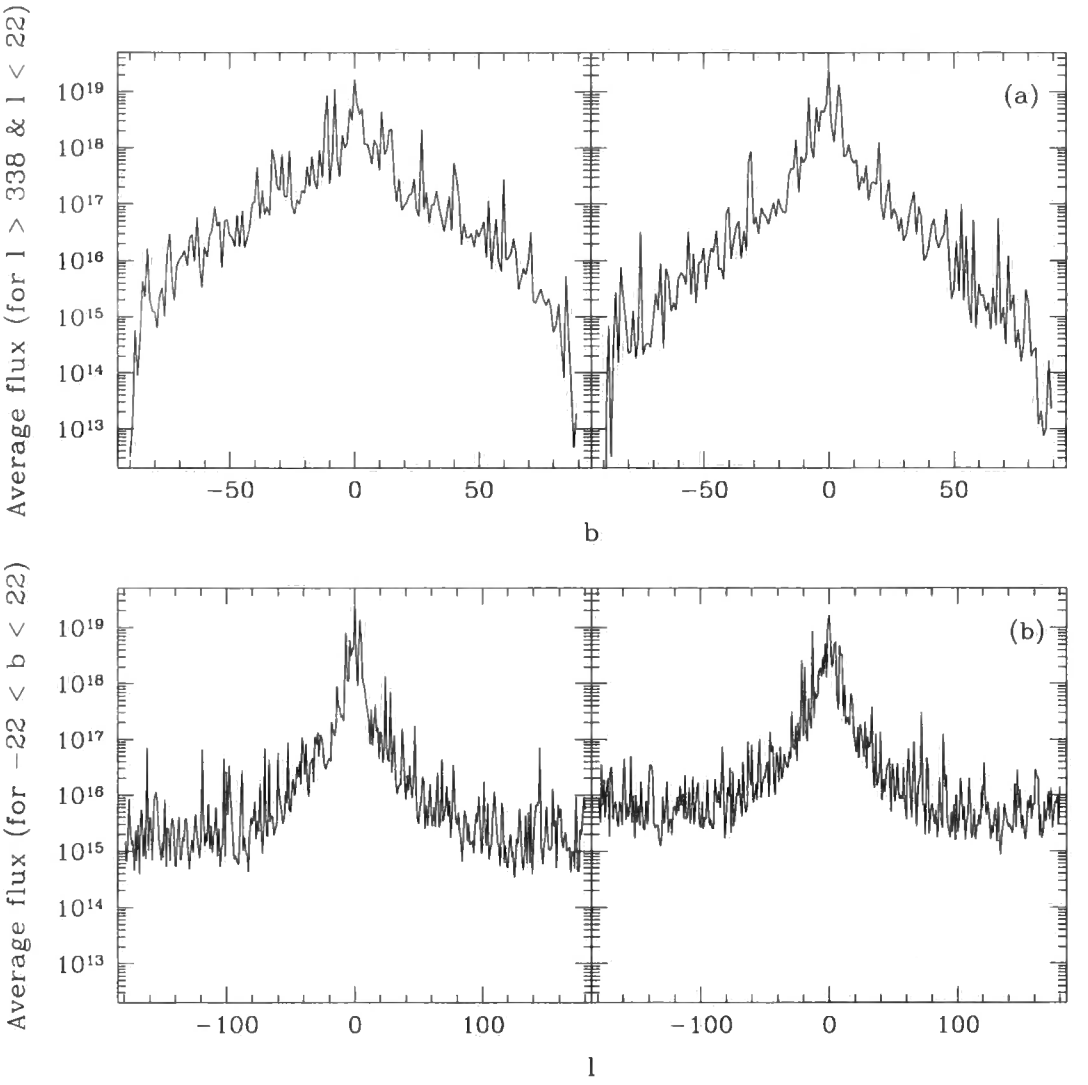

Figure 4.16: The average gamma-ray flux per square degree from dark matter substructure as measured along a great circle of constant galactic latitude (a) and longitude (b). The average has been taken over a strip of width 44 degrees and in in both cases the left hand plot represents the view along the short axis while the right hand side is the view along the long axis.

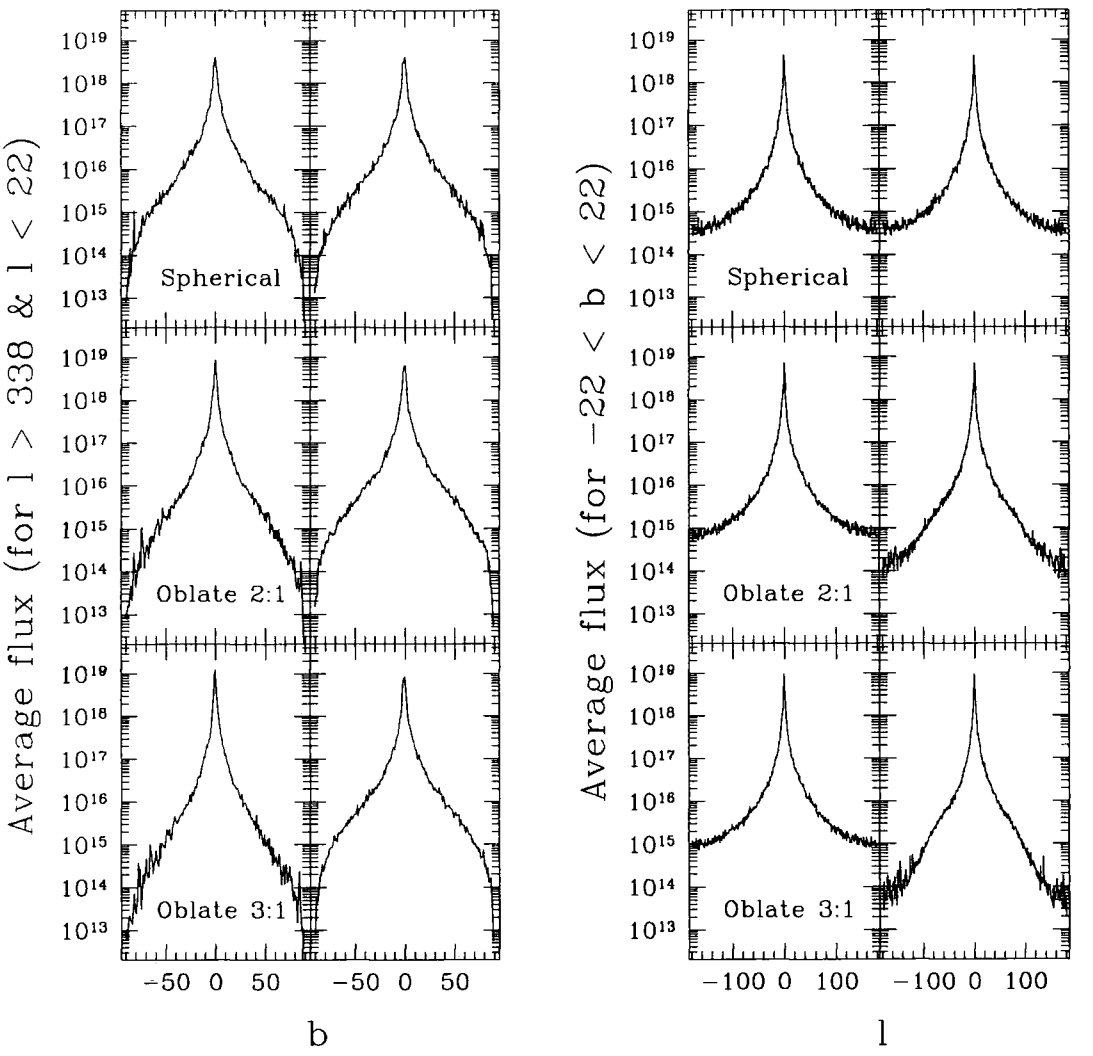

Figure 4.17: The effect of halo shape on the average gamma-ray flux from sub-halos. Substructure halos are randomly drawn from an oblate distribution with the indicated axis ratios. The left panels have the observer placed in the long axis whilst the right panels have the observer in the short axis.

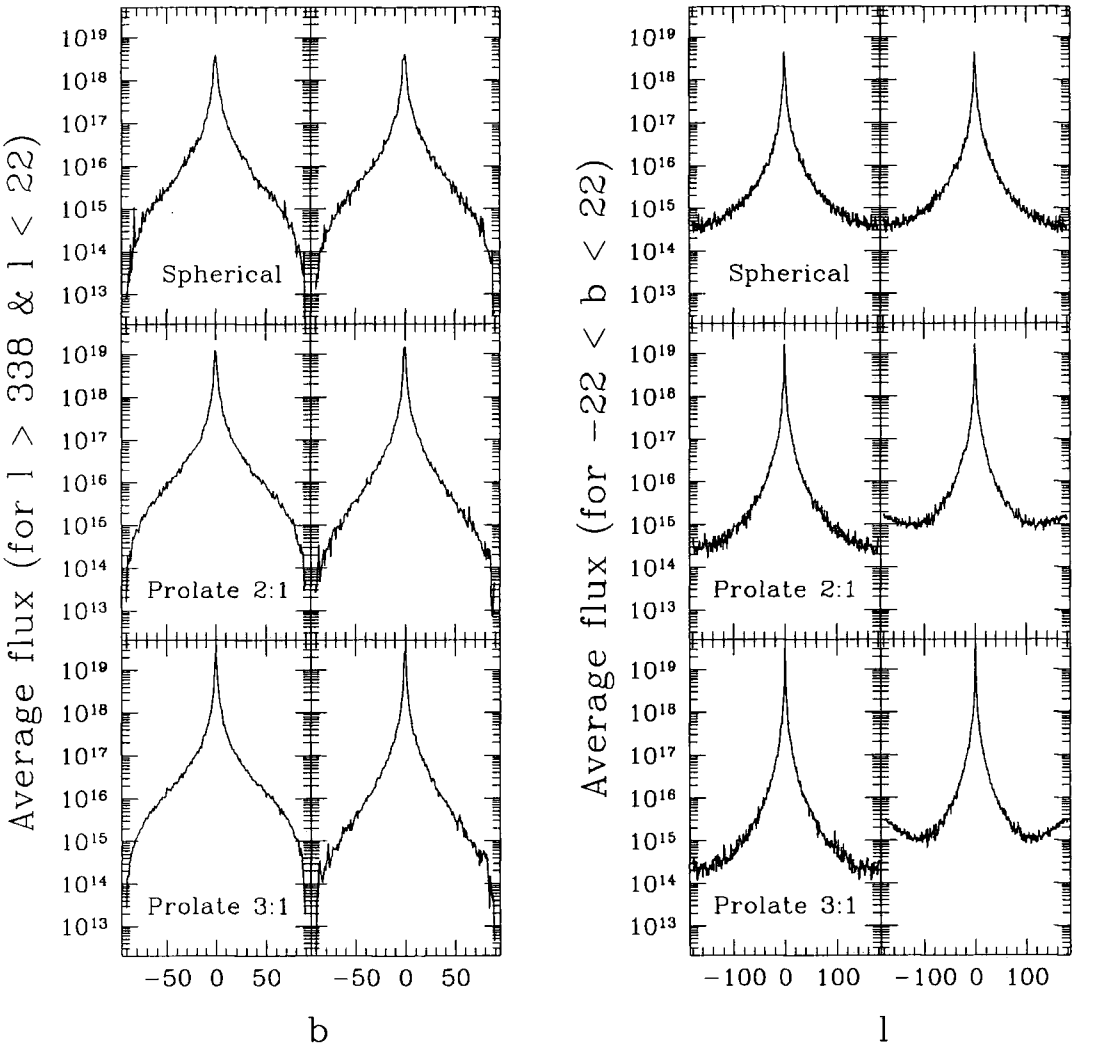

Figure 4.18: As in Figure 4.17 but for a prolate distribution of substructure halos.

4.2.2.3 The distribution of point sources

Individual substructures may be observed and quantified if the resolution of the telescope is sufficient. However, all of the past and present observations would only detect substructure as unresolved point sources. The distribution of their fluxes (and spatial distribution on the sky) may be used to rule out alternative origins, such as extra-galactic sources. In Fig. 4.19 we plot the cumulative distribution of point sources above a given flux within one degree square bins. The two curves consider substructure with peak circular velocities larger than 10 km s^{-1} and 1 km s^{-1}.

Higher resolution simulations are vital to quantify how much substructure survives within the galactic halo, how it is spatially distributed and to quantify the internal structure of surviving substructure. However, Fig. 4.19 gives an idea of what to expect if an all sky survey is carried out that is capable of detecting the brightest substructure halos.

4.2.3 Conclusions for indirect detection

Numerical simulations that follow the growth of structure within a Universe dominated by neutralinos (cold dark matter) have achieved a resolution that allows their global structure and internal structure to be quantified. The density profiles, shapes of dark matter halos, abundance and properties of dark matter substructure, all play an important role in determining the absolute surface brightness of observable products from dark matter annihilation.

We have used the results from the highest resolution simulations ever performed of CDM halos to examine the expected all-sky distribution of gamma-rays from neutralino annihilation. Substructure can boost the expected flux by a factor larger than 10^3 over that originating from a smooth dark matter halo at the Galactic anti-centre. Thus, gamma-ray observations, such as EGRET data, should already have the potential of constraining a large part of the parameter range of the neutralino cross-sections (T. Wibig & A. Wolfendale in preparation). The distinguishing shapes of CDM halos and the unique spatial and flux distribution of point sources from substructure within the Galactic halo should allow a unique identification of observational data with dark matter.

An initial comparison of our results, Fig. 4.16, with the initial observations of EGRET has already been made (FIG. 3 of Ref. [12]). In this comparison, the angular distribution of the diffuse γ-ray flux (extrapolated from the EGRET observations) is consistent to that of our simulated galaxy. However, the continuous flux predicted by our clumpy halo

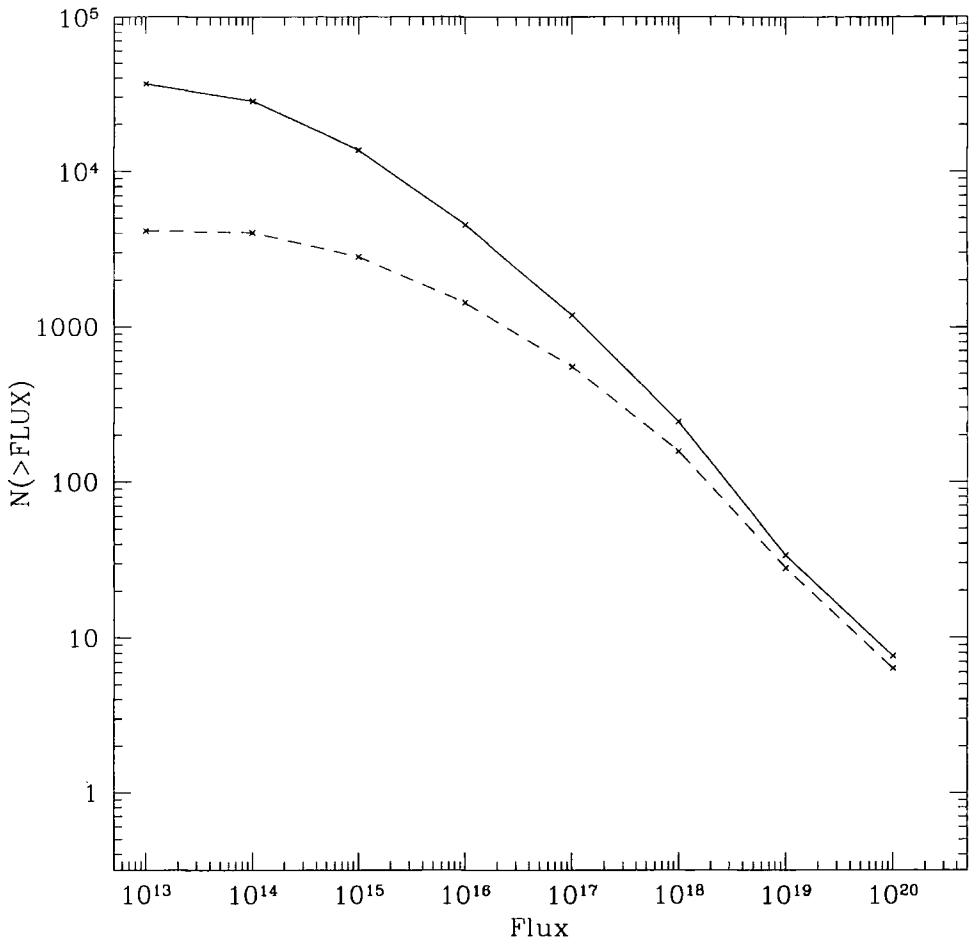

Figure 4.19: The cumulative number of gamma-ray sources above a given flux within a window $\Delta\Omega = 1° \times 1°$. The two curves are for substructure halos with circular velocities larger than 10kms^{-1} (dashed line) and 1kms^{-1} (solid line).

model, at galactic latitudes $-60 < b < 60$, is more than an order of magnitude too bright to be consistent with the observation. The monochromatic line, on the other hand, does lie close that predicted by our model at these latitudes (except for values close to the central part of the galaxy in which the observations are more uncertain). Before making any definitive conclusions we must recall that the background flux between 30GeVand 300GeV, which is precisely the interesting region for supersymmetric matter, has not yet been directly measured, and the values quoted are only extrapolations of the EGRET data [12]. A more significant comparison will only be possible once the this energy range has been measure with precision (by upcoming gamma radiation detectors).

4.3 Direct Detection

An alternative and perhaps more convincing method for confirming the existence and nature of dark matter is by direct detection. The two prime candidate particles require different detection techniques. Neutralinos are the lightest super-symmetric particles, otherwise known as WIMPS (weakly interacting massive particles). These can be identified in a laboratory by looking for phonons or a temperature increase from elastic scattering and nuclei recoil in various materials. Axions are another type of hypothetical particle that have the additional motivation of ensuring that the strong interaction conserves charge-parity; these can be identified by stimulating their conversion to photons within a magnetic cavity (c.f., Ref. [65]).

Many laboratory and some space based experiments utilising these detection methods are in progress and after a great deal of technological development they are beginning to probe the parameter space allowed by cosmological and particle physics constraints (*e.g.* Refs. [84, 2, 18, 11]). These experiments are all highly sensitive to the local density of particles and their velocity distribution [34, 139, 151]. As we have seen earlier in this chapter, the flux of gamma-rays on Earth from neutralino annihilations in the galactic halo is also very sensitive to any substructure in the dark matter [29]. It is therefore crucial to understand the phase space structure of galactic halos in the hierarchical CDM model in order that experiments can be fine tuned to search for the appropriate signals and that potential signals can be interpreted.

Many of the ongoing direct detection experiments adopt the principle that CDM particles passing near Earth have a smooth continuous density distribution with an isotropic Maxwellian velocity distribution with 3-d dispersion ~ 270 km s^{-1}. Recent theoretical work has examined the possibility of velocity anisotropies resulting from halo rotation [23] or triaxiality [75, 49]. Other halo models have also been studied *e.g.* , Sikivie [121], who assumes axially symmetric and cold collapse of matter to infer the presence of caustic rings in the solar neighbourhood. However, two decades of cosmological simulations of the CDM model has clearly demonstrated that dark matter halos form via a series of mergers and accretions of dark matter clumps along highly filamentary mass distributions. Assuming symmetry and locally cold flows is an incorrect over-simplification of the true hierarchical growth [95].

At a given point in a CDM halo, the "smooth" dark matter background arises from material that has been tidally stripped from less massive halos (*e.g.* , Ref. [61]). The

velocity distribution of particles reflects the mass distribution of progenitor halos that have merged and accreted into the final system. The power spectrum of fluctuations in the CDM model allows small dense dark matter halos to collapse at very early epochs. The cutoff scale from the free streaming of neutralinos is approximately $10^{-12}M_{\odot}$ [119], although it is possible that the QCD transition may introduce features in the power spectrum that allow clumping of CDM on even smaller scales [117].

After several decades of code development, matched with increased hardware performance, numerical simulations have finally achieved a resolution of sub-kpc scales within a cosmological context. Recent high resolution numerical simulations can follow the evolution and survival of dark matter substructure halos (sub-halos) as they orbit within dense environments [78, 61, 98]. However, numerical simulations are still a long way from having a resolution scale comparable to that required for direct detection. In the last part of this chapter we explore the phase space distribution of CDM within galactic and sub-galactic halos addressing questions of direct relevance to the direct detection of dark matter. Given our limited resolution compared to laboratory scales, we discuss the extrapolation of our results to Earth mass and solar system scales.

4.3.1 The mean density of dark matter at R_o

The flux of particles through a detector depends on the local density of dark matter and the velocity distribution of particles relative to the Earth's motion through the galaxy [55]. Here we combine several observational constraints on the baryonic distribution within the Milky Way with our numerical simulations of halo structure to determine the possible range of CDM halos that may surround the Galaxy.

The density profile of CDM halos within a specific cosmology follow a single parameter family uniquely determined by their mass. The cosmological scatter of halo concentrations is about 30% for virialised halos not undergoing current mergers [103, 45]. This scatter is largely due to variations in the virial radius at a fixed circular velocity and is sensitive to the presence of large substructure halos. If we consider just the structure internal to v_{peak} then deviations from our density profile are only of the order 10% (c.f. Figure 1 of Ref. [102]). The scatter in central density profiles is small because this region is completely relaxed and rarely contains substructure halos.

4.3.1.1 Upper limit

A single observed value of the circular velocity is insufficient to constrain the properties of the Galactic CDM halo, although the most important quantity to measure is the circular velocity at the Sun's position. Unfortunately, the structural properties of the Galaxy are not well known, *e.g.* the solar position $7 < R_o/\mathrm{kpc} < 8.5$, the disk scale length $2 < r_d/\mathrm{kpc} < 4$, the local circular velocity $190 < v_\odot/\mathrm{kms}^{-1} < 230$ [114]. The maximum density of CDM at R_o can be determined by calculating the minimum contribution to $v_\odot$ from the combined baryonic components.

The mass of an exponential disk is $M_d = 2\pi r_d^2 \Sigma(R_o) e^{R_o/r_d}$ where $\Sigma(R_o)$ is the vertical column density of baryons at the solar position R_o. Direct observations of the local stellar and gaseous distributions or dynamical estimates of the gravitating mass in the disk yield values of $\Sigma(R_o)$ lie in the range $40\text{–}90 M_\odot/\mathrm{pc}^2$ [81, 53, 41, 54]. Thus the baryonic disk mass lies in the range $4 - 8 \times 10^{10} M_\odot$, of which 67% lies within R_o. The Galactic bulge contributes a further mass of $1 - 2 \times 10^{10} M_\odot$ [60].

How does this compare to independent measurements? In order to explain the microlensing optical depth of K-giant stars towards the Galactic bulge, the stellar mass within R_o must be $> 7.6 \times 10^{10} M_\odot$ [20]. This is close to the mass of stars that a maximum disk allows and may be evidence that the Milky Way is a barred galaxy [59]. A further constraint on the central dark matter density can be derived using the kinematics of barred galaxies. The existence of rapidly rotating bars and the strength and position of shocks in their gas flows, both indicate low central dark matter densities [40, 147]. The analyses of these authors constrain the ratio $(v_{disk}/v_{halo})^2 > 2$ measured at $2r_d$ at the 2σ level. Applying these constraints to the Milky Way with $v_\odot = 220$ km s^{-1} and $v_{bulge}(R_o) = 70$ km s^{-1}, implies circular velocities at $2r_d$ of $v_{halo} < 120$ km s^{-1} and $v_{disk} > 170$ km s^{-1}. These parameters for the disk lie in the range discussed above and are illustrated in Fig. 4.20 as our fiducial Galactic model.

Summarising these constraints allows us to estimate the maximum mass of dark matter within R_o, given that we do not want to overestimate the contribution to the observed circular velocity. This gives $M_{CDM} \lesssim 3 \times 10^{10} M_\odot$ for $v_\odot = 220$ km s^{-1}. Adopting the currently favoured ΛCDM model with $\Omega_\Lambda = 0.7$, $\Omega_{CDM} = 0.3$, $\sigma_8 = 0.9$, $h = 0.65$ constrains the structure of the maximum CDM halo to be; $c_{moore} = 6$ ($c_{nfw} = 9$), $v_{peak} = 153$ km s^{-1}, $R_{vir} = 250$ kpc, $v_{vir} = 124$ km s^{-1}, $M_{vir} = 9 \times 10^{11} M_\odot$, $R(v_{peak}) = 52$ kpc. Using the halo density profile defined in Chapter 2 we find a mean density of dark

matter $\rho_{CDM}(R_o) \lesssim 0.23$ (GeV cm^{-3}) (adopting an NFW profile with inner cusp of -1 would lower this value by about 15%). For $v_\odot = 230$ km s^{-1} this density could rise by 30% to $\rho_{CDM}(R_o) = 0.3$ (GeV cm^{-3}).

4.3.1.2 Lower limit

A lower limit to the mass of the Galactic halo can be found assuming that it must be massive enough to "cool" the observed quantity of baryons to form the visible galaxy [150, 105]. This assumes that those baryons initially outside r_{vir} have not had time to cool and reach the central disk. This is probably an underestimate of the halo mass since a large fraction of the baryons may be external to the disk in a warm component – perhaps ejected via supernovæ feedback which is an essential ingredient to galaxy formation in the CDM model.

To estimate a lower limit to the halo mass we take a baryon fraction given by the upper limit from nucleosynthesis, $\Omega_b = 0.019h^{-2}$ [137] and a low Hubble constant $h = 0.6$. For a total baryonic mass of $8 \times 10^{10} M_\odot$, the halo mass must be $M_{vir} > (\Omega_o/\Omega_b) M_{baryon} > 4.6 \times 10^{11} M_\odot$ in order to cool the observed amount of baryons (this calculation limits the total amount of ejected baryons to be less than the mass that currently resides in the Galaxy). Within our adopted ΛCDM model this minimum CDM halo would have a density profile with parameters; $c_{moore} = 6$, $R_{vir} = 200$ kpc, $v_{vir} = 100$ km s^{-1}, $v_{peak} = 125$ km s^{-1}, $R(v_{peak}) = 40$ kpc and $M_{vir} = 4.6 \times 10^{11} M_\odot$. This leads to a lower limit of $\rho_{CDM}(R_o) \gtrsim 0.18$ (GeV cm^{-3}).

Although the Galactic CDM halo is tightly constrained we find that a ΛCDM halo is compatible with the observational constraints. Our fiducial Galactic model is also consistent with the total mass inferred from the orbits of its satellites [152] and the value of the circular velocity $v_c(50\text{kpc}) \approx 200$ km s^{-1} found from modelling the Sagittarius tidal stream [72].

Detailed modelling of the thickness of the Galactic gas disk provides another constraint on the local dark matter density [106]. Finally, we note that it remains to be resolved whether or not the adiabatic contraction from the cooling baryons would increase the central CDM density beyond that allowed by the observations [8].

4.3.2 Structure in density space

The previous calculation of the dark matter density assumes that the particles are smoothly distributed. If the dark matter is physically clustered on small scales then this estimate

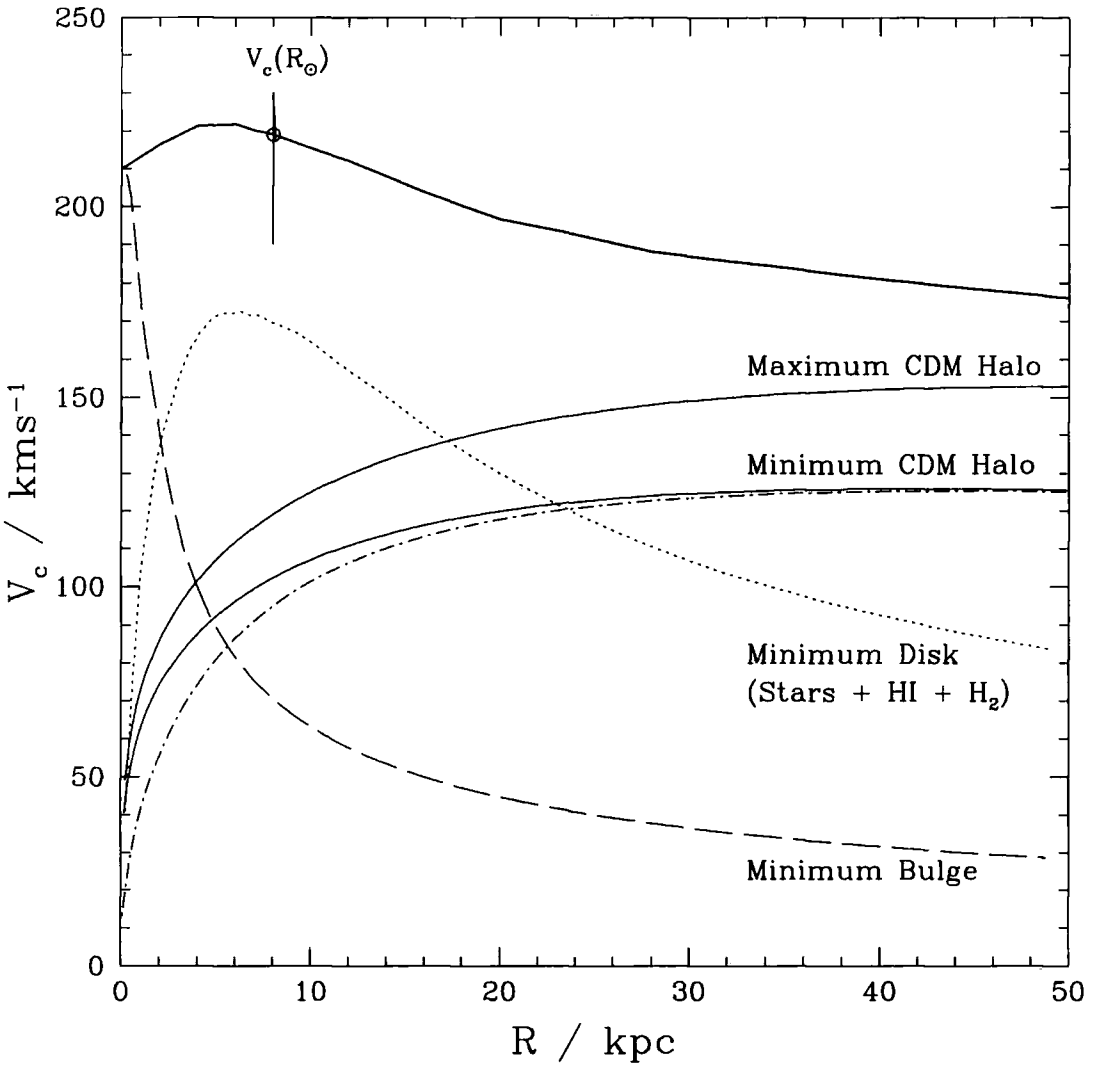

Figure 4.20: The dashed and dotted curves show the minimum contribution to the Galactic circular velocity curve from bulge and disk components respectively. The solid curves show the minimum and maximum allowed CDM halos with central density cusp $\rho(r) \propto r^{-1.5}$. The upper thick solid curve is the total circular velocity profile of the Galaxy for the case in which the CDM halo is the maximum allowed by observational constraints. The minimum CDM halo is the least massive halo that can cool the observed mass of baryons within a Hubble time. The dot–dashed curve is a minimum "NFW" halo with central cusp $\rho(r) \propto r^{-1}$.

Figure 4.21: The evolution of a dark matter sub-halo orbiting on a circular polar orbit within a Galactic potential at 20 kpc. The snapshot is after 3 Gyrs, about 5 orbits. The tidal streams of dark matter lead and trail the surviving dark matter clump of which just 0.3 percent of the initial mass remains bound.

could radically change. For example, if the first objects that collapse in the CDM hierarchy are small and dense enough, they will survive the Galaxy's tidal field and remain bound. The chances of the Earth moving through one of these clumps may be so small that direct detection would not succeed. Here we discuss the tidally limited structure of CDM halos within halos.

Even our highest resolution simulations show little substructure within about 10% of the virial radius. This is primarily a resolution effect since we do not have enough particles to resolve the cores of tidally stripped halos. CDM halos have singular cuspy profiles on all mass scales simulated to-date from $10^6 M_\odot$ to $10^{15} M_\odot$, therefore a central

core will always survive but would require extremely high mass resolution to resolve it.

If the number density of sub-halos continues as a power law to very small masses, would we expect a smooth component of matter at the solar radius? This question is quite subtle since the surviving fraction of halos at a given radius depends also on how the parent halo is assembled, *i.e.* is the formation dominated by major (similar mass) mergers or by accretion driven growth? In the former case halos will always be smooth since the halo centers coalesce to form a single system. In the latter case, halo cores always survive but may not have much mass attached to them. Further simulations and analytic modeling are required to fully address this question, here we make an estimate of the radius at which accreted sub-halos can retain most of their mass intact from the Galactic tidal field.

Although it is physically impossible to completely disrupt a CDM sub-halo, once the tidal radius, r_t, imposed by the Galaxy approaches the radius at which the density profile becomes shallower than -2, the sub-halo loses mass rapidly. If $r_t > r_{peak}$ then the halo will be stable and lose very little mass. This behaviour can be understood in terms of the energy distribution of particles compared with the escape velocity at different radii as discussed in Chapter 2. This process is illustrated in Fig. 4.21 in which we examine tidal mass loss for the extreme case. We construct an equilibrium dark matter halo with a peak circular velocity of 10 km s^{-1} using 10^7 particles, force softening of 10 parsecs and isotropic particle orbits. The model is an equilibrium Hernquist profile that has an inner density profile $\rho(r) \propto r^{-1}$ and is essentially a equilibrium replica of the Draco halo simulated earlier.

Figure 4.21 shows the evolution of this model placed on a circular orbit within a Galactic potential for three billion years. The model has been constructed such that the tidal radius imposed by the Milky Way is equal to the radius at which the satellite's circular velocity peaks (this is the position at which the density profile becomes shallower than $\rho(r) \propto r^{-2}$). Most of the mass has been stripped away by tidal forces and now lies in two symmetric tidal tails of material that completely wrap around the entire orbit. In Fig. 4.22 we plot the evolution of the circular velocity curve and density profile of this satellite.

The mass loss is continuous as particles on radial orbits escape, which in turn decreases the tidal radius allowing more particles to escape. Fig 4.23 shows the same satellite orbiting at 40 kpc within the same potential. In this case the tidal radius imposed by the Galaxy is twice as large and lies beyond the inner core causing the satellite to lose mass

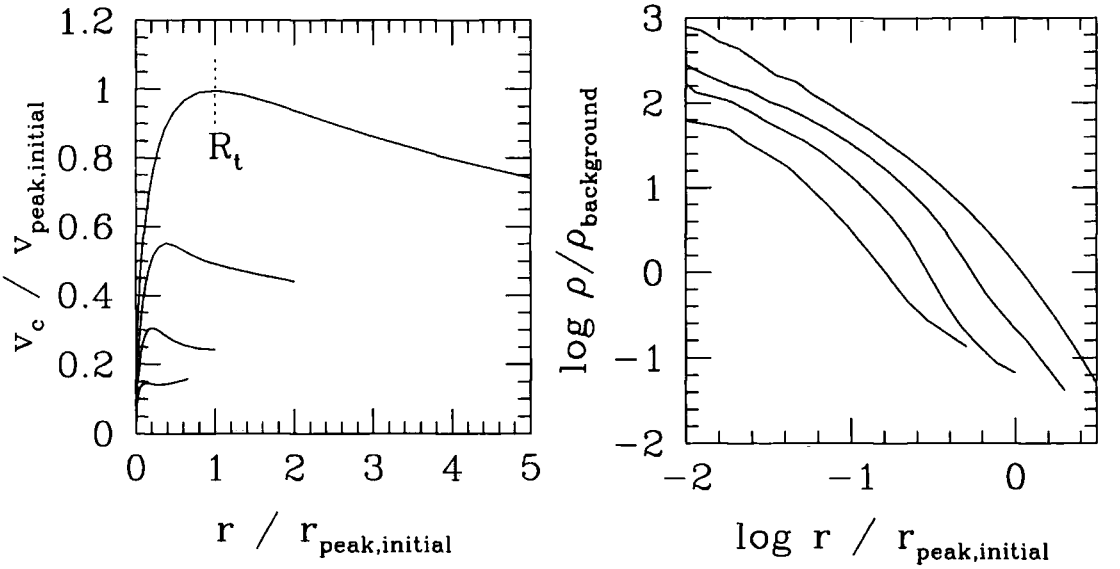

Figure 4.22: The evolution of the circular velocity and density profiles of the satellite shown in Fig. 4.21. The curves show the initial configuration and subsequent times of 1, 2 and 3 Gyrs. The satellite is on a circular orbit at 20 kpc from the center of a Galactic potential and the theoretical tidal radius (R_t) for this orbit is indicated.

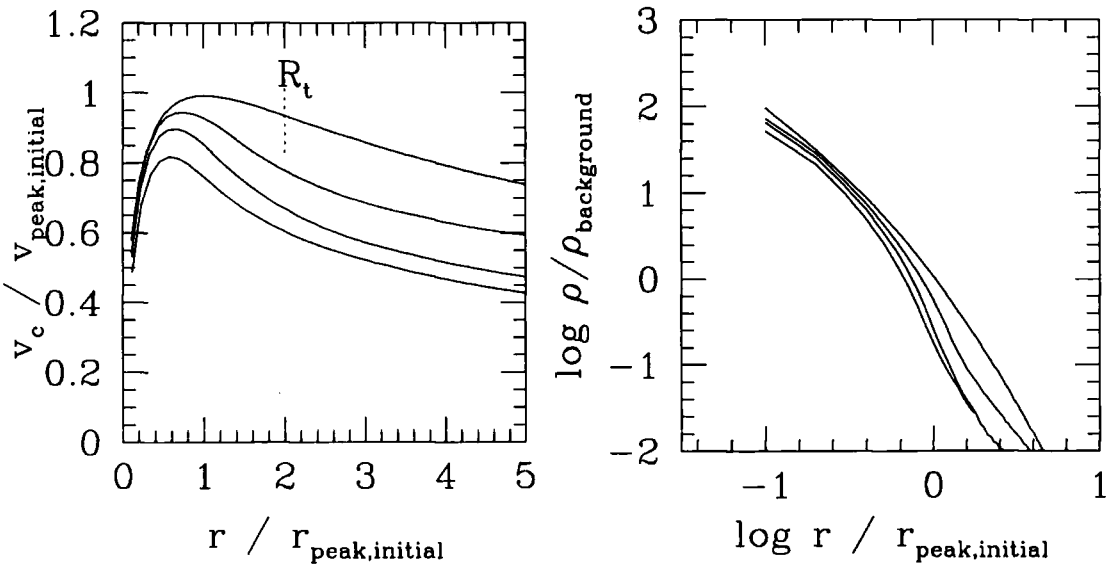

Figure 4.23: The evolution of the circular velocity and density profiles of the satellite moving on a circular orbit at 40 kpc from the center of a Galactic potential. The curves show the initial configuration and subsequent times of 1, 2 and 3 Gyrs.

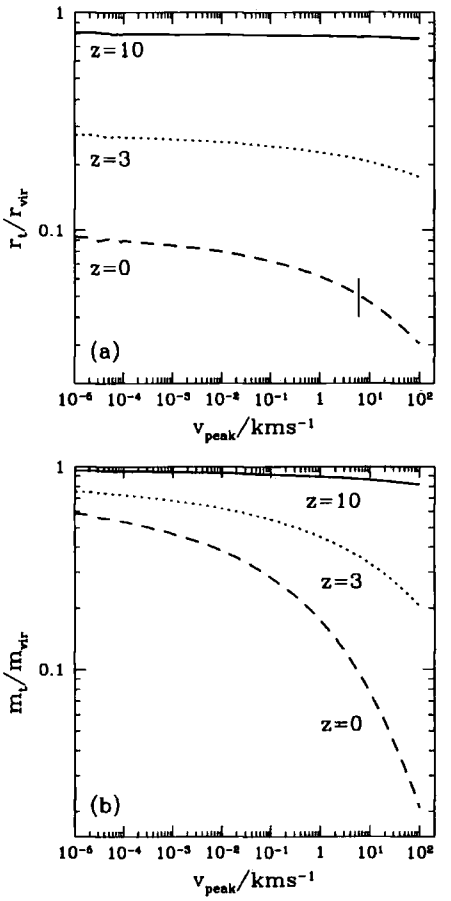

Figure 4.24: The upper panel shows the ratio of tidal radius to virial radius for CDM sub-halos of a given peak circular velocity orbiting at a distance of $R_o = 8$ kpc from the center of a $10^{12} M_\odot$ CDM halo. We consider satellites with concentrations scaling from the fiducial ΛCDM model with structural parameters defined at three different redshifts. We plot results down to halos with characteristic velocity of 1 cm s^{-1} which is roughly the free streaming limit for neutralinos. The lower panel shows the ratio of remaining bound mass to the initial virial masses of the sub-halos. If sub-halos enter Galactic progenitor halos at z=10 then more than 90% of their mass remains bound.

less rapidly. Whereas previously we found that after 3 Gyrs only 0.3% of the initial mass remains bound, in this case 40% remains bound at the final time.

Applying these results to sub-halos orbiting within the Milky Way allows us to estimate a radius at which a halo of a given concentration will lose most of its mass to the smooth background, *i.e.* the radius at which the Galactic tidal field truncates the satellite at $r(v_{peak})$. The ratio of r_{peak}/r_{vir} decreases with halo mass (halo concentration increases for small masses) therefore smaller mass halos can survive intact deeper within the Galactic potential. At the location of the Earth within the Galactic halo we estimate that halos with circular velocities larger than ≈ 1 km s^{-1} *accreting today* will lose more than 95% of their mass. Fig. 4.24 shows the tidal radii and masses of CDM sub-halos orbiting on circular orbits at R_o with a CDM parent halo of mass $10^{12}M_{\odot}$. To calculate tidal radii we use the orbital resonance theory derived by Weinberg (1998) which is slightly more stringent than the standard technique of using equipotential surfaces. To make this calculation we have assumed that the concentration $c = r_{vir}/2r_{peak}$ scales with mass as predicted by NFW. Fig. 4.24 shows that the amount of tidally stripped mass depends sensitively on the redshift that sub-halos accrete into the Milky Way. It is possible that the Galactic halo contains a significant fraction of tiny halos which would decrease the dark matter density in the smooth component.

Additional variations to the smooth component may come from the existence of dark matter streams which are the remanents of tidal interactions between halos (such as the ones which we explored in Chapter 3). Overlapping streams could enhance the density of dark matter at R_o, increasing the possibility of a signal detection. However, if the streams are isolated, they would contribute to modulations in the detected signal that could make it more difficult to separate from the background. Further analytic and numerical work is needed to investigate the numbers of streams that are flowing through the solar system; current simulations (*e.g.* . the one discussed at the beginning of this Chapter) are not able to resolve the small scale structure of the Galactic halo at the Solar radius [96].

4.3.3 Conclusions for direct detection

We may draw two main conclusions from this work:

• We combined our halo density profiles with observational constraints on the baryonic content of the Galaxy to infer the local density of dark matter. Observations favour a dominant baryonic component within $R_o = 8$ kpc which leaves a CDM halo that contributes $\lesssim 3 \times 10^{10}M_{\odot}$ within the same radius. This constrains the local dark matter

density to be $\rho(R_o) \lesssim 0.23$ GeV/cm^3 for a Galaxy with $v_\odot = 220$ km s^{-1}.

- We show that halos with circular velocities $\lesssim 1$ km s^{-1} can survive orbiting at the solar position within the Galactic potential. Since the central Galactic halo is in place by z=10, nearly all of the accreted halos will remain intact and retain most of their mass. The presence of a smooth component of dark matter at R_o depends on the detailed merger history of the Galaxy and on the internal structure of the first CDM halos to collapse with characteristic velocities of 1 m s^{-1} – 1 km s^{-1}.

Chapter 5

What we have learned and what remains to be done

We have investigated the interactions that occur when halos orbit within other halos. By applying well established theory and making detailed numerical simulations it is possible to explain the behaviour of tidally limited N-body systems and to make interesting predictions that are relevant to the properties of astrophysical objects.

A simple satellite-halo interaction allowed us to understand the tidal evolution of halos within halos. An important result was that sub-halos suffer nearly linear mass loss while their circular velocity varies by at most 20% as it orbits within a parent halo. We can also identify the reason for this mass loss: the potential of the sub-halo is continually changing. Tidal stripping removes particles from its edge modifying the sub-halos' structure; after many orbits the potential difference between the core and the edge of the sub-halo is low enough that the random velocity of the particles within it is sufficient to tear it apart.

Although the simple satellite-halo simulation has already helped us to better understand the tidal interactions between halos, much of the parameter space for such encounters is yet to be explored. We are very interested in extending this work to study the effects of satellite orbit, and satellite/parent mass ratios. Which would allow us to quantify the effects of changing these parameters on mass loss.

Varying the satellite mass (with fixed parent mass) will allow us to characterize the effects of dynamical friction for NFW type systems. The factor of 2 difference in the abundance of sub-halos between ΛCDM and sCDM halos may be due to due to dynamical effects which we will also explore.

We are currently setting up the initial conditions for many of these simulations and others are under way, we expect to have some results in the near future.

By performing detailed numerical simulations of the interaction of galactic halos within clusters (using a combination of equilibrium models for compound galactic halos) we were

able to find a possible origin for a particular feature of diffuse light in the Centaurus Cluster.

We investigated the response of galaxies of different morphologies to tidal shocks as they pass pericentre in a cluster potential. The only scenario that gave rise to tidal debris with the same characteristics of the Centaurus arc was a luminous spiral galaxy with a disk co-rotating with its passage past pericentre. This encounter geometry imparts the maximum energy to the disk stars allowing them to stream away and form long thin tidal tails of stellar debris that trace the orbital path of the galaxy. Only a small fraction of the tidal debris constitutes the Centaurus feature, which is prominent at its current pericentric position where the orbits move closer together.

One could potentially confirm the galactic origin of the Centaurus arc, by finding an over abundance of planetary nebulæ along its length and at redshifts close to that of NGC4709. Somewhere along the tidal tails lies the remnant spheroidal galaxy.

To explain the origin of the Centaurus arc we have made extensive use of the concept of "Galaxy Harassment", this is a natural continuation of the broader questions of the dynamical interaction of galactic halos. We will now go on to perform a large number of numerical simulations which will allow us to explore the large parameter space of interactions between disk+halo models orbiting within deeper potentials.

The ultimate aim is to continue this line of investigations leading to construct a complete simulation of more realistic multicomponent galactic halos (i.e. with discs of stars and bulges) and to further our understanding of the response of disks to tidal shocks.

We have already attempted one such simulation in which we used equilibrium models of disk galaxies to replace all of the halos above a certain mass threshold within a cluster that forms hierarchically in a CDM model. This time, at each redshift we would look for galactic size halos and replace them with suitable models that contained disks and (in some cases) bulges. Unfortunately, even after the first of these replacements the simulation required much more computing time that was available at hand and thus we have suspended the project for the moment. We hope that it will soon be possible to continue this line of investigation which will be the first attempt at modeling the detailed small scale structure of a cluster of galaxies and to study the properties and abundance of diffuse intracluster light.

To expand our understanding of the evolution of halos within halos, we took a full cosmological simulation and studied the evolution of the properties of sub-halos; paying particular attention to their peak circular velocities. We were able to construct a merger

tree for the sub-halos: tracing individual structures to the beginning of the simulation. This allowed us to conclude that once a halo falls into another virialised object its peak circular velocity is almost constant; almost 75% of sub-halos vary their peak circular velocity by less than $0.5\text{kms}^{-1}\text{Gyr}^{-1}$. The results from these merger trees varied according to whether we traced the structures forward or backwards in time. When tracing halos from high redshift to the present day it was not possible to recover all of the halos found at the initial redshift. *What happens to these halos?* There are three possible scenarios that may answer this question. The first is that sub-halos merge at early redshifts, via dynamical friction, and only the most massive of these is followed when tracing backwards. Another possibility is that one sub-halo enters another that is more massive but continues to orbit almost intact within this halo, again our method will only be able to trace the more massive one. Finally, upon entering its parent halo, sub-halos may completely disrupt to form tidal streams. The study of Ghigna *et al.* [62] suggest that the third of these possibilities is already ruled out, but further work is needed to confirm this.

We have been able to use our results to make interesting predictions relevant to the detection of dark matter. For the first time, high resolution simulations have been used to map the quantity and distribution of gamma-rays from the annihilation of dark matter particles. The density profiles and shapes of dark matter halos, as well as the properties of their substructure all play an important role in determining the total surface brightness of this radiation. Oblate and prolate halos are easily distinguishable by their gamma-ray signals and deep observations along galactic latitude and longitude could be used to define the shape of the Milky Way's halo. Substructure can boost the overall flux of gamma-rays by a factor larger than 10^3 from that of a smooth halo at the galactic anticentre.

The neutralino is one of the most favoured candidates to make up the CDM component in galaxies. Observations at these energies (such as the EGRET data) should already have the potential to constrain a large amount of the parameter range of masses and cross-sections for this particle. Further work is still needed to make these constraints.

Making a detailed analytical model of the tidal interactions of halos within halos allowed us to extrapolate the simulations down to very small scales. This was particularly relevant to direct detection experiments.

We were able to constrain the local density of dark matter to be $\rho_{CDM}(R_\odot) \lesssim 0.23$ GeVcm^{-3} for a local halo velocity of $v_\odot = 220\text{kms}^{-1}$. The smallest halos resolved in the simulations have circular velocities of 1kms^{-1}, cuspy singular density profiles and concentration parameters that scale according with mass. For smaller halos, with peak

velocities of 1 cms^{-1}, we used analytical models of their tidal interactions to investigate their survival within virialised systems. The central galactic halo is in place by z=10 so nearly all of the accreted halos will remain intact and retain most of their mass. The presence of a smooth component of dark matter at the solar radius depends on the details of the merger history for the Milky Way and on the structure of the first CDM halos that collapse.

A halo that accretes a smaller mass satellite will tidally disrupt it into tidal tails that slowly wrap in phase space (c.f., Ref. [68]). The symmetric tidal tails in Fig. 4.21 illustrated this process for a single high resolution satellite. The presence of dark matter streams may be inferred using directional dark matter detectors such as DRIFT [84], or by finding a highly peaked signal resulting from particles entering the detector with similar energies.

In our simulation the phase space distribution is smooth at $R_\odot$. However we can only resolve subhalos as small as $10^8 M_\odot$ which have internal velocity dispersions of order 10 km s^{-1} and can phase wrap several times around the Galaxy in a Hubble time. Therefore in a small patch of phase space we find multiple streams from the same tidally disrupted halos. If we had infinite resolution and examined a volume that was one parsec on a side we would then be sensitive to the substructure within our poorly resolved $10^8 M_\odot$ halos.

Future analytic work is therefore clearly necessary to resolve these issues. However, it is possible that the density of dark matter in the solar system is zero, or that the solar system may be moving through a single stream of CDM particles that has bulk motion of ≈ 200 km s^{-1}, with a velocity distribution of only a few m s^{-1}.

Appendix A | *Cuspy halo profiles*

In chapters 2 and 4 we have made extensive use of the NFW and Moore *et al.* density profiles for cold dark matter (CDM) halos. We use this section of the thesis to present some general results for both.

These profiles are particular cases of the general family:

$$\rho(r) = \frac{\rho_0}{(r/a)^{\gamma}[1+(r/a)^{\alpha}]^{(\beta-\gamma)/\alpha}}$$

Here, ρ_0 is a characteristic density that can be determined for each halo and a is a characteristic radius that is determined through the concentration, $c = r_{vir}/a$, which in turn is determined by cosmology and the halo mass. It turns out that simulated halos are well fitted by this type of profile for a full range of masses that span from clusters of galaxies to dwarfs. Navarro *et al.* [103] were the first to point out that these profiles were universal and develop a systematic way of determining the parameters ρ_0, a, c (The full procedure is explained in Refs. [103, 104]).

This way of writing the profile allows us to find its asymptotic behaviour easily:

$$\begin{aligned} r \to \infty \quad \rho(r) \quad &\to \quad (r/a)^{-\beta} \\ r \to 0 \quad \rho(r) \quad &\to \quad (r/a)^{-\gamma} \end{aligned}$$

and α defines the sharpness of the change from one slope to the other while a determines its location in r.

Originally, simulated dark matter halos were thought to follow a modified isothermal distribution, $(\alpha,\beta,\gamma) = (2,2,0)$ which was used extensively in the analysis of observed circular rotation curves. Recent high resolution N-body simulations lead to different values for (α,β,γ).

A.1 The NFW profile

For this profile we have that $(\alpha,\beta,\gamma) = (1,3,1)$ and we may write

$$\rho_{nfw}(r) = \frac{\rho_{0-nfw}}{(r/a)(1+r/a)^2} \tag{A.1}$$

Once we have the density distribution many physical quantities are easy to find:

• The total mass within radius r.

Considering spherical halos, the mass enclosed within a radius is found by integrating the density

$$M(r) = 4\pi \int_0^r \rho(r') r'^2 \, dr'$$

so, for this particular profile

$$M_{nfw}(r) = 4\pi \rho_{0-nfw} \int_0^r \frac{r'^2 \, dr'}{(r'/a)(1 + r'/a)^2} \tag{A.2}$$

Integrals of the type in equation A.2 will appear many times when working with these profiles so it is convenient to define its functional form. First we make the change of variable $x = r/a$; thus, $dx = dr/a$ and

$$\begin{aligned} a^3 f_{nfw}(x) &= a^3 \int_0^x \frac{x' \, dx'}{(1 + x')^2} \\ &= a^3 \left(\frac{1}{1 + x'} + \ln(1 + x') \right) \Big|_0^x \\ &= a^3 \left(\ln(1 + x) - \frac{x}{1 + x} \right) \end{aligned}$$

Which gives an expression for the mass as a function of radius:

$$M_{nfw}(r) = 4\pi \rho_{0-nfw} a^3 f_{nfw}(x)$$

It is convenient to define a characteristic mass and radius for these halos. Typically the virial radius, R_{vir} is used for this purpose. For a standard CDM universe (i.e. one in which $\Omega = \Omega_{matter} = 1$) it is defined as the radius that encloses a region for which the mean density of a halo is 200 times that of the background*. This also defines a characteristic mass for the halo; the virial mass M_{vir} which, for spherical halos, is related to the virial radius by:

$$M_{vir} = \frac{800\pi}{3} \rho_0 R_{vir}^3$$

Using this definition we write the mass within radius r as:

$$M_{nfw}(r) = M_{vir} \frac{f_{nfw}(x)}{f_{nfw}(c_{nfw})} \tag{A.3}$$

*This density contrast is a function of cosmology; for an $\Omega = 1$; $\Omega_{matter} = .3$, $\Lambda = .7$ universe instead of 200 it is ≈ 340

Where we must recall that $x = r/a$ and $c_{nfw} \equiv R_{vir}/a$ is the concentration (the concentration parameter is also defined by the virial mass of the halo as discussed in Refs. [104, 45] so it turns out that CDM halos are completely defined by only one parameter).

• The potential at r.

The Newtonian potential (per unit mass) of a spherically symmetric density distribution is

$$\Phi(r) = -4\pi G \left[\frac{1}{r}\int_0^r \rho(r')r'^2\,dr' + \int_r^\infty \rho(r')r'\,dr'\right] \tag{A.4}$$

We have already solved the first of these integrals (it is simply $M(x)$), the remaining integral we solve by making the same variable change as before

$$\begin{aligned} I_{nfw}(r) &= \int_r^\infty \rho_{nfw}(r')r'\,dr' \\ &= \rho_{0-nfw}a^2 \int_x^\infty \frac{dx'}{1+x'} \\ &= -\rho_{0-nfw}a^2 \left(\frac{1}{1+x'}\right)\Big|_x^\infty \\ &= \rho_{0-nfw}a^2 \left(\frac{1}{1+x}\right) \end{aligned}$$

and so, the potential for the nfw profile (written in terms of the virial mass and concentration) is:

$$\Phi_{nfw}(r) = -\frac{GM_{vir}}{af_{nfw}(c_{nfw})}\left[\frac{f_{nfw}(x) + \frac{x}{1+x}}{x}\right] \tag{A.5}$$

• The orbital frequency of circular orbits.

The equation of motion of a point particle at distance r from the center of potential of an NFW density distribution may be written as:

$$\frac{d^2\vec{r}}{dt^2} = F(r)\hat{e}_r = -\frac{d\Phi}{dr}\hat{e}_r$$

if we now consider only the radial part of this expression and circular orbits of radius r

$$r\Omega^2 = \frac{d\Phi}{dr} = \frac{GM(r)}{r^2}$$

Here we have defined the *orbital frequency*, Ω. We write it in terms of the same parameters as before

$$\Omega^2_{nfw} = \frac{GM_{nfw}(r)}{r^3} = \frac{GM_{vir}}{a^3}\frac{f_{nfw}(x)}{x^3 f_{nfw}(c_{nfw})} \tag{A.6}$$

• Circular and escape velocity.

Once you have the potential it is easy to evaluate the circular velocity

$$v^2 = r\frac{d\Phi}{dr} = \frac{GM(r)}{r}$$

or equivalently

$$v_{nfw}^2 = \frac{GM_{vir}}{a}\frac{f_{nfw}(x)}{xf_{nfw}(c_{nfw})} \tag{A.7}$$

The escape velocity can be found by asking what amount of kinetic energy is needed to overcome the potential:

$$\frac{1}{2}v_{esc}^2 = |\Phi(r)|$$

thus

$$v_{esc-nfw}^2 = \frac{2GM_{vir}}{a}\left[\frac{f_{nfw}(x) + \frac{x}{1+x}}{xf_{nfw}(c_{nfw})}\right] \tag{A.8}$$

As we have seen in chapter 2 a robust quantity that can serve to define a halo is the peak circular velocity, v_{peak}. This quantity is also important because it is more easily observed than the virial mass or concentration. If the maximum of circular velocity occurs at some radius $x_{peak} = r_{peak}/a$ then

$$v_{peak}^2 = \frac{GM_{vir}}{a}\frac{f_{nfw}(x_{peak})}{x_{peak}f_{nfw}(c_{nfw})} \tag{A.9}$$

To find v_{peak} explicitly we must maximise the circular rotation curve of equation A.7. The implicit first and second derivatives of the velocity are:

$$2v_{nfw}\frac{dv_{nfw}}{dx} = \frac{GM_{vir}}{af_{nfw}(c_{nfw})}\left(\frac{1}{x}\frac{df_{nfw}(x)}{dx} - \frac{f_{nfw}(x)}{x^2}\right) \tag{A.10}$$

$$\left(\frac{dv_{nfw}}{dx}\right)^2 + v_{nfw}\frac{d^2v_{nfw}}{dx^2} = \frac{GM_{vir}}{af_{nfw}(c_{nfw})}\left(\frac{1}{2x}\frac{d^2f_{nfw}(x)}{dx^2} - \frac{1}{x^2}\frac{df_{nfw}(x)}{dx} + \frac{f_{nfw}(x)}{x^3}\right) \tag{A.11}$$

so will need the following derivatives:

$$\frac{df_{nfw}(x)}{dx} = \frac{x}{(1+x)^2}$$

$$\frac{d^2f_{nfw}(x)}{dx^2} = \frac{1-x}{(1+x)^3}$$

The velocity has its critical points at $\frac{dv_{nfw}}{dx} = 0$. From equation A.10 we see that this condition is met when

$$\frac{1}{x}\frac{df_{nfw}(x)}{dx} - \frac{f_{nfw}(x)}{x^2} = 0$$

which is equivalent to

$$2x^2 + x - (1+x)^2 \ln(1+x) = 0 \tag{A.12}$$

equation A.12 has two non negative solutions (one of which we obtain numerically), namely $x = 0$ and $x \approx 2.1625816$. Further substitution of these values into A.11 proves that the circular velocity has a maximum at

$$x_{peak} = 2.16$$

which implies that

$$r_{peak} = 2.16a \tag{A.13}$$

With the peak circular velocity now explicitly defined, we may write all of the interesting physical quantities in terms of this parameter:

$$\begin{aligned}
v^2_{peak} &= \frac{GM_{vir}}{a} \times \frac{f_{nfw}(x_{peak})}{x_{peak} f_{nfw}(c_{nfw})}; \quad f_{nfw}(x_{peak}) \approx 0.4675860 \\
M_{nfw}(r) &= \frac{a v^2_{peak}}{G} \times \frac{x_{peak} f_{nfw}(x)}{f_{nfw}(x_{peak})} \\
\Phi_{nfw}(r) &= -v^2_{peak} \times \frac{x_{peak}}{f_{nfw}(x_{peak})} \left[\frac{f_{nfw}(x) + \frac{x}{1+x}}{x} \right] \\
\Omega^2_{nfw}(r) &= \frac{v^2_{peak}}{a^2} \times \frac{x_{peak} f_{nfw}(x)}{x^3 f_{nfw}(x_{peak})} \\
v^2_{esc-nfw}(r) &= v^2_{peak} \times \frac{2x_{peak}}{f_{nfw}(x_{peak})} \left[\frac{f_{nfw}(x) + \frac{x}{1+x}}{x} \right]
\end{aligned}$$

A.2 The Moore *et al.* profile

Recent very high resolution simulations lead to a profile with $(\alpha,\beta,\gamma) = (1.5,3,1.5)$, thus:

$$\rho_{moore}(r) = \frac{\rho_{0-moore}}{(r/a)^{1.5}[1 + (r/a)^{1.5}]} \tag{A.14}$$

We proceed exactly the same as before to obtain the physical quantities of interest. The different form of the profile leads to the following integrals:

$$\begin{aligned}
a^3 f_{moore}(x) &= a^3 2 \int_0^{\sqrt{x}} \frac{x'^2\, dx'}{(1 + x'^3)} \\
&= a^3 \tfrac{2}{3} \ln(1 + x'^3)\Big|_0^{\sqrt{x}} \\
&= a^3 \tfrac{2}{3} \ln(1 + x^{\frac{3}{2}})
\end{aligned}$$

$$
\begin{aligned}
I_{moore}(r) &= \int_r^\infty \rho_{moore}(r')r'\,dr' \\
&= \rho_{0-moore}a^2 2\int_{\sqrt{x}}^\infty \frac{dx'}{1+x'^3} \\
&= \rho_{0-moore}a^2\left\{\frac{1}{3}\ln\left[\frac{(1+x')^2}{x'^2-x'+1}\right]+\frac{2}{\sqrt{3}}\arctan\left(\frac{2x'-1}{\sqrt{3}}\right)\right\}\Bigg|_x^\infty \\
&= \rho_{0-moore}a^2\left[\frac{\pi}{\sqrt{3}}-\frac{1}{3}\ln\left(\frac{x+2\sqrt{x}+1}{x-\sqrt{x}+1}\right)-\frac{2}{\sqrt{3}}\arctan\left(\frac{2\sqrt{x}-1}{\sqrt{3}}\right)\right]
\end{aligned}
$$

With these results we are now able to recover the physical parameters (to begin with, we will write them in terms of the virial mass and concentration, as before).

- The total mass within radius r.

$$M_{moore}(r) = M_{vir}\frac{f_{moore}(x)}{f_{moore}(c_{moore})} \tag{A.15}$$

- The potential at r.

$$
\Phi_{moore}(r) = -\frac{GM_{vir}}{af_{moore}(c_{moore})}\left\{\frac{f_{moore}(x)}{x}+\left[\frac{\pi}{\sqrt{3}}-\frac{1}{3}\ln\left(\frac{x+2\sqrt{x}+1}{x-\sqrt{x}+1}\right)-\frac{2}{\sqrt{3}}\arctan\left(\frac{2\sqrt{x}-1}{\sqrt{3}}\right)\right]\right\} \tag{A.16}
$$

- The orbital frequency of circular orbits.

$$\Omega^2_{moore}(r) = \frac{GM_{moore}(r)}{r^3} = \frac{GM_{vir}}{a^3}\frac{f_{moore}(x)}{x^3 f_{moore}(c_{moore})} \tag{A.17}$$

- Circular and escape velocity.

$$v^2_{moore}(r) = \frac{GM_{vir}}{a}\frac{f_{moore}(x)}{xf_{moore}(c_{moore})} \tag{A.18}$$

$$v^2_{esc-moore}(r) = 2|\Phi_{moore}(x)| \tag{A.19}$$

We can see from A.18 that the maximum of circular velocity (at $x_{peak} = r_{peak}/a$) is again of the form:

$$v^2_{peak} = \frac{GM_{vir}}{a}\frac{f_{moore}(x_{peak})}{x_{peak}f_{moore}(c_{moore})} \tag{A.20}$$

The first and second derivatives of the circular velocity are the same as before, but now we have:

$$
\begin{aligned}
\frac{df_{moore}(x)}{dx} &= \frac{x^{1/2}}{1+x^{3/2}} \\
\frac{d^2f_{moore}(x)}{dx^2} &= \frac{1-2x^{3/2}}{2x^{1/2}(1+x^{3/2})^2}
\end{aligned}
$$

The condition for critical points ($\frac{dv_{moore}}{dx} = 0$) now leads to the following equation

$$3x^{3/2} - 2(1 + x^{3/2}) \ln(1 + x^{3/2}) = 0 \tag{A.21}$$

The two non-negative solutions to this are $x = 0$ and $x \approx 1.2496758$ (again, the nontrivial solution was obtained numerically). Thus, the circular velocity for the Moore *et al.* profile has a maximum at

$$x_{peak} = 1.25$$

which implies that

$$r_{peak} = 1.25a \tag{A.22}$$

All of the physical quantities may now be written in terms this velocity:

$$v^2_{peak} = \frac{GM_{vir}}{a} \times \frac{f_{moore}(x_{peak})}{x_{peak} f_{moore}(c_{moore})}; \quad f_{moore}(x_{peak}) \approx 0.4675860 \tag{A.23}$$

$$M_{moore}(r) = \frac{a v^2_{peak}}{G} \times \frac{x_{peak} f_{moore}(x)}{f_{moore}(x_{peak})} \tag{A.24}$$

$$\Phi_{moore}(r) = -v^2_{peak} \times \frac{x_{peak}}{f_{moore}(x_{peak})} \left\{ \frac{f_{moore}(x)}{x} + \left[\frac{\pi}{\sqrt{3}} - \frac{1}{3} \ln \left(\frac{x + 2\sqrt{x} + 1}{x - \sqrt{x} + 1} \right) - \frac{2}{\sqrt{3}} \arctan \left(\frac{2\sqrt{x} - 1}{\sqrt{3}} \right) \right] \right\} \tag{A.25}$$

$$\Omega^2_{moore}(r) = \frac{v^2_{peak}}{a^2} \times \frac{x_{peak} f_{moore}(x)}{x^3 f_{moore}(x_{peak})} \tag{A.26}$$

$$v^2_{esc-moore}(r) = 2|\Phi_{moore}(x)| \tag{A.27}$$

Bibliography

[1] M. Aaronson and E. W. Olszewski. Dark matter in dwarf galaxies. In *IAU Symp. 130: Large Scale Structures of the Universe*, volume 130, pages 409+, 1988. Provided by the NASA Astrophysics Data System.

[2] R. Abusaidi, D. S. Akerib, P. D. Barnes, D. A. Bauer, A. Bolozdynya, P. L. Brink, R. Bunker, B. Cabrera, D. O. Caldwell, J. P. Castle, R. M. Clarke, P. Colling, M. B. Crisler, A. Cummings, A. da Silva, and et al. Exclusion limits on the wimp-nucleon cross section from the cryogenic dark matter search. *Physical Review Letters*, 84:5699–5703, June 2000.

[3] C. Alcock, R. A. Allsman, D. R. Alves, T. S. Axelrod, A. C. Becker, D. P. Bennett, K. H. Cook, N. Dalal, A. J. Drake, K. C. Freeman, M. Geha, K. Griest, M. J. Lehner, S. L. Marshall, D. Minniti, C. A. Nelson, B. A. Peterson, P. Popowski, M. R. Pratt, P. J. Quinn, C. W. Stubbs, W. Sutherland, A. B. Tomaney, T. Vandehei, and D. Welch. The MACHO Project: Microlensing Results from 5.7 Years of Large Magellanic Cloud Observations. *ApJ*, 542:281–307, October 2000.

[4] M. Arnaboldi, K. C. Freeman, R. H. Mendez, M. Capaccioli, R. Ciardullo, H. Ford, O. Gerhard, X. Hui, G. H. Jacoby, R. P. Kudritzki, and P. J. Quinn. The kinematics of the planetary nebulae in the outer regions of ngc 4406. *ApJ*, 472:145+, November 1996.

[5] E. A. Baltz, C. Briot, P. Salati, R. Taillet, and J. Silk. Detection of neutralino annihilation photons from external galaxies. *Phys. Rev.*, D61:023514, 2000.

[6] Edward A. Baltz and Joakim Edsjo. Positron propagation and fluxes from neutralino annihilation in the halo. *Phys. Rev.*, D59:023511, 1999.

[7] J. Barnes and G. Efstathiou. Angular momentum from tidal torques. *ApJ*, 319:575–600, August 1987.

[8] J. Barnes and S. D. M. White. The response of a spheroid to a disc field or were bulges ever ellipticals? *MNRAS*, 211:753–765, December 1984.

[9] J. E. Barnes and L. Hernquist. Dynamics of interacting galaxies. *ARA&A*, 30:705–742, 1992.

[10] C. M. Baugh, S. Cole, C. S. Frenk, and C. G. Lacey. The epoch of galaxy formation. *ApJ*, 498:504+, May 1998.

[11] A. Benoit et al. First results of the edelweiss wimp search using a 320-g heat-and-ionization ge detector. `astro-ph/0106094`, 2001.

[12] L. Bergström, J. Edsjö, and C. Gunnarsson. Neutralino gamma-ray signals from accreting halo dark matter. *Phys. Rev. D*, 63:1463b+, April 2001.

[13] L. Bergstrom and P. Ullio. Full one-loop calculation of neutralino annihilation into two photons. *Nuclear Physics B*, 504:27–44, October 1997.

[14] Lars Bergstrom. Non-baryonic dark matter. *Nucl. Phys. Proc. Suppl.*, 70:31–42, 1999.

[15] Lars Bergstrom, Joakim Edsjo, and Paolo Gondolo. Indirect detection of dark matter in km-size neutrino telescopes. *Phys. Rev.*, D58:103519, 1998.

[16] Lars Bergstrom, Joakim Edsjo, Paolo Gondolo, and Piero Ullio. Clumpy neutralino dark matter. *Phys. Rev.*, D59:043506, 1999.

[17] Lars Bergstrom, Piero Ullio, and James H. Buckley. Observability of gamma rays from dark matter neutralino annihilations in the milky way halo. *Astropart. Phys.*, 9:137–162, 1998.

[18] R. Bernabei, P. Belli, R. Cerulli, F. Montecchia, M. Amato, G. Ignesti, A. Incicchitti, D. Prosperi, C. J. Dai, H. L. He, H. H. Kuang, and J. M. Ma. Search for wimp annual modulation signature: results from dama/nai-3 and dama/nai-4 and the global combined analysis. *Physics Letters B*, 480:23–31, May 2000.

[19] G. M. Bernstein, R. C. Nichol, J. A. Tyson, M. P. Ulmer, and D. Wittman. The luminosity function of the coma cluster core for -25<m/r<-9.4. *AJ*, 110:1507+, October 1995.

[20] J. Binney, N. Bissantz, and O. Gerhard. Is galactic structure compatible with microlensing data? *ApJ Lett.*, 537:L99–L102, July 2000.

[21] J. Binney and S. Tremaine. *Galactic dynamics.* Princeton, NJ, Princeton University Press, 1987, 747 p., 1987.

[22] Alain Bouquet, Pierre Salati, and Joseph Silk. gamma ray lines as a probe for a cold dark matter halo. *Phys. Rev.*, D40:3168, 1989.

[23] M. Brhlik. Wimp velocity impact on direct dark matter searches. *Physics Letters B*, 464:303–310, October 1999.

[24] G. Bruzual A. and S. Charlot. Spectral evolution of stellar populations using isochrone synthesis. *ApJ*, 405:538–553, March 1993.

[25] A. Burkert. The structure of dark matter halos in dwarf galaxies. *ApJ Lett.*, 447:L25–+, July 1995.

[26] S. Burles, K. M. Nollett, J. W. Truran, and M. S. Turner. Sharpening the predictions of big-bang nucleosynthesis. *Physical Review Letters*, 82:4176–4179, May 1999.

[27] S. Burles, K. M. Nollett, and M. S. Turner. Big bang nucleosynthesis predictions for precision cosmology. *ApJ Lett.*, 552:L1–L5, May 2001.

[28] D. Burstein and C. Heiles. Reddenings derived from h i and galaxy counts - accuracy and maps. *AJ*, 87:1165–1189, August 1982.

[29] C. Calcáneo-Roldán and B. Moore. Surface brightness of dark matter: Unique signatures of neutralino annihilation in the galactic halo. *Phys. Rev. D*, 62:07d+, December 2000.

[30] R. G. Carlberg. Velocity bias in clusters. *ApJ*, 433:468–478, October 1994.

[31] S. Chandrasekhar. Dynamical friction. i. general considerations: the coefficient of dynamical friction. *ApJ*, 97:255–262, March 1943.

[32] Juan I. Collar. Solar-bound weakly interacting massive particles: A no- frills phenomenology. *Phys. Rev.*, D59:063514, 1999.

[33] C. J. Conselice and J. S. Gallagher. Tides, interactions, and fine-scale substructures in galaxy clusters. *AJ*, 117:75–101, January 1999.

[34] C. J. Copi and L. M. Krauss. Angular signatures for galactic halo weakly interacting massive particle scattering in direct detectors: Prospects and challenges. *Phys. Rev. D*, 63:9f3+, February 2001.

[35] A. W. J. Cousins. Response functions in the red and near infrared. *South African Astronomical Observatory Circular*, 6:4+, 1981.

[36] M. Davis, G. Efstathiou, C. S. Frenk, and S. D. M. White. The evolution of large-scale structure in a universe dominated by cold dark matter. *ApJ*, 292:371–394, May 1985.

[37] W. J. G. de Blok and S. S. McGaugh. Testing modified newtonian dynamics with low surface brightness galaxies: Rotation curve fits. *ApJ*, 508:132–140, November 1998.

[38] W. J. G. de Blok, J. M. van der Hulst, and G. D. Bothun. Surface photometry of low surface brightness galaxies. *MNRAS*, 274:235–255, May 1995.

[39] G. de Vaucouleurs. The apparent density of matter in groups and clusters of galaxies. *ApJ*, 131:585+, May 1960.

[40] V. P. Debattista and J. A. Sellwood. Dynamical friction and the distribution of dark matter in barred galaxies. *ApJ Lett.*, 493:L5–+, January 1998.

[41] W. Dehnen and J. J. Binney. Local stellar kinematics from hipparcos data. *MNRAS*, 298:387–394, August 1998.

[42] D. D. Dixon, D. H. Hartmann, E. D. Kolaczyk, J. Samimi, R. Diehl, G. Kanbach, H. Mayer-Hasselwander, and A. W. Strong. Evidence for a galactic gamma-ray halo. *New Astronomy*, 3:539–561, October 1998.

[43] A. K. Drukier, K. Freese, and D. N. Spergel. Detecting cold dark-matter candidates. *Phys. Rev. D*, 33:3495–3508, June 1986.

[44] J. Dubinski. The origin of the brightest cluster galaxies. *ApJ*, 502:141+, July 1998.

[45] V. R. Eke, J. Navarro, and M. Steinmetz. The power spectrum dependence of dark matter halo concentrations. *submited to ApJ*, `astro-ph/0012337` , December 2000.

[46] V. R. Eke, J. F. Navarro, and C. S. Frenk. The evolution of x-ray clusters in a low-density universe. *ApJ*, 503:569+, August 1998.

[47] John Ellis. Particle candidates for dark matter. *Phys. Scripta*, T85:221, 2000.

[48] S. Ettori and A. C. Fabian. Rosat pspc observations of 36 high-luminosity clusters of galaxies: constraints on the gas fraction. *MNRAS*, 305:834–848, May 1999.

[49] N. W. Evans, C. M. Carollo, and P. T. de Zeeuw. Triaxial haloes and particle dark matter detection. *MNRAS*, 318:1131–1143, November 2000.

[50] J. J. Feldmeier, R. Ciardullo, and G. H. Jacoby. Planetary nebulae as standard candles. xi. application to spiral galaxies. *ApJ*, 479:231+, April 1997.

[51] H. C. Ferguson, N. R. Tanvir, and T. von Hippel. Detection of intergalactic red-giant-branch stars in the virgo cluster. *Nat*, 391:461+, January 1998.

[52] R. A. Flores and J. R. Primack. Observational and theoretical constraints on singular dark matter halos. *ApJ Lett.*, 427:L1–L4, May 1994.

[53] C. Flynn and B. Fuchs. Density of dark matter in the galactic disk. *MNRAS*, 270:471+, October 1994.

[54] C. Flynn, A. Gould, and J. Bahcall. Faint star counts with hst. In *ASP Conf. Ser. 165: The Third Stromlo Symposium: The Galactic Halo*, pages 387+, 1999.

[55] K. Freese, J. Frieman, and A. Gould. Signal modulation in cold-dark-matter detection. *Phys. Rev. D*, 37:3388–3405, June 1988.

[56] Z. Frei and J. E. Gunn. Generating colors and k corrections from existing catalog data. *AJ*, 108:1476–1485, October 1994.

[57] M. Fukugita, C. J. Hogan, and P. J. E. Peebles. The cosmic baryon budget. *ApJ*, 503:518+, August 1998.

[58] N. Gehrels and P. Michelson. Glast: The next-generation high energy gamma-ray astronomy mission. *Astropart. Phys.*, 11:277–282, 1999.

[59] O. Gerhard. The galactic bulge. In *ASP Conf. Ser. 197: Dynamics of Galaxies: from the Early Universe to the Present*, pages 201+, 2000.

[60] O. E. Gerhard. Dynamics of the galaxy. In *ASP Conf. Ser. 182: Galaxy Dynamics - A Rutgers Symposium*, pages 307+, August 1999.

[61] S. Ghigna, B. Moore, F. Governato, G. Lake, T. Quinn, and J. Stadel. Dark matter haloes within clusters. *MNRAS*, 300:146–162, October 1998.

[62] S. Ghigna, B. Moore, F. Governato, G. Lake, T. Quinn, and J. Stadel. Density profiles and substructure of dark matter halos: Converging results at ultra-high numerical resolution. *ApJ*, 544:616–628, December 2000.

[63] Paolo Gondolo and Joseph Silk. Dark matter annihilation at the galactic center. *Phys. Rev. Lett.*, 83:1719–1722, 1999.

[64] M. D. Gregg and M. J. West. Galaxy disruption as the origin of intracluster light in the coma cluster of galaxies. *Nat*, 396:549–552, 1998.

[65] K. Griest. Calculations of rates for direct detection of neutralino dark matter. *Physical Review Letters*, 61:666–669, August 1988.

[66] J. E. Gunn, B. W. Lee, I. Lerche, D. N. Schramm, and G. Steigman. Some astrophysical consequences of the existence of a heavy stable neutral lepton. *ApJ*, 223:1015–1031, August 1978.

[67] R. C. Hartman, D. L. Bertsch, S. D. Bloom, A. W. Chen, P. Deines-Jones, J. A. Esposito, C. E. Fichtel, D. P. Friedlander, S. D. Hunter, L. M. McDonald, P. Sreekumar, D. J. Thompson, B. B. Jones, Y. C. Lin, P. F. Michelson, P. L. Nolan, W. F. Tompkins, G. Kanbach, H. A. Mayer-Hasselwander, A. Mücke, M. Pohl, O. Reimer, D. A. Kniffen, E. J. Schneid, C. von Montigny, R. Mukherjee, and B. L. Dingus. The third egret catalog of high-energy gamma-ray sources. *ApJS*, 123:79–202, July 1999.

[68] A. Helmi and S. D. M. White. Building up the stellar halo of the galaxy. *MNRAS*, 307:495–517, August 1999.

[69] M. Henriksen and G. Byrd. Tidal triggering of star formation by the galaxy cluster potential. *ApJ*, 459:82+, March 1996.

[70] L. Hernquist and N. Katz. Treesph - a unification of sph with the hierarchical tree method. *ApJS*, 70:419–446, June 1989.

[71] W. Hu, M. Fukugita, M. Zaldarriaga, and M. Tegmark. Cosmic microwave background observables and their cosmological implications. *ApJ*, 549:669–680, March 2001.

[72] R. Ibata, G. F. Lewis, M. Irwin, E. Totten, and T. Quinn. Great circle tidal streams: Evidence for a nearly spherical massive dark halo around the milky way. *ApJ*, 551:294–311, April 2001.

[73] Y. P. Jing and Y. Suto. The density profiles of the dark matter halo are not universal. *ApJ Lett.*, 529:L69–L72, February 2000.

[74] Gerard Jungman, Marc Kamionkowski, and Kim Griest. Supersymmetric dark matter. *Phys. Rept.*, 267:195–373, 1996.

[75] M. Kamionkowski and A. Kinkhabwala. Galactic halo models and particle dark-matter detection. *Phys. Rev. D*, 57:3256–3263, March 1998.

[76] G. Kanbach. The EGRET high energy gamma-ray telescope on GRO. *Bulletin d'Information du Centre de Donnees Stellaires*, 28:69+, March 1985.

[77] F. J. Kerr and D. Lynden-Bell. Review of galactic constants. *MNRAS*, 221:1023–1038, August 1986.

[78] A. Klypin, S. Gottlöber, A. V. Kravtsov, and A. M. Khokhlov. Galaxies in n-body simulations: Overcoming the overmerging problem. *ApJ*, 516:530–551, May 1999.

[79] A. Klypin, A. V. Kravtsov, O. Valenzuela, and F. Prada. Where are the missing galactic satellites? *ApJ*, 522:82–92, September 1999.

[80] A. V. Kravtsov, A. A. Klypin, J. S. Bullock, and J. R. Primack. The cores of dark matter-dominated galaxies: Theory versus observations. *ApJ*, 502:48+, July 1998.

[81] K. Kuijken and G. Gilmore. The galactic disk surface mass density and the galactic force k(z) at z = 1.1 kiloparsecs. *ApJ Lett.*, 367:L9–L13, January 1991.

[82] G. Lake. Detectability of gamma-rays from clumps of dark matter. *Nat*, 346:39+, July 1990.

[83] T. Lasserre, C. Afonso, J. N. Albert, J. Andersen, R. Ansari, É. Aubourg, P. Bareyre, F. Bauer, J. P. Beaulieu, G. Blanc, A. Bouquet, S. Char, X. Charlot, F. Couchot, C. Coutures, F. Derue, R. Ferlet, J. F. Glicenstein, B. Goldman, A. Gould, D. Graff, M. Gros, J. Haissinski, J. C. Hamilton, D. Hardin, J. de Kat, A. Kim, É. Lesquoy, C. Loup, C. Magneville, B. Mansoux, J. B. Marquette, É. Maurice, A. Milsztajn, M. Moniez, N. Palanque-Delabrouille, O. Perdereau, L. Prévot,

N. Regnault, J. Rich, M. Spiro, A. Vidal-Madjar, L. Vigroux, S. Zylberajch, and The EROS collaboration. Not enough stellar mass Machos in the Galactic halo. *Astron. & Astrophys.*, 355:L39–L42, March 2000.

[84] M. J. Lehner, K. Griest, C. J. Martoff, G. E. Masek, T. Ohnuki, D. Snowden-Ifft, and N. J. C. Spooner. The drift project: searching for wimps with a directional detector. In *Dark matter in Astrophysics and Particle Physics*, pages 767+, 1999.

[85] R. W. Lessard. Veritas: the very energetic radiation imaging telescope array system. *Astropart. Phys.*, 11:243–246, 1999.

[86] D. F. Malin. Photographic amplification of faint astronomical images. *Nat*, 276:591–593, December 1978.

[87] D. F. Malin. Direct photographic image enhancement in astronomy. *J.Phot.Sci*, 29:199+, December 1981.

[88] H. A. Mayer-Hasselwander, D. L. Bertsch, B. L. Dingus, A. Eckart, J. A. Esposito, R. Genzel, R. C. Hartman, S. D. Hunter, G. Kanbach, D. A. Kniffen, Y. C. Lin, P. F. Michelson, A. Muecke, C. von Montigny, R. Mukherjee, P. L. Nolan, M. Pohl, O. Reimer, E. J. Schneid, P. Sreekumar, and D. J. Thompson. High-energy gamma-ray emission from the galactic center. *Astron. & Astrophys.*, 335:161–172, July 1998.

[89] A. Melchiorri, P. A. R. Ade, P. de Bernardis, J. J. Bock, J. Borrill, A. Boscaleri, B. P. Crill, G. De Troia, P. Farese, P. G. Ferreira, K. Ganga, G. de Gasperis, M. Giacometti, V. V. Hristov, A. H. Jaffe, A. E. Lange, S. Masi, P. D. Mauskopf, L. Miglio, C. B. Netterfield, E. Pascale, F. Piacentini, G. Romeo, J. E. Ruhl, and N. Vittorio. A measurement of ω from the north american test flight of boomerang. *ApJ Lett.*, 536:L63–L66, June 2000.

[90] D. Merritt. Relaxation and tidal stripping in rich clusters of galaxies. i - evolution of the mass distribution. *ApJ*, 264:24–48, January 1983.

[91] D. Merritt. Relaxation and tidal stripping in rich clusters of galaxies. ii - evolution of the luminosity distribution. *ApJ*, 276:26–37, January 1984.

[92] D. Merritt. Relaxation and tidal stripping in rich clusters of galaxies. iii - growth of a massive central galaxy. *ApJ*, 289:18–32, February 1985.

[93] M. Moles, J. M. Garcia-Pelayo, J. Masegosa, and A. Aparicio. Ubvri observations of bl lacertae objects. *ApJS*, 58:255–263, June 1985.

[94] B. Moore. Evidence against dissipationless dark matter from observations of galaxy haloes. *Nat*, 370:629+, August 1994.

[95] B. Moore. Caustic rings and cold dark matter. `astro-ph/0103094`, March 2001.

[96] B. Moore, C. Calcáneo-Roldán, J. Stadel, T. Quinn, G. Lake, S. Ghigna, and F. Governato. Dark matter in draco and the local group: Implications for direct detection experiments. *Phys. Rev. D*, `astroph/0106271`:12, July 2001.

[97] B. Moore, S. Ghigna, F. Governato, G. Lake, T. Quinn, J. Stadel, and P. Tozzi. Dark matter substructure within galactic halos. *ApJ Lett.*, 524:L19–L22, October 1999.

[98] B. Moore, F. Governato, T. Quinn, J. Stadel, and G. Lake. Resolving the structure of cold dark matter halos. *ApJ Lett.*, 499:L5–+, May 1998.

[99] B. Moore, N. Katz, and G. Lake. On the destruction and overmerging of dark halos in dissipationless n-body simulations. *ApJ*, 457:455–459, February 1996.

[100] B. Moore, N. Katz, G. Lake, A. Dressler, and A. Oemler. Galaxy harassment and the evolution of clusters of galaxies. *Nat*, 379:613–616, 1996.

[101] B. Moore, G. Lake, and N. Katz. Morphological transformation from galaxy harassment. *ApJ*, 495:139+, March 1998.

[102] B. Moore, T. Quinn, F. Governato, J. Stadel, and G. Lake. Cold collapse and the core catastrophe. *MNRAS*, 310:1147–1152, December 1999.

[103] J. F. Navarro, C. S. Frenk, and S. D. M. White. The structure of cold dark matter halos. *ApJ*, 462:563+, May 1996.

[104] J. F. Navarro, C. S. Frenk, and S. D. M. White. A universal density profile from hierarchical clustering. *ApJ*, 490:493+, December 1997.

[105] J. F. Navarro and M. Steinmetz. The core density of dark matter halos: A critical challenge to the λcdm paradigm? *ApJ*, 528:607–611, January 2000.

[106] R. P. Olling and M. R. Merrifield. The shape of the milky way's dark halo. In *ASP Conf. Ser. 182: Galaxy Dynamics - A Rutgers Symposium*, pages 407+, August 1999.

[107] P. J. E. Peebles. Structure of the coma cluster of galaxies. *AJ*, 75:13+, February 1970.

[108] S. Perlmutter, G. Aldering, M. della Valle, S. Deustua, R. S. Ellis, S. Fabbro, A. Fruchter, G. Goldhaber, D. E. Groom, I. M. Hook, A. G. Kim, M. Y. Kim, R. A. Knop, C. Lidman, R. G. McMahon, P. Nugent, R. Pain, N. Panagia, C. R. Pennypacker, P. Ruiz-Lapuente, B. Schaefer, and N. Walton. Discovery of a supernova explosion at half the age of the universe. *Nat*, 391:51+, January 1998.

[109] S. Perlmutter, G. Aldering, G. Goldhaber, R. A. Knop, P. Nugent, P. G. Castro, S. Deustua, S. Fabbro, A. Goobar, D. E. Groom, I. M. Hook, A. G. Kim, M. Y. Kim, J. C. Lee, N. J. Nunes, R. Pain, C. R. Pennypacker, R. Quimby, C. Lidman, R. S. Ellis, M. Irwin, R. G. McMahon, P. Ruiz-Lapuente, N. Walton, B. Schaefer, B. J. Boyle, A. V. Filippenko, T. Matheson, A. S. Fruchter, N. Panagia, H. J. M. Newberg, W. J. Couch, and The Supernova Cosmology Project. Measurements of omega and lambda from 42 high-redshift supernovae. *ApJ*, 517:565–586, June 1999.

[110] T. Quinn, N. Katz, J. Stadel, and G. Lake. Time stepping n-body simulations. *submited to ApJ*, `astro-ph/9710043` , oct 1997.

[111] G. Raffelt. Astrophysical axion bounds: An update. *Proc. of "Beyond the Desert", Ringberg Castle, Germany, June 8-14, 1997*, `astro-ph/9707268` , jun 1997.

[112] K. D. Rakos, A. P. Odell, and J. M. Schombert. The butcher-oemler effect in abell 2317. *ApJ*, 490:194+, November 1997.

[113] D. O. Richstone. Collisions of galaxies in dense clusters. ii - dynamical evolution of cluster galaxies. *ApJ*, 204:642–648, March 1976.

[114] P. D. Sackett. Does the milky way have a maximal disk? *ApJ*, 483:103+, July 1997.

[115] R. Sadat and A. Blanchard. New light on the baryon fraction in galaxy clusters. *Astron. & Astrophys.*, 371:19–24, May 2001.

[116] D. J. Schlegel, D. P. Finkbeiner, and M. Davis. Maps of dust infrared emission for use in estimation of reddening and cosmic microwave background radiation foregrounds. *ApJ*, 500:525+, June 1998.

[117] C. Schmid, D. J. Schwarz, and P. Widerin. Peaks above the harrison-zel'dovich spectrum due to the quark-gluon to hadron transition. *Physical Review Letters*, 78:791–794, February 1997.

[118] B. P. Schmidt, N. B. Suntzeff, M. M. Phillips, R. A. Schommer, A. Clocchiatti, R. P. Kirshner, P. Garnavich, P. Challis, B. Leibundgut, J. Spyromilio, A. G. Riess, A. V. Filippenko, M. Hamuy, R. C. Smith, C. Hogan, C. Stubbs, A. Diercks, D. Reiss, R. Gilliland, J. Tonry, J. ; Maza, A. Dressler, J. Walsh, and R. Ciardullo. The high-z supernova search: Measuring cosmic deceleration and global curvature of the universe using type ia supernovae. *ApJ*, 507:46–63, November 1998.

[119] D. J. Schwarz and S. Hofmann. Small-scale structure of cold dark matter. *Nuclear Physics B Proceedings Supplements*, 87:93–95, 2000.

[120] J. A. Sellwood. Is a simple collisionless relic dark matter particle ruled out? *ApJ Lett.*, 540:L1–L4, September 2000.

[121] P. Sikivie. Caustic ring singularity. *Phys. Rev. D*, 60:80d+, September 1999.

[122] J. Silk and H. Bloemen. A gamma-ray constraint on the nature of dark matter. *ApJ Lett.*, 313:L47–L51, February 1987.

[123] Joseph Silk and Mark Srednicki. Cosmic-ray antiprotons as a probe of a photino-dominated universe. *Phys. Rev. Lett.*, 53:624, 1984.

[124] D. N. Spergel and P. J. Steinhardt. Observational evidence for self-interacting cold dark matter. *Phys. Rev. Lett.*, 84:3760–3763, 2000.

[125] P. Sreekumar, D. L. Bertsch, B. L. Dingus, C. E. Fichtel, R. C. Hartman, S. D. Hunter, G. Kanbach, D. A. Kniffen, Y. C. Lin, J. R. Mattox, H. A. Mayer-Hasselwander, P. F. Michelson, C. von Montigny, P. L. Nolan, K. Pinkau, E. J. Schneid, and D. J. Thompson. Observations of the large magellanic cloud in high-energy gamma rays. *ApJ Lett.*, 400:L67–L70, December 1992.

[126] F. W. Stecker. The cosmic gamma-ray background from the annihilation of primordial stable neutral heavy leptons. *ApJ*, 223:1032–1036, August 1978.

[127] M. Tarenghi. Old and new observations of the m87 jet. In *Optical Jets in Galaxies*, pages 145–151, March 1981.

[128] T. Theuns and S. J. Warren. Intergalactic stars in the fornax cluster. *MNRAS*, 284:L11–L15, January 1997.

[129] T. X. Thuan and J. Kormendy. Photographic measurements of the diffuse light in the coma cluster. *PASP*, 89:466–473, August 1977.

[130] A. Toomre. On the gravitational stability of a disk of stars. *ApJ*, 139:1217–1238, May 1964.

[131] N. Trentham and B. Mobasher. The discovery of a giant debris arc in the coma cluster. *MNRAS*, 293:53+, January 1998.

[132] M. S. Turner. Dark matter and dark energy in the universe. In *ASP Conf. Ser. 165: The Third Stromlo Symposium: The Galactic Halo*, pages 431+, 1999.

[133] M. S. Turner and J. A. Tyson. Cosmology at the millennium. *Reviews of Modern Physics, Volume 71, Issue 2, March 1999, pp.S145-S164*, 71:145–, 1999.

[134] Michael S. Turner. Probing the structure of the galactic halo with gamma rays produced by wimp annihilations. *Phys. Rev.*, D34:1921, 1986.

[135] Michael S. Turner. Ten things everyone should know about inflation. *To be published in Generation of Cosmological Large-scale Structure, edited by D.N. Schramm*, astro-ph/9704062 , apr 1997.

[136] J. A. Tyson and P. Fischer. Measurement of the mass profile of abell 1689. *ApJ Lett.*, 446:L55–+, June 1995.

[137] D. Tytler, S. Burles, L. Lu, X. Fan, A. Wolfe, and B. D. Savage. The deuterium abundance at z=0.701z = 0.701 toward qso 1718+4807. *AJ*, 117:63–67, January 1999.

[138] P. Ullio and L. Bergström. Neutralino annihilation into a photon and a Z boson. *Phys. Rev. D*, 57:1962–1971, February 1998.

[139] P. Ullio and M. Kamionkowski. Velocity distributions and annual-modulation signatures of weakly-interacting massive particles. *JHEP*, 03:049, April 2001.

[140] J. M. Uson, S. P. Boughn, and J. R. Kuhn. Diffuse light in dense clusters of galaxies. i - r-band observations of abell 2029. *ApJ*, 369:46–53, March 1991.

[141] M. Valluri. Compressive tidal heating of a disk galaxy in a rich cluster. *ApJ*, 408:57–70, May 1993.

[142] E. van Kampen. Improved numerical modelling of clusters of galaxies. *MNRAS*, 273:295–327, March 1995.

[143] R. Vilchez-Gomez, R. Pello, and B. Sanahuja. Detection of intracluster light in the rich clusters of galaxies abell 2390 and cl 1613+31. *Astron. & Astrophys.*, 283:37–50, March 1994.

[144] M. L. Weil, J. Bland-Hawthorn, and D. F. Malin. Diffuse stellar light at 100 kiloparsec scales in m87. *ApJ*, 490:664+, December 1997.

[145] M. D. Weinberg. Adiabatic invariants in stellar dynamics. 1: Basic concepts. *AJ*, 108:1398–1402, October 1994.

[146] M. D. Weinberg. Adiabatic invariants in stellar dynamics. 2: Gravitational shocking. *AJ*, 108:1403–1413, October 1994.

[147] B. J. Weiner, J. A. Sellwood, and T. B. Williams. The disk and dark halo mass of the barred galaxy ngc 4123. ii. fluid-dynamical models. *ApJ*, 546:931–951, January 2001.

[148] S. D. M. White. The dynamics of rich clusters of galaxies. *MNRAS*, 177:717–733, December 1976.

[149] S. D. M. White, C. S. Frenk, and M. Davis. Clustering in a neutrino-dominated universe. *ApJ Lett.*, 274:L1–L5, November 1983.

[150] S. D. M. White, J. F. Navarro, A. E. Evrard, and C. S. Frenk. The baryon content of galaxy clusters - a challenge to cosmological orthodoxy. *Nat*, 366:429+, December 1993.

[151] L. M. Widrow. Distribution functions for cuspy dark matter density profiles. *ApJS*, 131:39–46, November 2000.

[152] M. I. Wilkinson and N. W. Evans. The present and future mass of the milky way halo. *MNRAS*, 310:645–662, December 1999.